The Dissertation Committee for Jeffrey Charles Wiemeri
certifies that this is the approved version of the following dissertation:

# Magnetic Field Enhancement of Coulomb Blockade Conductance Oscillations in Metal-Metal Oxide Double Barrier Tunnel Devices Fabricated Using Atomic Force Microscope Nanolithography

**Committee:**

_____________________________________
**Chih-Kang Ken Shih, Supervisor**

_____________________________________
**Sanjay K. Banerjee**

_____________________________________
**Thomas A. Spencer**

_____________________________________
**Alejandro De Lozanne**

_____________________________________
**Qian Niu**

# Magnetic Field Enhancement of Coulomb Blockade Conductance Oscillations in Metal-Metal Oxide Double Barrier Tunnel Devices Fabricated Using Atomic Force Microscope Nanolithography

by

**Jeffrey Charles Wiemeri, B.S., M.S.**

**Dissertation**

Presented to the Faculty of the Graduate School of
the University of Texas at Austin
in Partial Fulfillment
of the Requirements
for the Degree of

**Doctor of Philosophy**

The University of Texas at Austin

May 2005

For my loving wife, Kiley.

# Acknowledgements

The author expresses his sincere appreciation to the Space Based IR Technology Branch of the Space Vehicles Directorate, Air Force Research Laboratory. Without their continuous support and use of their laboratory equipment the devices discussed in this dissertation would not have been characterized.

To Paiboon Tangyunyong and Jeremy Walraven at the Failure Analysis Laboratory at Sandia National Laboratory, many thanks for the support and use of their Atomic Force Microscope.

My sincere appreciation to the U.S. Air Force, the Texas Advanced Materials Research Center, and the DARPA/MARCO MSD Focus Center for providing financial support for this research.

For the staff of the Microelectronics Research Center, many thanks for your support and training on clean room equipment including the oxide furnaces, III-V lithography bay, the CHA e-beam evaporator, and the Atomic Force Microscope. I would like to especially thank Jeannie Toll and Joyce Kokes for the help with administrative needs and equipment purchases.

Dr. Ken Shih, Dr. Sanjay Banerjee, and Dr. Thomas Spencer, thank you for the comments, edits, and discussions leading me to this point. For the members of the High Power Microwave Division who have supported me as deputy branch chief and branch chief while I have been working on this dissertation, *HERE HERE*!

Jeffrey C. Wiemeri, Major, USAF

Physicist

# Magnetic Field Enhancement of Coulomb Blockade Conductance Oscillations in Metal-Metal Oxide Double Barrier Tunnel Devices Fabricated Using Atomic Force Microscope Nanolithography

Publication No. _____________

Jeffrey Charles Wiemeri, Ph.D.
The University of Texas at Austin, 2005

Supervisor: Chih-Kang Ken Shih

Magnetic field enhancement of Coulomb blockade conductance oscillations in metal oxide double barrier tunnel devices fabricated using atomic force microscope nanolithography is reported for the first time. Anodic oxidation by this method was accomplished on lithographically patterned Ti and Ni device layers. This is the first time Ni has been reported to be oxidized via scanning probe lithography. Magnetoresistance measurements were taken on selected devices in a Hall effect cryogenic system where tunneling conductance behavior was observed at 1.8, 10, 25, and 50 K in the Ti devices and 150 K in the Ni devices. Coulomb blockade conductance features were observed at

1.8, 10 and 50 K in the Ti devices and 10 and 25 K in the Ni devices. Applying a 9T magnetic field enhanced the conductance oscillations and clarified the Coulomb staircase apparent in the I-V curves for both devices. From theoretical fits of the experimental conductance behavior for the Ti devices, this is attributed to a suppression of cotunneling currents in the device. Additionally, in multiple Ti devices, a zero-bias anomaly peak was observed at ~ 2 K and is attributed to contaminant particles in the metal oxide barrier creating a localized magnetic moment in the junction leading to spin-flip and s-d exchange scattering assisted tunneling according to the Anderson-Appelbaum model. This is the first time these zero-bias anomalies have been observed and reported in planar tunnel junctions.

# Table of Contents

# List of Figures

# Chapter One

# Introduction

## Section 1.1: The Need For Nanoscale Electronics Technology

Since 1965, when *Electronics* magazine published Gordon Moore's famous prediction [1] that the number of transistors on a chip would double every year and predicted that the trend would continue into the next decade, the ability of the microelectronics industry to shrink the dimensions of silicon based electronic devices according to the famous "Moore's Law" has been nothing short of amazing. After the co-founder of Intel's initial prediction, the slope changed in the mid-1970s to a doubling approximately every 18 months and for more than thirty years device density on chips has doubled according to this exponential progression [2]. This exponential increasing density of devices has increased performance while reducing cost and size of microchips, and subsequently the computers around which they are based. Additionally, information storage technologies have been advancing rapidly where hard drive capacities have been doubling every year. These developments, too, have become tied in with the famous "law". The end result is that today one can buy a new sub-$1000 desktop computer that is more powerful than a $3000 computer sold only a few years ago [3].

This rapid and amazing pace of computer technology, from semiconductor based logic devices, to hard disk drives, to memory devices has pushed the limits of engineering and has quickly generated a need to understand the science and engineering of working with devices on the nanoscale. Understanding how to make devices with dimensions of tens of nanometers to increase logic, storage and memory density and understanding the transport behavior at these dimensions has become crucial to continuing the pace of this technological advancement.

While keeping silicon-based processing on track with the famous “law”, accompanying developments in reducing line widths (the width of the smallest feature) by a factor of two every six years, increasing clock-rates by a factor of two every two years, and increasing capacities of random access memory (RAM) by a factor of two every 18 months have also occurred. Not content with resting on its laurels, the semiconductor industry is committed to maintaining adherence to “Moore’s Law” for as long a physically and financially possible. In order to keep the industry moving on track, the National Technology Roadmap for Semiconductors was established in the early 1990s. Detailing all the technologies needed to maintain progress, the roadmap outlines where funding for research and development is needed. In the past couple years, the roadmap was opened to international participation from Europe, Japan, Korea, and Taiwan, leading to the creation of the International Roadmap for Semiconductors.

Currently, state-of-the-art chips are produced with a minimum line width of 90 nanometers, a density of 0.97 gigabits per centimeter squared (GBits/cm$^2$), and an oxide thickness of 1.2 nm [4]. The latest 2004 roadmap lays out development through 2018 with 18 nm line widths, a density nearing 40 gigabits per square centimeter (Gbits/cm$^2$), and an oxide thickness of 0.5 nm. However, starting in 2005, the roadmap also begins to show several unsolved problems as device dimensions continue to shrink, with the situation becoming quite grave starting as early as 2006. Just one of the issues raised by the ever decreasing sizes is leakage through the gates as gate thicknesses approach the widths of a couple atoms. Additionally, the roadmap calls for research in metallization technologies, lithography techniques, new photoresists, device characterization techniques, device design, and new dielectric materials to name a few. All this research is being called upon to deal with the issues of operating at the nanoscale, the region between the atomic scale of tenths of nanometers up to multiple tens of nanometers.

Semiconductor logic and memory devices are not the only advancing technology areas benefiting from, and being challenged by, nanotechnology. Computer hard disk drive technology has seen a great boom recently as thin film growth technology has resulted in present recording densities more than 25 million times greater than when the original IBM 5 MB disk came out in 1956 [5, 6].

The majority of this gain has occurred since 1997 when IBM introduced giant magnetoresistance (GMR) based hard drives [7]. GMR was discovered in 1988 by multilayering Fe and Cr layers using molecular beam epitaxy (MBE) [7, 8]. As a magnetic field is applied to a stack of layers consisting of two ferromagnetic materials separated by a thin conducting layer, the magnetization in one ferromagnetic layer becomes aligned with the applied field and as the field is increased further both types of materials become aligned. When the two layers are in anti-parallel alignment, the resistance can be as much as 60% greater than when the magnetization of the layers is in parallel. However, the largest GMR percentage change between alignments observed in a device at room temperature is ~ 24% [9].

GMR technology advancements, such as utilizing GMR read heads in addition to the disks, utilizing an initial antiferromagnetic layer to pin the first ferromagnetic layer by exchange coupling (what is known as spin-valve GMR) to increase GMR have led to reduction in the required size of the read head and write pole tip [5-8]. These advancements have led to annual increases of 100% (thus an approximate doubling each year) in the recording density of hard disks. Utilizing the latest ferromagnetic technology, the "superparamagnetic" limit (the point at which the individual magnetization domains have become so small that they are no longer able to hold magnetization due to thermal instabilities) has been pushed to up to 300 Gbits/in$^2$ for GMR hard drives [6].

To achieve this density, read heads utilizing Tunneling Magnetoresistance (TMR), where the two ferromagnetic materials are separated by a thin dielectric tunneling layer (instead of the conductive layer in GMR), are being studied. TMR values have been achieved at greater than 50% at room temperature [7]. Additionally, in a TMR device the current flows perpendicularly through the device, allowing the read head (sensor) to be attached directly to the magnetic shields, which can then also be used as the electrical contacts for the device. This is unlike GMR heads where the current flows parallel to the device and the sensor has to be electrically isolated from the conducting magnetic shields. Thus TMR devices do not have the isolation layers taking up crucial space, increasing their compatibility with high density read heads [7, 8]. However, TMR devices are more highly resistive than GMR devices, limiting their use for high performance high data rate disk drives. Thus with shrinking sensor size, other read head technology is being pursued, such as the current perpendicular to plane (CPP) devices [5-8].

Beyond the 300 Gbits/in$^2$ limit, perpendicular to plane (versus the current in plane) recording methods will be required as TMR resistance is too high [7, 8]. In this method, data is recorded on the small ends of the magnetic domains as well as on their long axis, where data is currently stored. Using this technique, storage densities may approach 500 – 600 GBits/in$^2$. Utilizing lithographically defined magnetic islands or self-assembled nanoparticles of FePt patterned with nano-imprint lithography, recording densities could be extended to 1 Tb/in$^2$ [6, 8]. To achieve these recording densities at the current rate of advancement, read heads and write pole tip dimensions will need to decrease 20-30% each year and will soon match the dimensional requirements for semiconductor devices discussed previously [6].

Memory is another technology area that will rely upon nanotechnology to allow it to continually increase storage density and speed. Flash memory devices are based on standard silicon process technology (which manufactures desire to be uniform for all device components). As dimensions are scaled down, the tunneling oxide thickness for the flash memory floating gate oxide becomes so thin the gate is no longer able to hold charge [9]. Thus Flash memory will have trouble meeting increasing demands for low voltage, high speed, high retention, and high endurance operation. Multiple technologies are emerging to fill this void. Two such technologies are the magnetic tunnel junction (MTJ) magnetic random access memory (MRAM) based around TMR mentioned earlier, and single electron shut-off memory [7-9].

Recently, non-volatile MRAM technology has favored arrays of individually patterned magnetic storage cells or bits where each bit comprises a magnetic thin film multilayered structure. The technology of choice for these magnetic bits has been anisotropic magnetoresistance (AMR) [7, 8]. In AMR, the angle the current flows through a ferromagnet in relation to the orientation of the magnetization generates a resistance proportional to $\cos^2\theta$. This effect is an order of magnitude less than GMR, which at first look appears ideal for MRAM applications.. GMR based devices have much greater resistance change than AMR, the bit construction is much simpler, the time to read a bit (which to first approximation is proportional to the strength of signal required to read it) is much quicker, and the bit can be read with a much lower signal (meaning it can be read nondestructively thus preventing having to rewrite the bit every time it is read). However, GMR technology is not ideal for MRAM applications for the simple reason that ironically the device resistance is too low, due to the internal conducting spacers [7]. In order to properly balance an MRAM memory circuit using GMR technology, the GMR bits would need to be wired in series. Creating such a circuit with many bits in a large array would greatly decrease the signal actually used to read any particular bit and addressing an individual bit would be difficult. However, MTJ MRAM based around the higher resistance TMR technology (with the thin dielectric tunneling layer) has all the benefits of GMR based bits, but has an even higher change in resistance. Basically, TMR devices work on the effect that when the magnetization of the two ferromagnets is aligned (parallel configuration) the number of occupied energy states in one electrode and the number of available states in the other electron is optimized, thus the probability of tunneling is greatest [9]. Thus, information is stored by either the device being very conductive or very resistive. When the bit is in antiparallel configuration (resistive), the tunneling is between majority states in one electrode and minority states in the other electrode, thus the conductance (based on tunneling probability) is greatly reduced. As mentioned, TMR devices are perpendicular devices thus have a higher potential bit density. More importantly, because of their higher resistance they can be laid out with a novel cross-point circuit architecture where the devices are not in series with each other, but are in series with a switch so they can each be individually addressed. This greatly reduces the amount of signal required to read and write the bit information [7]. Subsequently, there are many expected advantages of MTJ MRAM technology, such as unlimited read/writes, read access time of ~ 10 ns, write times of ~ 50 ns, high bit densities, low power (no refresh/charge pumps needed for erase), low voltage, non-volatile, radiation immune and a wide operating temperature [8]. Thus MTJ MRAM has the potential capability of rivaling dynamic random access memory (DRAM) in density (as the current flows perpendicular through the bit vice parallel to it, as mentioned for hard drive technology) and static random access memory (SRAM) in speed (as the amount of signal needed to a read a bit is greatly reduced from the larger TMR effect) [7-9].

Another upcoming memory technology to challenge flash memory is single electron shut-off (SESO) memory [9]. The single electron device stacks over the gate of the access transistor replacing the DRAM capacitor and giving a cell limited only by the dimensions. SESO memory is a gain memory and stores several hundred electrons versus the 100,000 level in current DRAMs. The SESO transistor is combined with a metal oxide semiconductor field effect transistor (MOSFET) to form a memory cell.

During write operation, charges are transferred from the write data line to the storage node through the SESO transistor. The stored charges are read as a threshold shift of the MOS transistor. The signal can be read with conventional memory circuitry. In a SESO memory device, there is an ultra-thin polysilicon film that suppresses electron hopping between traps because electrons on the traps can 'sense' the Coulomb repulsion of the other traps preventing tunneling or hopping to the other traps (a phenomena called Coulomb blockade to be described later). Thus in a SESO device, the leakage is significantly reduced over that of standard MOSFET technology where a primary source of leakage is electron hopping or tunneling from conduction band to valence band by way of mid-gap trap states in a thick polysilicon layer. Additionally, SESO memory requires about 30% fewer processing steps than standard DRAM technology.

To produce all the technologies mentioned requires precise engineering skills and in-depth scientific knowledge. Being able to develop and tailor device materials and structures to control tunneling through thin oxides in logic devices, to create ultra small patterned magnetic domains for GMR hard disk drives, and to write and maintain bit information in MTJ MRAM and SESO memory devices is an absolute necessity. To do this requires the fundamental knowledge of tunneling behavior with different materials, knowing how devices on the nanoscale behave under a magnetic field, and applying new lithography techniques to different materials to increase the knowledge base for novel logic, hard disk and memory technologies.

The difficulty in developing this scientific and technical knowledge base is that the physics at this scale is different from what industry has been used to. In the nanoscale regime (~ 10 nm – 100 nm), mesoscopic physics dominates: too large for most quantum effects, but too small to be considered bulk. As an example, the scaling laws for semiconductor logic devices start to break down around 80 nm line widths [3]. Other issues reside in materials, device fabrication, and just plain scientific knowledge. Precise control on this scale is absolutely necessary to achieve an understanding and control of new phenomena.

Specifically for the case of MTJ devices, the tunneling probability and TMR depends on the spin polarization. How spin polarization is actually manifested is unclear. The tunneling probability for specific spin states of the tunneling electrons will be influenced by the symmetry of the electronic states in the ferromagnetic metals and the detailed band structure of the insulation tunnel barrier. The symmetry of electron states in the ferromagnetic layers may affect how the tunnel probability depends on barrier thickness. Thus, the magnitude and the spin states of the tunneling electrons could be influenced by the thickness of the tunnel barrier. Additionally, how the tunneling probability is affected by electronic states at the insulator/ferromagnetic metal interface is not entirely clear nor how does the formation of a tunnel barrier of various materials affect the properties of the ferromagnetic metal. These are just a few issues awaiting more detailed analysis.

## Section 1.2: Purpose of Research

This research effort was undertaken to contribute to the science required to advance nanoscale electronics technology. Utilizing a relatively novel lithography technique whereby metals are anodized with a scanning probe microscope tip [10-12], lateral metal-metal oxide tunnel barrier devices were formed on Titanium (Ti) and Nickel (Ni). The former has been reported by a few research groups working with Kazuhiko Matsumoto [13-15] and offers a base of knowledge by which to proceed to other materials. Ni was studied as this is a ferromagnetic metal, and applying a novel lithography technique, which has never been applied to a material, would open up new avenues of research. Also NiO is an antiferromagnetic material that can also be a semiconductor depending on processing. Often Al-O or $Al_2O_3$ is used as the insulating dielectric layer in TMR devices; NiO perhaps could offer an alternative with proper study of its tunneling properties.

Current-voltage (I-V) measurements were made versus magnetic field at different temperatures for the Ni and Ti devices to study transport phenomena such as tunneling and Coulomb blockade. Results show that applying a strong magnetic field to these tunnel devices decreased the overall conductance by reducing the probability of higher order tunneling mechanisms and enhanced observed Coulomb blockade phenomena.

To adequately discuss the results of the research three chapters of background are presented. Chapter Two discusses the general length scales involved with nanoscale/mesoscopic devices and the physics behind Coulomb blockade phenomena. Chapter Three and Chapter Four discuss the theories regarding the transport characteristics of metal-insulator-metal (MIM) tunnel devices and zero-bias anomalies, respectively. Chapter Five describes the techniques used for fabricating nanoscale oxide barriers using scanning probe nanolithography. The devices used for the characterization and reasons for their use and the detailed method of characterization are then described.

Experimental results and analysis are presented and compared to results of other research groups. Lastly some concluding comments are provided. As an aid to future research, detailed information on any areas where the author possessed primary knowledge on procedures or practices are included in the appendices.

# Chapter Two

# Mesoscopic Length Scales and Coulomb Blockade

## Section 2.1: Mesoscopic Length Scales

Following the development presented in *Mesoscopic Physics and Electronics* [16], when fabricating devices at nanometer length scales, how these length scales effect physical behavior is important. Mesoscopic devices are categorized by their respective length, width, and height in relation to the Fermi wavelength, $\lambda_F$. At zero temperature, electrons occupy all the states specified by the wave vector **k** up to the Fermi wave number, $k_{F,}$ and the Fermi wavelength is defined as, $\lambda_F = 2\pi/k_{F.}$ Thus the Fermi wavelength can be interpreted as the physical distance between states at zero temperature, thus one electron will occupy a cube of volume $\lambda_F^3$ in three dimensions. For a given volume in the reciprocal k-space, the number of k states allowed in that volume at zero temperature is given by

$$\frac{V_{k-space}}{k_F^{\ 3}} = \frac{V_{k-space}}{(2\pi/\lambda_F)^3} = \frac{V_{k-space} \bullet V_{Fermielectron}}{8\pi^3} \qquad (1)$$

As mentioned, at zero temperature, all the electrons will occupy a sphere in k-space up to radius $k_F$, thus the number of allowed states (thus number of electrons) will be given by

$$N = \frac{4\pi}{3} k_F^{\ 3} \frac{\lambda_F^{\ 3}}{8\pi^3} 2 \qquad (2)$$

where the factor of two comes from the two electron spins. The density would then be just this number divided by $\lambda_F^3$. This process can be done for each dimension in k-space for different dimensional systems, d = 0, 1, 2, or 3. Incorporating the factor of two, one obtains:

$$
\begin{aligned}
n &= 2 && d = 0 \text{ (0 Dimensions)} \\
n &= \frac{2}{2\pi} k_F && d = 1 \text{ (1 Dimension)} \\
n &= \frac{2}{(2\pi)^2} \pi k_F{}^2 && d = 2 \text{ (2 Dimensions)} \\
n &= \frac{2}{(2\pi)^3} \frac{4}{3} \pi k_F{}^3 && d = 3 \text{ (3 Dimensions)}
\end{aligned}
\qquad (3)
$$

For metals, $\lambda_F$ is on the order of a few Å in bulk, while for 2D semiconductor systems $\lambda_F$ can be on the order of several hundred Å. Mesoscopic system dimensional scales are defined in terms of $\lambda_F$ as follows:

For a box, $L_x$ by $L_y$ by $L_z$,

$$
\begin{aligned}
&\lambda_F << L_x, L_y, L_z && \text{3D system (bulk)} \\
&\lambda_F \approx L_x << L_y, L_z && \text{Quasi 2D system (thin films)} \\
&L_x < \lambda_F << L_y, L_z && \text{2D system (heterostructures)} \\
&L_x < \lambda_F \approx L_y << L_z && \text{Quasi 1D system (quantum wires)} \\
&L_x, L_y < \lambda_F << L_z && \text{1D system (point contacts)} \\
&L_x, L_y, L_z < \lambda_F && \text{0D system (quantum dot)}
\end{aligned}
\qquad (4)
$$

The first question in making a tunnel device is how does one know if all conduction paths through a barrier have been closed leaving only tunneling as mechanisms by which electrons can transport through the barrier at low applied voltages ($V < \varphi_o$ (the barrier height)) and at low temperatures (thus eliminating thermionic emission). The answer comes from the formulation by Landauer, who derived a relation for the conductance in a 1D wire .

For a 1D quantum point contact connected to two electrodes at chemical potentials $\mu_1$ and $\mu_2$ the net current at zero temperature is given by

$$I = e\sum_{n=1}^{N}\int_{\mu_1}^{\mu_2} dE \frac{\partial N_n}{\partial E} v_n(E) T_n(E) \qquad (5)$$

where $v_n$ and $T_n$ are the velocity and transmission probability of n-th subband, $E$ are the energy levels corresponding to each **k** value of the system and N is the occupied number of states. The voltage between the ideal electrodes measured in a four-probe set-up is, with a reflection probability at the ideal leads of each subband $R_n$ included (in other words, a non-perfect interface to the ideal leads),

$$V = \sum_{n=1}^{N} \frac{R_n(\mu_2 - \mu_1)}{e} \qquad (6)$$

For a 1D contact $n = k_F/\pi$,

$$\frac{\partial N}{\partial E} = \frac{1}{\pi\hbar}\left(\frac{\partial \hbar k_F}{\partial E}\right) = \frac{1}{\pi\hbar}\left(\frac{\partial \frac{(\hbar k_F)^2}{2m}}{\partial \hbar k_F}\right)^{-1} = \frac{1}{\pi\hbar}\frac{2m}{2\hbar k_F} = \frac{1}{\pi\hbar v} \qquad (7)$$

where $\hbar$ is Planck's constant, $h$, divided by 2π. Thus, the velocity terms in the integral cancel. Assuming the voltage difference, $V$, between leads is much less than the Fermi energy, $E_F$, then $T_n(E) = T_n(E_F)$ is a constant. Then the integral is independent of energy and one can write

$$I = e\sum_{n=1}^{N}\int_{\mu_1}^{\mu_2} dE\,\frac{\partial N_n}{\partial E}v_n(E)T_n(E) = e\sum_{n=1}^{N}(\mu_2-\mu_1)\frac{1}{\pi\hbar}T_n(E_F) = e\sum_{n=1}^{N}(\mu_2-\mu_1)\frac{2}{h}T_n(E_F) \qquad (8)$$

The conductance is G = I/V, thus:

$$G = e\frac{\sum_{n=1}^{N}(\mu_2-\mu_1)\frac{2}{h}T_n(E_F)}{\sum_{n=1}^{N}\frac{R_n(\mu_2-\mu_1)}{e}} = \frac{2e^2}{h}\sum_{n=1}^{N}\frac{T_n(E_F)}{R_n} = \frac{2e^2}{h}\sum_{n=1}^{N}\frac{T_n(E_F)}{(1-T_n(E_F))} \qquad (9)$$

In a two terminal measurement, the voltage and current are measured with the same leads, and the potential drop is not only for the scattering structure but also for contact with the ideal leads, in this case V is simply

$$V = \sum_{n=1}^{N}\frac{(\mu_2-\mu_1)}{e} \qquad (10)$$

If the transmission probability is 1, then

$$G = e^2\frac{\sum_{n=1}^{N}(\mu_2-\mu_1)\frac{2}{h}T_n(E_F)}{\sum_{n=1}^{N}(\mu_2-\mu_1)} = \frac{2e^2}{h}\sum_{n=1}^{N}T_n(E_F) = \frac{2e^2}{h}\sum_{n=1}^{N}1 = \frac{2e^2}{h}\bullet N \qquad (11)$$

Thus conductance for a point contact is quantized in steps of $2e^2/h$. The quantum resistance $R_Q$ is the inverse of this value and is equivalent to 12.9 kΩ.

For the creation of tunnel barriers, if one treats a junction between two electrodes as multiple parallel paths, as these paths are constrained to less than the width of the

Fermi wavelength, the conductance of the overall junction will drop in steps of $2e^2/h$. As the last path is closed, and the conductance drops below $2e^2/h$ there are no conduction paths left and the barrier becomes a tunnel barrier. Thus for a tunnel barrier, the resistance in a barrier needs to be greater than $R_Q$. To ensure a large enough resistance, a common rule of thumb is to ensure barriers resistance exceed $h/e^2$, thus $R_Q$ is also often defined in literature as 25.8 kΩ. When fabricating tunnel barriers, increasing the barrier thickness, increases scattering and placing several in series will increase resistance beyond $R_Q$. This will subsequently reduce any measured current requiring higher fidelity apparatus for measurements. Quantum resistance is not to be confused with standard series resistance in a standard material. One can have a highly scattering material with $R \gg R_Q$, but this does not mean the device is tunneling. The flow of electrons is impeded by scattering centers requiring higher fields (voltage) to generate a current, and the current will be linear versus voltage (that is ohmic). The best way to verify that a device is tunneling is to measure its I-V characteristics before and after a barrier is formed. If the resistance jumps from less than a few kΩ to above $R_Q$ when the barrier is made and a parabolic conductance is exhibited (see Chapter Three on Simmons' MIM tunneling theory) then there is good probability that the barrier is indeed tunneling.

### Section 2.2: Coulomb Blockade and Conductance Oscillations [17]

If one fabricates a device on the nanoscale with two tunnel junctions creating a central island an interesting effect known as Coulomb blockade arises from the inherent quantization of electric charge. Capacitance is defined as $C = Q/V$, where Q is the electric charge on some structure, be it parallel plates, a sphere, or an island. The capacitive energy, U, stored on this structure is:

$$U = \int dU = \int V dq = \int_0^Q \frac{q}{C} dq = \frac{1}{2}\frac{Q^2}{C} \qquad (12)$$

Thus an electron can be added to a structure with n electrons already on it by an external charge $Q_{ext}$ when:

$$\Delta U = \frac{((n+1)e - Q_{ext})^2}{2C} - \frac{((ne - Q_{ext})^2}{2C} = 0 \qquad (13)$$

This equation is satisfied when $Q_{ext} = e(n + \frac{1}{2})$ and thus $V = \frac{Q_{ext}}{C} = \frac{e}{C}(n + \frac{1}{2})$. Starting with n = 0 (no charge on the device), at $V = \pm\frac{e}{2C}$ there will be a step in the current as an electron is allowed to overcome the Coulomb repulsion and transport onto the device structure (in the case of tunnel barriers, by tunneling onto the device). Thereafter, every e/C increase in voltage will result in another step in current, creating what is known as a Coulomb blockade staircase, and will create a spike in conductance, creating what is known as Coulomb conductance oscillations. If C is small enough (below 1 femptofarad (fF)), this effect is observable with reasonable voltages. These small capacitances are achievable using present nanolithography and materials growth techniques, where capacitances as small as in the attofarad (aF) range have been achieved. At higher temperatures, thermal activation ($\sim e^{-Ec/2kT}$) over the barrier will begin to 'wash-out' the steps in the I-V curves and the conductance peaks in the dI/dV curves. Besides having a low capacitance the thermal energy, kT, needs to be much less than $e^2/2C$ in order to observe the phenomena. However, for 10 aF, T is 92.8 K, thus a standard liquid He chamber which a low temperature of ~ 2 K could easily satisfy the temperature criteria for a small enough capacitance.

When fabricating devices on the nanoscale, another energy value to be aware of is the quantized energy levels of a particular geometry. The quantized energy levels for a structure of dimensions, $L_x$, $L_y$, $L_z$ are given by:

$$E_Q(n_x, n_y, n_z) = \frac{\hbar^2}{2m}\left[\left(\frac{\pi n_x}{L_x}\right)^2 + \left(\frac{\pi n_y}{L_y}\right)^2 + \left(\frac{\pi n_z}{L_z}\right)^2\right] \quad (14)$$

Capacitance is, in general, proportional to the size (length) of a device, for example a sphere has a capacitance of $4\pi\varepsilon_0 r$, thus C ~ L. Therefore the charging energy in electron volts goes as $e^2/4\pi\varepsilon_0 r$. For L large (>> $\lambda_F$), the Coulomb repulsion energy is much greater than the quantization energies. However, as L becomes small, on the order of $\lambda_F$ or smaller, the quantized energy steps of the structure become larger and more important than the Coulomb repulsion energy. Crossover occurs at ~ $\sqrt{\lambda_F a_B}$ , where $a_B$ is the Bohr radius (0.53 Å). For example, for an island on the order of 10 nm,

$$\Delta E_Q = \frac{\Delta\hbar^2 k^2}{2m} = \frac{\hbar^2}{2m}\left(\frac{\pi}{L}\right)^2 = 0.38\frac{eV}{L^2\,[\text{nm}]} = 3.8\,\text{meV}$$

$$\Delta E_C = \frac{e^2}{4\pi\varepsilon_0 L} = 1.44\frac{eV}{L\,[\text{nm}]} = 144\,\text{meV} \quad (15)$$

Coulomb blockade devices are usually fabricated as two tunnel junctions creating a central island. The capacitance of the device is then $C_{total} = C_S + C_{island} + C_D$. Often a third terminal is added to these double barrier Coulomb blockade devices connected to a voltage through a very thick tunneling barrier so that the voltage can only capacitively couple to the main device. In this manner the third terminal acts as a gate (with capacitance $C_G$) on the device. Now the total capacitance is equal to $C_{total} = C_S + C_G + C_{island} + C_D$ (see Fig. 1).

The advantage of using a gate is that a small bias can be placed across the source and drain leads without greatly upsetting thermal equilibrium and keeping the device in the Coulomb blockade regime. The gate voltage can then be used to control current flow by raising and lowering the energy of the device. At each $e/C_{gate}$ step in gate voltage there will be a subsequent peak in the source-drain current (left and right leads going through the double barrier). In this manner, if the source-drain were biased very close to $(n + ½)e/C_{total}$ a very small charge on the gate can cause a large spike in source drain current, resulting in huge effective gain. This three terminal Coulomb blockade device is called a single electron transistor and there are active areas of research and development in industry to utilize these devices to detect very small charges, down to a single electron, for highly accurate electrometers.

Up to this point, Coulomb blockade has only been treated classically, with the effect arising from the inherent quantization of charge. The charging of the island resulting in the Coulomb blockade occurs via first order tunneling. In this limit, at zero temperature, conductance goes completely to zero when the device has been Coulomb blockaded. However, Coulomb blockade only suppresses the sequential tunneling of charge where the process of electron transport through the device involves a real state in which the charge of the device changes by one-electron charge that raises the energy level above the Fermi values of the leads. In actuality, when a device is Coulomb blockaded, there will still be current from higher orders of tunneling involving two electrons, such as inelastic and elastic cotunneling and Kondo tunneling (tunneling via Kondo effect) which are described below. Even though these processes are of second order (or higher), they can become the dominant transport mechanism for single electron transistors in the Coulomb blockade regime.

Inelastic cotunneling occurs when the electron entering the device occupies a state different than a second electron, which is leaving the device, thus creating an electron-hole excitation on the device [18, 19] (see Fig. 2). The necessary conditions for this process to dominate is that the device be Coulomb blockaded and there be enough thermal or potential energy from an applied voltage to create the electron hole pair. In order for this to occur, the temperature needs to be less than the thermal energy needed to increase the conductance $G \sim e^{-Ec/2kT}$ above $2e^2/h$. Thus,

$$k_B T_{inelastic} << \frac{E_C}{2} \ln\left[\frac{hG}{2e^2}\right] \qquad (16)$$

At lower temperatures and voltages, elastic cotunneling becomes dominant [18-21]. In this process the electron coming onto the device occupies the exact same state as the electron leaving the device. In essence, the electron can be viewed as one-single electron doing the tunneling as there are no excitations left on the island. This process is a factor $1/nE_C$, where n is the density of states of the device, smaller than inelastic tunneling. For larger (not quantized) metallic devices, this process is not significant compared to inelastic cotunneling. For quantized devices with a limited number of states (as in a single-level quantum dots) this process is the dominant tunneling mechanism in the Coulomb blockade regime and occurs when

$$k_B T_{elastic}, eV << \sqrt{\frac{E_C}{n}} \qquad (17)$$

Another possible tunneling mechanism is the third order tunneling resulting from Kondo scattering. As will be described in the chapter on the Appelbaum-Anderson model, Kondo scattering occurs when an electron is forward scattered by a localized magnetic state through a spin exchange interaction. These localized states become present for tunneling through quantum dots when the top level is unfilled, thus the quantum dot is spin degenerate and acts as the localized moment. Kondo scattering occurs at temperatures and voltages in quantum dots exponentially smaller than elastic or inelastic tunneling due to a negative exponential dependence on $E_c/n$ and $e^2/hG$ in the probability of this effect occurring.

The devices for this research effort used metallic islands much greater in dimension than the Fermi wavelength. In addition, the lowest temperature at which the devices were characterized was ~ 2 K, and I-V characterization went to several volts. These factors thus preclude elastic or Kondo tunneling as being the dominant effect beyond Coulomb blockade. Thus, detailed discussion of second order tunneling processes will be limited to inelastic cotunneling.

### Section 2.3: Inelastic Tunneling For Double Barrier Devices

Following the development of Averin and Nazarov [18], for the three terminal single electron transistor, the charge on the island is defined by all three voltage sources (for consistency the left electrode shall be the source electrode and labeled as electrode 1 with voltage $V_1$ and the tunnel junction between it and the island with it shall be tunnel junction 1 with capacitance $C_1$. Likewise, the right electrode in figures is the drain and will be referred to with a 2 as will the junction to the drain electrode),

$Q = -(C_G V_G + C_1 V_1 + C_2 V_2) = ne$ (18)

When the island charge is changed from n to n+1 by an electron tunneling onto the island the change in charging energy is,

$$\Delta U = \frac{((n+1)e-Q)^2}{2C} - \frac{((ne-Q)^2}{2C} = \frac{e^2}{C}(n+\frac{1}{2}-\frac{Q}{e}) \qquad (19)$$

The energy change associated with tunneling in the first and second junctions is then the difference between the energy after the tunnel event and before the tunnel event:

$$E_1 = U(n+1,Q) - U(n,Q) = \frac{e}{C_{total}}[e(n+\frac{1}{2}) - V(C_2 + \frac{C_g}{2}) + C_g V_g]$$

$$(20)$$

$$E_2 = U(n-1,Q) - U(n,Q) = \frac{e}{C_{total}}[-e(n-\frac{1}{2}) - V(C_1 + \frac{C_g}{2}) - C_g V_g]$$

Using the Fermi Golden Rule to calculate the transition rates, Γ, from initial energy state, $E_i$ to final energy state $E_f$, in standard second order perturbation theory,

$$\Gamma_{if} = \frac{2\pi}{\hbar} | \sum_{\psi} \frac{\langle \psi_i | H^T | \psi \rangle \langle \psi | H^T | \psi_f \rangle}{E_{\psi} - E_I} |^2 \, \delta(E_i - E_f) \qquad (21)$$

letting $T_1$ and $T_2$ denote the tunneling matrices for the first and second junction. Referencing Figure 2, if the electron leaving $\text{lead}_1$ leaves the energy state with energy $E_a$ and tunnels to the higher energy state, $E_b$, on the island, and if the electron leaving the island, leaves a state $E_c$ and goes onto state $E_d$ on lead$_2$, then one can sum the amplitudes for each of these processes to occur first obtain,

$$\Gamma = \frac{\hbar}{2\pi e^4 R_1 R_2} \int \left( \begin{array}{l} dE_a dE_b dE_c dE_d f(E_a)(1-f(E_b)) f(E_c)(1-f(E_d)) \times \\ \left( \frac{1}{E_b - E_a + E_1} + \frac{1}{E_d - E_c + E_2} \right) \delta(eV + E_a - E_b + E_c - E_d) \end{array} \right) \qquad (22)$$

The above equation has utilized the fact that the absolute value of the tunneling matrices $T_1$ and $T_2$ are directly related to the tunneling resistances in junctions 1 and 2 ($R_1$ and $R_2$, respectively) by,

$$\frac{1}{R_i} = \frac{4\pi e^2}{\hbar} |T_i|^2 \; n_0 n_i \qquad (23)$$

where $n_0$ and $n_i$ are the densities of states of the central island and the leads at the Fermi level. At T = 0 K and for eV << $E_1$, $E_2$ then the transition rate can be explicitly determined:

$$\Gamma = \frac{\hbar}{12\pi R_1 R_2} \left( \frac{1}{E_1} + \frac{1}{E_2} \right)^2 V^3 \qquad (24)$$

For non-zero temperatures, but for eV << $E_1$, $E_2$ (which are close to the Fermi level which for metals is on the order of several volts), and utilizing f(-E)=1-f(E), the transition rate then becomes,

$$\Gamma = \frac{\hbar}{2\pi e^4 R_1 R_2} \left( \frac{1}{E_1} + \frac{1}{E_2} \right)^2 \int \prod_{i=a}^{d} (dE_i f(E_i)) \delta(eV + \sum_{i=a}^{d} E_i) \qquad (25)$$

Relating the forward and backward tunneling rates by $\Gamma(-V) = \exp(-eV / k_B T) \Gamma(V)$ and that the current is related to the forward and backward tunneling rates by

$I(V) = e[\Gamma(V) - \Gamma(-V)]$, Averin and Nazarov obtain an expression for inelastic tunneling at non-zero temperatures:

$$\boxed{I(V,T) = \frac{\hbar}{12\pi e^2 R_1 R_2}\left(\frac{1}{E_1} + \frac{1}{E_2}\right)^2 \left[(eV)^2 + (2\pi k_B T)^2\right]\cdot V \qquad (26)}$$

Thus, a linear and cubic term dependent current expression for inelastic tunneling current is obtained which will dominate in the Coulomb blockade regime.

# Chapter Three

## Simmons' Theory for Tunneling in Metal-Insulator-Metal Barriers

In 1963, John G. Simmons developed a generalized mathematical formula for the tunneling of electrons through a thin insulating film between two electrodes, a metal-insulator-metal (MIM) device [22]. Utilizing the Wentzel-Kramers-Brillouin (WKB) approximation, he was able to develop his formula for tunneling through a rectangular barrier with and without image force lowering. Later in 1964 he expanded his theory to incorporate thermal effects [23].

Tunneling is an inherently quantum mechanical process [24]. The physical basis for tunneling through a thin barrier is the smooth behavior of the probability density $\Psi^*\Psi$ across the metal-insulator interface. The reason for this is the exponential decay of the wavefunction for an electron at the Fermi energy. As the wavefunction enters the barrier the amplitude decays as $\exp(-\kappa x)$ where $\kappa \cong (2m/\hbar^2)^{1/2}\phi^{1/2}$ where x is the distance into vacuum or the insulator (in which case $\phi$ and m must be adjusted accordingly). The rate of tunneling through the barrier is dominated by this exponential decay where the potential energy V(x) exceeds the kinetic energy $E_x$. According to the WKB approximation the probability $D(E_x)$ that an electron can penetrate a potential barrier of height V(x) is given by,

$$D(E_x) = \exp(-2K) \quad (27)$$

$$K = \int_{s_1}^{s_2} \kappa(x, E_x)\,dx \quad (28)$$

$$\kappa(x,E_x)=\left(\frac{2m^*[V(x)-E_x]}{\hbar^2}\right)^{1/2} \qquad (29)$$

Thus,

$$D(E_x)=\exp\left[-\frac{4\pi}{h}\int_{s_1}^{s_2}2m^*[V(x)-E_x]^{1/2}\,dx\right] \qquad (30)$$

where $s_1$ and $s_2$ are the turnaround points (each edge of the barrier at the Fermi level), $m^*$ is the effective mass in the barrier and $E_x$ is the kinetic energy $m^*v_x^2/2$. Continuing with Simmons' procedure, the number $N_1$of electrons tunneling from $\text{lead}_1$ to $\text{lead}_2$ through the barrier is given by:

$$N_1=\int_0^{v_m}v_x n(v_x)D(E_x)dv_x=\frac{1}{m^*}\int_0^{E_m}n(v_x)D(E_x)dE_x \qquad (31)$$

where $E_m$ is the maximum energy of the electrons in the electrode and $n(v_x)dv_x$ is the number of electrons per unit volume with velocity between $v_x$ and $v_x + dv_x$. With an isotropic velocity distribution, the number of electrons per unit volume is given by,

$$n(v)dv_x dv_y dv_z=(2m^{*4}/h^3)f(E)dv_x dv_y dv_z \qquad (32)$$

where *f*(E) is the Fermi-Dirac distribution function.

Therefore:

$$n(v_x)=\frac{4\pi m^{*3}}{h^3}\int_0^{\infty}f(E)dE_r \qquad (33)$$

in polar coordinates where,

$$v_r^2=v_x^2+v_y^2 \text{ and } E_r=\frac{m^*v_r^2}{2}. \qquad (34)$$

Thus,

$$N_1 = \frac{4\pi m^{*2}}{h^3}\int_0^{E_m} D(E_x)dE_x \int_0^{\infty} f(E)dE_r \qquad (35)$$

Similarly if electrode two is at a higher potential than electrode 1 by a potential V, then:

$$N_2 = \frac{4\pi m^{*2}}{h^3}\int_0^{E_m} D(E_x)dE_x \int_0^{\infty} f(E+eV)dE_r \qquad (36)$$

and the net flow of electrons is N =N$_1$ – N$_2$:

$$N = \frac{4\pi m^{*2}}{h^3}\int_0^{E_m} D(E_x)dE_x \int_0^{\infty} [f(E) - f(E+eV)]dE_r \qquad (37)$$

Defining,

$$\zeta_1 = \frac{4\pi m^{*2}\, e}{h^3}\int_0^{\infty} f(E)dE_r \qquad (38)$$

and

$$\zeta_2 = \frac{4\pi m^{*2}\, e}{h^3}\int_0^{\infty} f(E+eV)dE_r \qquad (39)$$

letting $\zeta = \zeta_1 - \zeta_2$ then

$$J = \int_0^{E_m} D(Ex)\zeta dE_x \qquad (40)$$

With V(x) = η + φ(x), where η is the Fermi energy level, assume the width of the barrier, Δs, is relatively constant in the range between the kinetic energy of the particle (E$_x$) and the Fermi level (η). Also assume Δs is equal to the barrier width at the Fermi level, then:

$$D(E_x) = \exp\left[-\frac{4\pi}{h}(2m^*)^{1/2}\int_{s1}^{s2}(\eta + \varphi(x) - E_x)^{1/2}dx\right] \qquad (41)$$

This can be integrated using the approximation:

$$\int_{s1}^{s2} f^{1/2}(x)dx \cong \beta \overline{f} \Delta s \qquad (42)$$

where β is a correction factor for the approximation used as a measure of how much the function differs from its average value over the width of the barrier. β is defined in developing the approximation as:

$$\beta = 1 - \frac{1}{8\overline{f}^2 \Delta s} \int_{s_1}^{s_2} [f(x) - \overline{f}]^2 dx \qquad (43)$$

The average value of the function from $s_1$ to $s_2$ is defined as

$$\overline{f} = \frac{1}{\Delta s} \int_{s_1}^{s_2} f(x)dx \qquad (44)$$

where $\Delta s = s_2 - s_1$. The second term in β is generally much less than 1, thus β ~ 1. This leads to

$$D(E_x) \approx \exp[-A(\eta + \overline{\varphi}(x) - E_x)^{1/2}] \qquad (45)$$

where $\overline{\varphi}(x)$ is the mean barrier height above the Fermi level (using the function average definition above). A is defined by,

$$A = \frac{4\pi\beta\Delta s}{h}(2m^*)^{1/2}. \qquad (46)$$

At 0 K, then,

$$\zeta_1 = \frac{4\pi m^* e}{h^3}(\eta - E_x)$$

$$(47)$$

$$\zeta_2 = \frac{4\pi m^* e}{h^3}(\eta - E_x - eV)$$

$$\zeta = \begin{cases} \dfrac{4\pi m^* e}{h^3}(eV) & 0 < E_x < \eta - eV \\ \dfrac{4\pi m^* e}{h^3}(\eta - E_x) & \eta - eV < E_x < \eta \\ 0 & E_x > \eta \end{cases} \qquad (48)$$

Substituting the above into equation (40),

$$J = \frac{4\pi m^* e}{h^3}\left[\begin{array}{l} eV \int_0^{\eta - eV} \exp[-A(\eta + \overline{\varphi} - E_x)^{1/2}]dE_x - \overline{\varphi} \int_{\eta - eV}^{\eta} \exp[-A(\eta + \overline{\varphi} - E_x)^{1/2} dE_x + \\ \int_{\eta - eV}^{\eta} (\eta + \overline{\varphi} - E_x)\exp[-A(\eta + \overline{\varphi} - E_x)^{1/2} dE_x \end{array}\right] \qquad (49)$$

Performing the integration, one obtains for ,current density flowing through a generalized barrier:

$$J = J_o \left\{ \overline{\varphi} \exp(-A\overline{\varphi}^{1/2}) - (\overline{\varphi} + eV)\exp[-A(\overline{\varphi} + eV)^{1/2}] \right\} \qquad (50)$$

where,

$$J_o = \frac{e}{2\pi h(\beta \Delta s)^2} \qquad (51)$$

This is known as the Simmons' tunneling equation and can be interpreted as a current density $J_o(\overline{\varphi}\exp(-A\overline{\varphi}^{1/2}))$ flowing from electrode one to electrode two and a current density $J_o(\overline{\varphi} + eV)\exp[-A(\overline{\varphi} + eV)^{1/2}]$ flowing in the opposite direction yielding J as the net current density.

At moderate voltages where eV < φ (the barrier height), and letting Δs = s, the average barrier height, $\bar{\varphi} = (\varphi - \frac{eV}{2})$, and letting β = 1, then the Simmons equation becomes,

$$J = \left(\frac{e}{2\pi h s^2}\right)\left\{\begin{aligned} &\left(\varphi - \frac{eV}{2}\right)\exp[-\frac{4\pi s}{h}(2m)^{1/2}\left(\varphi - \frac{eV}{2}\right)^{1/2}] \\ &-\left(\varphi + \frac{eV}{2}\right)\exp[-\frac{4\pi s}{h}(2m)^{1/2}\left(\varphi + \frac{eV}{2}\right)^{1/2}] \end{aligned}\right\} \qquad (52)$$

which at relatively low voltages reduces to a linear and cubic term at the lowest orders:

$$J = J_L(V + \alpha V^3) + \ldots \qquad (53)$$

where,

$$J_L = \frac{(2m^*)^{1/2}}{\Delta s}\left(\frac{e}{h}\right)^2 \varphi^{1/2}\exp(-A\varphi^{1/2}) \qquad (54)$$

and

$$\alpha = \left[\frac{(Ae)^2}{96\varphi} - \frac{Ae^2}{32\varphi^{1/2}}\right] \qquad (55)$$

The conductance is given by $\partial J / \partial V$,

$$G = J_L + 3\alpha V^2 + \ldots \qquad (56)$$

and thus again parabolic conductance behavior is an indicator of tunneling.

Simmons subsequently incorporated image force lowering on the rectangular barrier by utilizing a parabolic approximation for the image force induced reshaping of the barrier. The barrier height as a function of x is then written as,

$$\varphi(x) = \varphi_o - \frac{eVx}{s} - \frac{1.15\lambda s^2}{x(s-x)} \qquad (57)$$

where $\varphi_o$ is the unlowered barrier height above the Fermi level, s is as defined before, and $\lambda = e^2 \ln 2/8\pi\varepsilon s$. Utilizing the average function value equation (44) and solving the integral, with the limits of integration ($s_1$ and $s_2$) determined from the roots of,

$$0 = \varphi_o - \frac{eVx}{s} - \frac{1.15\lambda s^2}{x(s-x)}. \qquad (58)$$

Simmons found an analytic solution can be obtained for $eV < \varphi_o$ with the following approximations good to second order,

$$s_1 = \frac{1.2\lambda s}{\varphi_o}$$

$$(59)$$

$$s_2 = s[1 - \frac{9.2\lambda}{3\varphi_o + 4\lambda - 2eV}] + s_1$$

Then one obtains for the image force lowered barrier, $\varphi_I$,

$$\bar{\varphi} = \frac{1}{s}\int_{s1}^{s2}\left\{\varphi_o - \frac{eVx}{s} - \frac{1.15\lambda s^2}{x(s-x)}\right\}dx = \varphi_o - \frac{eV}{2s}(s_1 + s_2) - \frac{1.15\lambda s}{(s_2 - s_1)}\ln\left[\frac{s_2(s-s_1)}{s_1(s-s_2)}\right] = \varphi_I \qquad (60)$$

Thus for an image force lowered barrier:

$$J = J_o\left\{\varphi_I \exp(-A\varphi_I{}^{1/2}) - (\varphi_I + eV)\exp(-A(\varphi_I + eV)^{1/2}\right\} \qquad (61)$$

where for $\beta = 1$,

$$J_o = \frac{e}{2\pi h s^2} \text{ and } A = \frac{4\pi s}{h}(2m^*)^{1/2}. \qquad (62)$$

Expanding the constants, expressing J in A/cm$^2$, $\varphi_o$ in V, and s, $s_1$ and $s_2$ in Å units, and with $\varepsilon$ as the dielectric constant, one obtains,

$$\boxed{\begin{aligned} &J(V) = \left(\frac{6.2x10^{10}}{s^2}\right) \times \left\{\varphi_I \exp(-1.025 s \varphi_I{}^{1/2}) - (\varphi_I + V)\exp[-1.025 s(\varphi_I + V)]\right\} \\ &\qquad\qquad\qquad\qquad\qquad\qquad\qquad\qquad\qquad\qquad\qquad\qquad\qquad\qquad (63) \\ &\varphi_I = \varphi_o - \left(\frac{V}{2s}\right)(s_1 + s_2) - \left(\frac{5.75}{\varepsilon(s_2 - s_1)}\right) \times \ln\left[\frac{s_2(s - s_1)}{s_1(s - s_2)}\right] \end{aligned}}$$

For V < $\varphi_o$

$$s_1 = \frac{6}{\varepsilon \varphi_o}$$

$$(64)$$

$$s_2 = s\left[1 - \frac{46}{3\varphi_o \varepsilon s + 20 - 2V\varepsilon s}\right] + \frac{6}{\varepsilon \varphi_o}$$

and for V > $\varphi_o$

$$s_1 = \frac{6}{\varepsilon \varphi_o}$$

$$(65)$$

$$s_2 = \frac{(\varphi_o \varepsilon s - 28)}{\varepsilon V}$$

With the area of a MIM tunnel junction and knowledge about the dielectric constant of the insulator, the barrier thickness, and expected barrier height, one can plot a curve of current versus voltage based on Simmons' tunneling equations.

The equations developed so far for MIM tunneling only take the applied voltage into account and neglect thermal effects (thus are for T = 0 K). To develop a general thermal dependence [23], Simmons assumed only electrons close to the Fermi level contributed to the tunneling, and simplified the probability of tunneling to,

$$D(E_x) = \exp(-A\overline{\varphi}^{1/2})\exp\left[\frac{-A(\eta - E_x)}{2\overline{\varphi}^{1/2}}\right] \qquad (66)$$

Incorporating temperature dependence of the Fermi-Dirac distribution functions into the current density equation, one obtains,

$$J(V,T)=\frac{4\pi m^{*}ekT}{h^{3}}\exp(-A\bar{\varphi}^{1/2})\int_{0}^{E_m}\ln\left\{\frac{1+\exp\left[\frac{\eta-E_x}{kT}\right]}{1+\exp\left[\frac{\eta-E_x-eV}{kT}\right]}\right\}\exp\left[\frac{-A(\eta-E_x)}{2\bar{\varphi}^{1/2}}\right]dE_x \quad (67)$$

where $E_m$ is the energy at the barrier maximum, which for normal metals and insulators is many kT above the Fermi level. Letting $E_m$ go to infinity, one obtains,

$$J(V,T)=\left(\frac{4\pi m^{*}e}{h^{3}B^{2}}\right)\left[\frac{\pi BkT}{\sin(\pi BkT)}\right]\exp(-A\bar{\varphi}^{1/2})[1-\exp(-BeV)] \qquad (68)$$

where $B=A/2\bar{\varphi}^{1/2}$, and again $A=\frac{4\pi\beta\Delta s}{h}(2m^{*})^{1/2}$. At T = 0 K, this reduces to, assuming $\bar{\varphi}>>eV$,

$$J(V,0)\cong\left(\frac{e}{2\pi hs^{2}}\right)\left\{\bar{\varphi}\exp(-A\bar{\varphi}^{1/2})-\bar{\varphi}\exp(-A(\bar{\varphi}+eV)^{1/2})\right\} \qquad (69)$$

Comparing to equation (5) obtained from the zero temperature case, one see that the only difference is the multiplier of the second term in the brackets which should be $(\bar{\varphi}+eV)$. This is a result of the approximations made, thus based on Simmons' development, we have a generalized thermal expression for the net current density in an MIM tunnel barrier,

$$\boxed{\begin{aligned}J(V,T)&=\left[\frac{\pi BkT}{\sin(\pi BkT)}\right]\left(\frac{e}{2\pi hs^{2}}\right)\left\{\bar{\varphi}\exp(-A\bar{\varphi}^{1/2})-(\bar{\varphi}+eV)\exp(-A(\bar{\varphi}+eV)^{1/2})\right\}\\&=\frac{\pi BkT}{\sin(\pi BkT)}J(V,0)\end{aligned}\qquad (70)}$$

# Chapter Four

## Zero-Bias Tunneling Anomalies: Appelbaum-Anderson Model

### Section 4.1: Overview

In 1933, an anomalous low-temperature resistivity increase not explained by theory was observed in alloy metals by W. J. de Haas, J. de Boer, and G.J. Van den Berg [25]. For the next several decades, anomalous resistivity/conductivity at low-temperatures in metals containing dilute magnetic alloys attracted much interest [26]. Starting in the 1960s, with advancing technologies and the ability to create tunneling barriers, Hall, Racette, and Ehreneich [27] found a dip in conductance (a peak in resistance) in III-V p-n tunnel junctions centered at zero bias whose magnitude depended on dopant concentration, dopant type, temperature and semiconductor used. Logan and Rowell in 1964 [28], studying Si and Ge p-n tunnel junctions, found a conductance peak for high dopant concentrations and a conductance dip for low dopant concentrations. They empirically determined that the conductance peaks varied as $-\ln[(kT+|eV|)/E_0]$. Also that year, Wyatt found that the effect also occurred in metal tunnel junctions separated by oxide barriers [29]. Wyatt found peaks in the conductance that behaved empirically the same as Logan and Rowell's peaks. Subsequently, there were many more discoveries of anomalous conductance peaks and dips in metal-metal oxide tunnel systems of various materials.

The first theoretical treatment of these anomalous behaviors was by J. Kondo in 1964 [30, 31]. A minimum in the temperature dependence of the resistivity of Au-Fe, Rh-Re etc. dilute magnetic alloys was explained by calculating the *s*-*d* scattering of the conduction electrons by the localized magnetic impurities. This third-order contribution to the scattering rate, thus resistance, was determined to be proportional to – ln T, an increasing contribution at low temperatures. Since then, the resultant strong scattering of electrons at the Fermi energy by isolated magnetic moments has been known as the Kondo effect, or Kondo scattering. This effect has been studied and observed for many physical systems such as dilute metallic alloys with magnetic features and tailored mesoscopic systems, such a quantum point contacts and quantum dots, where the d-levels in the magnetic impurities are mimicked by the degenerate states of the quantized system [26, 27].

Kondo's theoretical treatment was adopted in 1966 and further refined in 1967 by Joel Appelbaum [33, 34] to treat the case of near zero-bias tunneling anomalies. This followed a suggestion by P.W. Anderson that magnetic scattering in the oxide barrier may be important. Based on this, Appelbaum postulated that in junctions showing zero-bias anomalies, magnetic impurities were the source of magnetic moments originating from unpaired *d*-electrons of an isolated atom or ion located just inside the barrier near the metal-metal oxide interface. According to Appelbaum's theory, the conductance around zero-bias is expressed as a sum of three main contributions, which will be derived in detail below.

In brief, as seen in Figure 3, the first contribution comes from the electrons that tunnel through the barrier without interaction or that scatter from the impurity without any spin exchange. The second contribution takes into account spin exchange between the electrons and magnetic impurities and provides a magnetic field (H) dependent term that is independent of voltage in zero magnetic field. This contribution can be experimentally observed as splitting of the conductance peak into two peaks with each peak in the conductance at eV = +/- $g\mu_B H$ (thus the two peaks are separated by 2 $g\mu_B H$) which represents the threshold for exciting a Zeeman transition of the magnetic moment. Here g is the splitting factor (~ 2 for electrons) and $\mu_B$ is the Bohr magneton $(\mu_B = e\hbar/2m = 5.79x10^{-5} eV/T)$. Shen and Rowell first experimentally observed this effect in 1967 and 1968 [31]. The third contribution comes from electrons that are scattered by *s-d* exchange interaction of the electron spin with the localized magnetic states near the interface. This interaction can either forward scatter the electrons across the barrier (giving a conductance peak) or the electrons are scattered back into the source electrode (resulting in a conductance dip), depending on the relative spin alignment of the impurity and tunneling electron. This contribution gives rise to the anomalous logarithmic behavior of the conductance at low temperature and near zero-bias, $G_3 \sim -\ln[(kT+|eV|)/E_0]$ and is in essence the same physical effect as the Kondo effect. This process is often referred to simply as a Kondo tunneling process. Schrieffer and Wolf [35], found that the Hamiltonian developed by Anderson (who assisted Appelbaum in this theory) for a localized magnetic moment in a dilute magnetic alloy is equivalent in the limit of small *s-d* interactions as to the Kondo Hamiltonian and that both possess the same low temperature anomalies. The difference arises in that Anderson disregards the exchange interaction giving rise to spin-flip scattering processes that Appelbaum ultimately does include in his theory.

## Section 4.2: Detailed Development of the Appelbaum-Anderson Model [34]

The Anderson-Appelbaum model describes an assisted tunneling process and was theoretically treated using the transfer Hamiltonian approach (extended by Bardeen to solid-state structures in 1961 [24]). The Hamiltonian for the entire tunnel junction can be written a,:

$$H = \sum_i \frac{p_i^{2}}{2m} + \sum_i V(\vec{x}_i) + \frac{1}{2}\sum_{i\neq j} W(\vec{x}_i - \vec{x}_j) \qquad (71)$$

In second-quantization including all electron-electron interactions:

$$H = H_o + H_I$$

$$H_o = \int \psi^*(\vec{x})\left(\frac{p^2}{2m} + V(\vec{x})\right)\psi(\vec{x})d^3x \qquad (72)$$

$$H_I = \int \psi^*(\vec{x})\psi^*(\vec{x}')W(\vec{x}-\vec{x}')\psi(\vec{x})\psi(\vec{x}')d^3x d^3x'$$

where $H_o$ represents one electron interactions and $H_I$ two electron interactions. The states of interest are the conduction electron states on sides 'a' (left) and 'b' (right) of the tunnel junction, represented by $\varphi_{k\sigma}^{a}(x)$ and $\varphi_{k\sigma}^{b}(x)$, with wavevector (momentum) **k** and spin σ and with destruction operators $a_{k\sigma}$ and $b_{k\sigma}$ to destroy the electron on the respective sides. Assuming one localized electron confined to a region near the metal-metal oxide interface (a valid assumption as long as the spacing between localized magnetic impurities is much greater than the lattice spacing) with a destruction operator $d_\sigma$ that destroys the localized state of spin projection σ, one can write,

$$\psi(\vec{x}) = \sum_{k'\sigma'} a_{k'\sigma'}\varphi_{k'\sigma'}{}^{a}(\vec{x}) + \sum_{k''\sigma''} b_{k''\sigma''}\varphi_{k''\sigma''}{}^{b}(\vec{x}) + \sum_{\sigma} d_\sigma \varphi_{d\sigma}(\vec{x}). \qquad (73)$$

Putting this into the Hamiltonian, Appelbaum obtained a Hamiltonian grouped into those describing the electrode separately from those describing transfer and interaction:

$$H = H_1 + H_2 + H_3 + H_4 + H_5 + H_6 + H_7. \qquad (74)$$

Highlighting the significant aspects of this expression, the first term:

$$H_1 = \sum_{k\sigma} \varepsilon_{k\sigma}{}^{a} a_{k\sigma} * a_{k\sigma} + \sum_{k\sigma} \varepsilon_{k\sigma}{}^{b} b_{k\sigma} * b_{k\sigma} \qquad (75)$$

is the single-particle energies of the electrons on the left (a) and right (b) sides of the barrier.

$$H_2 = \sum_{k,k',\sigma} (T_{kk'} a_{k\sigma} * b_{k'\sigma} + T_{k'k} b_{k'\sigma} * a_{k\sigma}) + \sum_{k,\sigma} T_{kd}{}^{a} (a_{k\sigma} * d_{\sigma} + d_{\sigma} * a_{k\sigma}) + \\ \sum_{k,\sigma} T_{kd}{}^{b} (b_{k\sigma} * d_{\sigma} + d_{\sigma} * b_{k\sigma}) \qquad (76)$$

describes traditional tunneling from one side to the other with the probability determined by the tunneling matrix element $T_{kk'}$. The latter two terms describe the overlap of the localized d states with the conduction electrons on the 'a' and 'b' sides. The first terms involving interaction with the localized state are $H_5$ and $H_7$,

$$H_5 = \sum_{k,k',\sigma,\sigma'} W_{kk'}{}^{d} d_{\sigma} * a_{k\sigma'} * d_{\sigma'} a_{k'\sigma} + \text{Hermitian Conjugate} \qquad (77)$$

$$H_7 = \sum_{k,k',\sigma,\sigma'} W_{kk'}{}^{d} a_{k\sigma} * d_{\sigma'} * b_{k'\sigma'} d_{\sigma} + \text{Hermitian Conjugate} + \sum_{k,k',\sigma,\sigma'} W_{kk'}{}^{d} a_{k\sigma} * d_{\sigma'} * d_{\sigma'} b_{k'\sigma} \qquad (78)$$

$$+ \text{Hermitian Conjugate}$$

In $H_5$, the process described is for when the electron in the left hand metal interacts with the localized moment and the electron's spin projection is changed (while remaining in the left electrode). This is a spin-flip scattering event between the local moment and an electron near the electrode-barrier interface. $H_7$ represents the case for when the electron interacts with the localized moment and is simultaneously transferred through the barrier; in other words, a spin-flip tunneling process. In this process, the electron can tunnel through the barrier and appear with opposite spin on the other side and the localized moment can have its spin projection flipped.

Recasting the Hamiltonian with raising and lowering operators, $S^+$ and $S^-$, and dividing into three parts: a tunneling Hamiltonian, $H^T$, for terms moving the electron across the barrier, an interaction Hamiltonian, $H^I$, for electrons that stay on the same side of the barrier but their momentums or spin projections are changed through interaction with the localized state, and a self-energy Hamiltonian, $H_0$, which contains the energy of the electrons themselves (as in $H_1$) and the magnetic energy of the localized moment. Appelbaum obtains the following Hamiltonian for a system in a magnetic field **H** with side 'a' at voltage V:

$$H = H_0 + H' \tag{79}$$

$$H_0 = \sum_{k\sigma} \varepsilon_{k\sigma}{}^{a} a_{k\sigma} * a_{k\sigma} + \sum_{k\sigma} \varepsilon_{k\sigma}{}^{b} b_{k\sigma} * b_{k\sigma} + g \,|\, \mu_B \,|\, \vec{S} \bullet \vec{H} \tag{80}$$

$$H' = H^T + H^I \tag{81}$$

$$\begin{aligned} H^T = {} & T_J \sum_{kk'} S_z [(a_{k\uparrow} * b_{k\uparrow} - a_{k\downarrow} * b_{k'\downarrow}) + (b_{k'\uparrow} * a_{k\uparrow} - b_{k'\downarrow} * a_{k\downarrow})] + \\ & T_J \sum_{kk'} S^+ (a_{k\downarrow} * b_{k'\uparrow} + b_{k\downarrow} * a_{k'\uparrow}) + T_J \sum_{kk'} S^- (a_{k\uparrow} * b_{k'\downarrow} + b_{k'\uparrow} * a_{k\downarrow}) + \\ & T \sum_{kk'\sigma} (a_{k\sigma} * b_{k'\sigma} + b_{k'\sigma} * a_{k\sigma}) + T_a \sum_{kk'\sigma} (a_{k\sigma} * b_{k'\sigma} + b_{k'\sigma} * a_{k\sigma}) \end{aligned} \tag{82}$$

$$H^I = J \sum_{kk'} \left\{ S_Z (a_{k\uparrow} * a_{k'\uparrow} - a_{k\downarrow} * a_{k'\downarrow}) + S^+ a_{k\downarrow} * a_{k'\uparrow} + S^- a_{k\uparrow} * a_{k'\downarrow} \right\} \tag{83}$$

If one assumes an **H** field in the z direction, then the last term of $H_0$ becomes $\Delta S_z$, where $\Delta$ is the Zeeman splitting of the localized spin, $g|\mu_B|H$. In $H^T$ the terms involving $T_J$ describe spin-flip tunneling; those involving T and $T_a$, describe direct tunneling not involving the localized impurity (T) or scattering from the impurity without spin exchange ($T_a$). The interaction Hamiltonian, $H^I$, is the second-quantization of the *s-d* exchange interaction $H^{s-d} = -2J\vec{S} \bullet \vec{\sigma}$. Using the Fermi Golden Rule to third order, given by,

$$W_{i,j} = \frac{2\pi}{\hbar}\left\{ |H'_{ij}|^2 + \sum_{k \neq i} \frac{H'_{ik}\, H'_{kj}\, H'_{ij}}{E_i - E_k} + \text{Hermitian Conjugate} \right\} \times \delta(E_i - E_j) \qquad (84)$$

where i and $E_i$ represents a conduction electron-localized spin state and its energy, respectively, to determine transition probabilities, Appelbaum found three conductance terms,

$$G = G_1 + G_2 + G_3 \qquad (85)$$

$$G_1 = \frac{4\pi e^2}{\hbar} \rho^a(\varepsilon_F) \rho^b(\varepsilon_F) \left\{ T^2 + N_a 2TT_a + N_a T_a{}^2 \right\} \qquad (86)$$

$$G_2 = \frac{4\pi e^2}{\hbar} \rho^a(\varepsilon_F) \rho^b(\varepsilon_F) N_a \left\{ S(S+1) T_J{}^2 + T_J{}^2 \frac{\langle M \rangle_{av}}{2} \left( \begin{array}{l} \tanh \dfrac{eV + \Delta}{2k_B T} + \\ \tanh \dfrac{\Delta - eV}{2k_B T} \end{array} \right) \right\} \qquad (87)$$

$$G_3 = G_{31} + G_{32} + G_{33} \qquad (88)$$

$$G_{31} = C\left\{ 1 - \frac{\langle M^2 \rangle_{av}}{S(S+1)} + \frac{\langle M \rangle_{av}}{2(S+1)S} \left( \tanh \frac{eV + \Delta}{2k_B T} + \tanh \frac{\Delta - eV}{2k_B T} \right) \right\} \rho(\varepsilon_F) \ln \frac{|eV| + k_B T}{E_0} \qquad (89)$$

$$G_{32} = \frac{C}{2}\left\{1 + \frac{\left\langle M^2 \right\rangle_{av}}{S(S+1)} + \frac{\left\langle M \right\rangle_{av}}{S(S+1)}\left(\tanh\frac{eV+\Delta}{2k_BT}\right)\right\}\rho(\varepsilon_F)\ln\frac{|eV+\Delta|+k_BT}{E_0} \qquad (90)$$

$$G_{33} = \frac{C}{2}\left\{1 + \frac{\left\langle M^2 \right\rangle_{av}}{S(S+1)} + \frac{\left\langle M \right\rangle_{av}}{S(S+1)}\left(\tanh\frac{\Delta-eV}{2k_BT}\right)\right\}\rho(\varepsilon_F)\ln\frac{|eV-\Delta|+k_BT}{E_0} \qquad (91)$$

$$C = -\left(\frac{8\pi e^2}{\hbar}\right)S(S+1)\rho^a(\varepsilon_F)\rho^b(\varepsilon_F)N_aT_J{}^2J \qquad (92)$$

where $\rho^a(\varepsilon_F)$ and $\rho^b(\varepsilon_F)$ are the density of electron states on each side of the junction, $N_a$ is the number of non-interacting localized magnetic impurities, <M> is the average magnetization of the localized spins, Δ is as defined before, and $k_B$ is the Boltzman constant. $G_1$ proportional (~) to $(T+Ta)^2$ describes direct tunneling (or tunneling with no spin exchange), $G_2 \sim T_J{}^2$, describes magnetic field dependent spin-flip tunneling, and $G_3 \sim T_J{}^2J$.,which at zero magnetic fields is ~ -ln[(|eV|+nkT)/$E_0$], gives rise to the zero-bias Kondo tunneling anomalies (tunneling assisted by s-d exchange resulting in forward or backward Kondo scattering across the barrier). Appelbaum included multiple localized moments with the result that every term with a $T_J$ or J is multiplied by $N_a$ (as would be expected).

The magnetic field dependence of $G_2$ has been observed [31] and the splitting of the peaks with a width of $2g\mu_BH$ is physically understood as the tunneling electrons exchanging spin with the localized moment, requiring at least $g\mu_BH$ of energy. Thus if every electron flipped its spin, then $G_2$ should go to 0 when $|eV| < g\mu_BH$. However, only

S/S(S+1) of electrons will spin-flip in this manner, thus the maximum amount will be for S=1/2. At zero temperature up to 2/3 of electrons will not tunnel due to spin-flip effects when $|eV| < g\mu_B H$ (thus $G_2$ is reduced to a third of its zero magnetic field level).

Experimental evidence has shown that the Appelbaum-Anderson model is quite accurate for tunnel junctions that exhibit a zero-bias conduction peak or dip that is small in comparison ( ~ 10 % or less) to the entire conductance. In addition, experimental evidence has shown at high magnetic fields the spin-flip tunneling process is the dominant behavior [31, 36-38].

# Chapter Five

# Scanning Probe Nanolithography By Anodic Oxidation

## Section 5.1: Overview

In 1990, J. A. Dagata and associates reported that they were able to oxidize hydrogen-passivated silicon (Si) (111) surfaces with 200 nm line widths 1-20 nm deep using a scanning tunneling microscope (STM) [10]. Dagata and other researchers [10-15, 39-42] found that with a conductive scanning probe microscope tip and a conductive stage on which the Si wafer was mounted in an atmosphere of some ambient humidity or in oxygen gas (in the case of an STM), a voltage on the order of a few volts applied either to the tip or stage would form $SiO_2$ underneath where the scanning probe tip was located. The thickness and width of this oxide was found to depend on: write speed; voltage; whether the bias was pulsed or DC; the use of p- or n- type wafers; and ambient humidity. In an ambient humid environment, a meniscus of water several nanometers thick forms on surfaces. When the tip is negatively biased with regards to the Si, the bias disassociates the water into $H^+$ and $OH^-$ ions and present oxygen into free $O^+$ and $O^-$ radicals (see Fig. 4). The hydroxide/oxide ions are driven by the field through any present surface oxide where they combine via an electrochemical reaction with the passivated Si at the $Si/SiO_2$ interface. For Dagata and the other research groups, passivation was accomplished by dipping Si wafers in a dilute hydrogen fluoride (HF) solution after a standard RCA (named after Radio Corporation of America) clean (bathing wafers in a hydrogen peroxide ammonium hydroxide mix which cleans off insoluble organic materials, followed by a dip in dilute HF to clean off a thin oxide layer formed in the first step, followed by a bath in hydrogen peroxide in hydrochloric acid to remove ionic and heavy metal atoms) or other clean. The HF dip removes any remaining $SiO_2$ layer formed during the RCA clean and the surface is left with a passivated surface of Si-H bonds. The reaction is: $2H_2O + 2Si{:}H + 2O_2 \rightarrow 2OH^- + 2Si^+ + 2O^{2-} + 2H^- + 2O^{2+} + 2H^+ \rightarrow 2SiO_2 + 2H_2O + H_2$. The remaining hydrogen either combines with oxygen to form water from the present electric field or dissipates on its own.

Typical parameters for the anodization of Si using this process are to follow the wafer cleaning step with a 1 – 25% HF dip, use tip voltages in the range of -2 – -25 V (-2 to -10 V most common), write speeds of 0.1 μm/s -100 μm/s, and use conducting tips such as Ti coated $Si_3N_4$, heavily doped silicide tips (e.g. Ni-silicide), PtIr coated Si-tips (used normally for scanning capacitance microscopy (SCM), or Co coated tips (used for magnetic force microscopy (MFM)). If done using an atomic force microscope (AFM), the process is usually done in a clean room, which normally has a 30 – 40% ambient humidity. Using these values, line widths for anodization of Si:H range from 10 – 100 nm with a thickness of 1 – 10 nm.

As might be suspected, scanning probe microscope based anodization is not limited to hydrogen passivated silicon. Hiroyuki Sugimura and associates [12] first oxidized titanium by this method, and Kazuhiko Matsumoto's group has as well [13]. Additionally, niobium (Nb) [43], aluminum (Al) [11], and gallium and aluminum gallium aresenides (GaAs/AlGaAs) [44, 45] have all been anodized with scanning probe lithography. The line widths generated for each material differs as their oxidation potentials differ, but still fall in the tens of nanometers range for width and single nanometers for depth.

For this research effort, to fabricate tunnel barrier devices using this method and to expand to other materials, an incremental process was used to develop the techniques and determine the parameters necessary to perform nanolithography with the equipment utilized. For this work, a Digital Instruments (now part of Veeco Instruments) 3000 atomic force microscope with Nanoscope IIIa controller [46] (see Fig. 5) was used for the nanolithography. The control software for this AFM includes an option to apply a bias to the tip (the plate on which the wafer or sample sits is then connected to ground) through its Ana2 channel (analog channel 2). The control software provided a bias up to +/- 15 V DC on this channel when activated. To achieve higher voltages, a battery and rheostat control switch was connected through a Digital Instruments breakout box, which had a direct connection to the circuit applying the voltage to the tip. The Digital Instruments control software also allowed programming of the movement of the tip. In this manner, voltages, write speed, and pattern of the oxide could be controlled.

## Section 5.2: AFM Nanolithography of Silicon

The first step in this process was to acquire the ability to produce oxide lines on silicon. The most difficult part in this process was learning the software and controls for the Digital Instruments AFM. This is especially true when there are software upgrades which change syntax and location of the controls to turn on and off the ability to control voltage on Ana2 (referred to as aoana2 or lsana2 in the lithography software depending on version). The latest version used of the Windows 3.1 driven software (4.43r1) also required the input attenuation to be turned off.

Obtaining AFM tips well suited to this application also involved trial and error. Cr tips were initially used and worked, but they were no longer sold. PtIr SCM and Ni-silicide tips both worked for nanooxidation. The PtIr tips worked best and were used most for this research effort. However, for even the PtIr tips, the performance varied from tip to tip, even for those fabricated from the same wafer.

Once the software and tip requirements for oxidation were met, the process for performing the actual nanolithography was straightforward. First n-type (100) Si wafers were cleaned using a self-made Piranha etch; a 2:1 mixture of sulfuric acid ($H_2SO_4$) and hydrogen peroxide ($H_2O_2$) for a period of 10 minutes to clean off insoluble organics. Then the wafers were dipped in a 25% HF bath for two minutes to remove any oxide and to hydrogen passivate the surface, then blown dry with $N_2$. The wafers were then placed on the AFM sample plate and held down with vacuum. The ambient humidity in the clean room was monitored over several weeks and found to maintain a relatively constant humidity of 35% +/- 1%. Therefore, humidity was not a variable in developing the nanolithography parameters.

Using the AFM control software, several diamond/box shapes were drawn to develop the writing process (all lithography programs are included in Appendix A). A pattern of lines at increasing write speeds was then drawn. Found was that at a bias of - 8 V at 0.5 μm/s, the line widths were approximately 80 nm. At - 6 V at 10 μm/s, the thickness of the lines was reduced to 50 nm (see Fig. 6). Thus, the ability to perform

AFM nanolithography on Si was accomplished and a well formed UT with 80 nm line width was drawn (see Fig. 7).

### Section 5.3: AFM Nanolithography of Titanium and Nickel

Once AFM nanolithography on silicon was achieved, lines of $TiO_2$ were created. 30 – 50 Å of Ti was electron beam (e-beam) deposited with a CHA Industries (company named after Carl Hermann and Associates) e-beam evaporator on 1000 Å of $SiO_2$ thermally grown by dry oxidation at 1100 $^{o}$C on n-type Si (100) wafers. How to connect the top Ti conducting layer to ground was the next difficult step to determine. Open literature does not report the details on how this step is accomplished. Probe leads were tried, but they tended to either scratch through the thin metal or conduction was so low across the wafer that oxidation was not achieved. Also, the probe leads interfered with the operation of the AFM probe head. Copper (Cu) tape was tried as was silver (Ag) conducting paint along the edge. Again conductance across the wafer to the contact point was too low for oxidation. In the case of the tape, the adhesive prevented contact. Additionally, coating the entire backside with Al in the e-beam evaporation chamber in an attempt to also coat the sides and then etching off with Al etch after oxidation did not work as the top never did make a good contact with ground. The successful method discovered and which was used for all the lithography for this research, wrapped the wafer in aluminum foil (leaving the area to be oxidized open) and used Ag conducting paint from GC Electronics to ensure a good contact between the top surface and the foil. In addition, Teflon tape was used to secure the foil to a metal block which was then vacuum mounted to the sample stage of the AFM. This method also had the advantage of being easy to apply and remove without any metal etchants being required (methanol was employed to clean off the Ag paint).

After the sample was mounted in the AFM as described, box patterns were once again drawn to see if oxidation of Ti could be accomplished. Indeed, $TiO_2$ lines were drawn, requiring a bit more voltage and slower write speed than with Si. Line widths from 25 nm up to 110 nm were drawn with voltages ranging from - 9 V at .05 μm/s and - 10 V at 0.1 μm/s creating 25 – 30 nm line widths and - 12 V at .05 μm/s creating over 100 nm line widths, as demonstrated in Figure 8. Due to the lack of uniformity in the deposition and oxidation process and proximity to the grounding contact, oxidation was found to vary across the sample surface. Again a UT was drawn with 90 nm lines to mark success (see Fig. 9). The electrochemical process for the anodization of Ti is: $Ti + 2H_2O \rightarrow Ti^{4+} + 4e^- + 2OH^- + 2H^+ \rightarrow TiO_2 + 2H_2$.

Once the nanooxidation process was established for Si and Ti, new materials were considered. To date there had been no studies performed on AFM oxidized tunnel devices fabricated with ferromagnetic materials. In addition, most TMR devices utilize non-magnetic metal oxides for the tunnel barrier. As the industry could perhaps use an oxide with magnetic properties to save process steps, Ni was chosen as its oxide is generally antiferromagnetic, but can also assume other properties depending on preparation. Ni was thus obtained and oxidation studied. For these Ni samples, the metal was patterned in the device structure to eventually be used for the tunnel barrier devices so parallel development of the optical lithography steps and nanolithography steps could be conducted. The devices for this study were formed in a three step process. First the metal to be oxidized is deposited on the oxide, thus 80 - 90 Å of Ni was e-beam deposited on the $SiO_2$ layer, in an optical lithography defined pattern. The pattern consists of three 10 µm x 10 µm pads connected in a T-structure with 1 µm lines (see Fig. 10). Then ~ 500 Å of Al is e-beam evaporated in a pattern of 50 µm wide lines that go from the 10 µm pads to 100 µm wide lines that stretch to the edge of the sample. These leads are connected to the Al foil for anodization and also serve as the probe and packaging leads for device characterization, as shown in Figure 11. The final step in device fabrication is to oxidize the internal T-junction with a pattern to confine transporting electrons through defined oxide structures.

For the purposes of establishing the ability to oxidize Ni, some simple patterns were first drawn in the T-junction. Due to the lower oxidation state of Ni (0.25 V) versus Ti (1.63 V), Ni oxidation depended much more on the surface conditions and wear of the AFM tip, thus would produce patterns in agreement with what was programmed into the AFM control software at about half the rate of Ti. The electrochemical reaction for Ni anodization is: $Ni + H_2O \rightarrow Ni^+ + OH^- + H^+ + e^- \rightarrow NiO + H_2$. Tips normally wear from being dragged across the surface during AFM imaging. Performing oxidation increases this wear as the tip too can build up oxide material. Often an AC pulse or positive voltage after writing is used to 'discharge' the oxide from the tip. A double "X" pattern was drawn on 85 Å Ni at - 7 V, 0.3 µm/s that resulted in a very apparent oxide with 200 – 300 nm line widths and thickness going over 10 nm (see Fig. 12 (a)). The oxidation of Ni via scanning probe lithography has yet to be reported in the open literature. The lines are quite clumped with oxidized islands of Ni. Subsequently, a - 6 V, 1 µm/s write of a single “X” created an even more clumped “X” shape (Fig. 12 (b)). Using a lesser voltage, an “X” was attempted at a - 4 V bias at 0.5 μm/s, but resulted in a carrot “^” shape (Fig. 12 (c)). However, the line was much more clear with no clumping or “islands”, the line width was approximately 300 nm.

What was obvious was that oxidation of Ni was more difficult to control. As some of the roughness of the Ni may be from the thin amount of Ni deposited on the oxide and oxide build up on tips can cause rough oxidation, lines were drawn on one sample with 159 Å of Ni deposited on 2400 Å of wet-oxidation grown $SiO_2$. This was accomplished using a -10 V amplitude square wave pulse from an Hewlett Packard 3314A Function Generator operating at 10 Hz. Three samples from this effort are shown with line widths from 85 nm to 150 nm at write speeds from 0.02 to 0.04 μm/s (see Fig. 13). The lines did not show as much clumping, but were much wider due to the slow write speeds needed to instigate oxidation (when write speeds were quicker no oxidation occurred when the bias was pulsed).

The Ti lithography process was also further refined through use of the actual device metal “T” pattern. Again simple tunnel barrier lines were drawn, this time on 220 Å of Ti on 2400 Å $SiO_2$ wet-oxide, to ensure that nanolithography could be done on the photolithographically defined device layer. Four samples are shown where the barrier lines were each written using a 10 Hz pulse at 0.1 μm/sec at - 7 V for two of the samples, - 8 V for the third sample, and - 9 V for the fourth. Resultant line widths ranged from 80 – 150 nm (see Fig. 14).

From these studies, the parameters for Ti and Ni oxidation were determined to be in the - 4 – -15 V range with write rates in the range of 0.1 to 1.0 μm/s in order to generate a measurable oxide.  For device fabrication, the difficulty lies in obtaining visible oxidation, controlling the pattern and still having thin enough barriers to allow tunneling.  Due to these limitations, the yield of this AFM nanooxidation process in producing useful devices was approximately 5%.  The description of the actual fabricated devices characterized for this effort will be discussed in Chapter Six.

# Chapter Six

# Device Fabrication and Characterization

## Section 6.1: Choice of Devices for Study

Single electron transistors (SET's) featuring Coulomb blockade effects and ferromagnetic tunnel junctions with spin-dependent tunneling magnetoresistance (TMR) peaks and zero-bias anomalies have been a subject of great interest [47-53]. While zero-bias anomalies have been discussed, and the basic concept of TMR introduced previously in Chapter One, a brief review of the physics behind TMR have not been discussed.

In 1975, Julliere proposed the first theory to explain TMR [47]. In his study he measured the current-voltage characteristics of Fe-Ge-Co tunnel barriers. While he too found Appelbaum's zero-bias anomalies, what was most significant about his work is that he put forth the first theoretical description of TMR. He proposed, based on the work of Tedrow and Messervey [54], the change in conductance (and by inverse the resistance) from parallel (p) to antiparallel (ap) alignment of a tunnel junction with two different ferromagnetic leads depended on the relative spin polarizations of the two electrodes. Namely,

$$\frac{\Delta G}{G} = \frac{G_p - G_{ap}}{G_p} = \frac{2P_1P_2}{1+P_1P_2} = \frac{R_{ap} - R_p}{R_a} = \frac{\Delta R}{R} \qquad (93)$$

where $P_1 = 2a_1+1$ and $P_2=2a_2-1$ are the polarizations of the respective electrodes and where $a_1$ and $a_2$ are the fractions of tunneling electrons in electrodes 1 and 2 (respectively) whose magnetic moments are parallel to the magnetization of their respective material. Since this study, the work of Julliere has been adopted as the reference expression for TMR ratio and percentages, and recently has lead to much work, both experimentally and theoretically. The TMR effect is not only of interest due to the application for magnetic field sensors for hard drives as mentioned in the first chapter, but also there is interest from a basic science standpoint on new interesting phenomena being observed in magnetic tunnel junctions.

Recently, magnetoconductance/magnetoresistance studies have been done on ferromagnetic SETs to reveal the interplay between Coulomb blockade effects and TMR for various tunneling structures including:

$Co/Al_2O_3$/Co-cluster/$Al_2O_3/Co$ double junctions [55]

Ni/NiO/Co/NiO/Ni double junctions [51, 56, 57]

$Co/Al_2O_3$/Permalloy ($Ni_{80}Fe_{20}$) junctions of various design [58]

Co/NiO/Ni/NiO/Co double junctions [51, 57]

$Al/Al_2O_3/Co/Al_2O_3/Al$ double junctions [51, 57]

Ni-Fe/Co/Al-O/Co/Al-O/Co/Ni-Fe/FeMn/Co and Ni-Fe/Co/Al-O/Co/Al-O/Co/Al-O/Co ferromagnetic-granular-ferromagnetic junctions [59].

These studies most often found that TMR was enhanced in the Coulomb blockade regime and was attributed to spin-polarized tunneling [47, 51, 56-60]. In sputter-deposited junctions [55], TMR was found not to depend on whether or not the devices were operated in the Coulomb blockade regime. However, except for Ootuka, et al., who looked at $Al/Al_2O_3/Al/Al_2O_3/Al$ double junctions [51 ,57], there are no other reported studies of magnetoconductance in completely normal-metal/oxide/normal-metal/oxide/normal-metal double junction devices. In addition, all of the above devices' tunnel junctions were formed using standard microelectronic fabrication techniques (deposition by evaporation or sputtering, and etching).

Another technique for forming SETs has been developed using the atomic force microscope (AFM) based nanolithography process discussed earlier [12-14]. Using this technique Matsumoto and co-workers have fabricated SETs using Ti/$TiO_2$/Ti tunnel junctions with 2-5 junctions [13] and Nb/NbO/Nb tunnel junctions [43] that have operated at room temperature. Tunnel devices formed using AFM nanolithography are planar devices, where current flows parallel to the device surface and not perpendicular to the surface as in devices fabricated through layered deposition of material. However, to date, experimental results other than the authors [60] on magnetic field effects on current conduction mechanisms in tunnel junctions and SETs formed using SPM nanolithography or in planar Coulomb blockade tunnel devices, for that matter, have yet to be reported [61-65]. One of the reasons for this is that AFM nanolithography can result in incomplete oxidation of the oxide barrier due to the imprecise morphology of the deposited metal on an oxidized Si surface. Also, planar junctions are not currently of interest to those studying devices for use as magnetic field sensors. In addition, electron transport laterally through thin layers of metal depends on the smoothness of the deposited metal. However, this is advantageous when wanting to fabricate devices with clusters of unoxidized metal particles surrounded by the metal-oxide dielectric. In this situation, the device structure resembles that of studies where purposely-made granular tunnel junctions [52, 59] or tunnel junctions doped with impurities [50, 55] were utilized. The devices for our study utilize a Ti/$TiO_2$/Ti /$TiO_2$/Ti tunnel junction or a Ni/NiO/Ni tunnel junction where the oxide barrier is fabricated using AFM nanolithography. An intentionally unoxidized region of Ti is left in the middle of the Ti device (a Ti island) and unoxidized Ni particles are left embedded within the NiO. Ni was chosen as it is a ferromagnetic material, yet single-crystal NiO is antiferromagnetic (NiO nanoparticles have been shown to vary from superparamagnetism to super antiferromagnetism with increasing particle size [66]) and also can be a semiconductor depending on how the oxide is grown. Granularity of the titanium and nickel is a byproduct from the deposition process onto the $SiO_2$ surface. Figure 15 shows a sample surface after metallization. Note the grain size which provides some indication as to expected roughness.

## Section 6.2: Device Fabrication

### Oxidation

Devices were made by first growing approximately 1000 Å of $SiO_2$ in a dry $O_2$ environment at 1100°C for 40 minutes on a n-type Si (100) wafer in the furnaces at the University of Texas Microelectronics Research Center (MRC). Local operating procedures were utilized with the four power settings on the oxidation furnace set to Left Channel: ~800, Center Channels: ~550/~550, and Right Channel: ~ 900. Each user needs to independently verify temperatures for each power setting (using the same power setting temperature could vary as much as $25^{o}$ C). Thickness was confirmed by ellipsometry with a Nanospec B ellipsometer and the deep blue color of the wafer.

### Photolithography

The devices were then patterned using photolithography in the III-V bay at MRC using a Karl Suss MJB-3 Mask Aligner. Through trial and error, and changes due to new lamps, filters, and a new mask, a process was developed that gave relatively predictable results. As most users in this bay were using line widths on the order of hundreds of microns versus the desired one micron for this effort's mask, and the base material for this work was $SiO_2$, not GaAs, a new process had to be established. The 5" mask for this effort was purchased from DuPont photomask for approximately $1000, although prices are dependent on specifications. As described in the previous chapter, the mask had two layers for metallization. One defining a small "T" with 1 micron line widths and second with wide leads that went to the edge of the sample.

To photolithographically define the samples, the newly oxidized wafers were cleaved into pieces approximately 1-1.5" on the edge, rinsed with deionized (DI) water, then given a three step cleaning in acetone, methanol and isopropyl, then rinsed again with DI water. The sample pieces were then baked at $150^{o}$ C to remove any remaining water or solvents for a period of 10-15 minutes. Then primer and AZ5209 photoresist (meaning it leaves 0.9 μm thick resist after spinning at prescribed values) were each spun on at 4000 rpm for 40 seconds. The sample pieces were then placed in a $90^{o}$ C oven to pre-bake for 11 minutes. Meanwhile the mask was loaded onto the Karl Suss mask aligner. The procedures used for the Karl Suss aligner are included in Appendix B. While the samples were being exposed for 8 minutes, an AZ 4025 developer bath was prepared. After exposure, the samples were dipped for 8 – 9 seconds in the developer. Quality of the lithography process is checked by use of microscopes in the III-V bay. Usually this process allowed 1.5 – 2.5 μm line widths to be made from the 1 μm line width mask.

## Metallization and Lift-off

After the first layer was photolithographicaly patterned, the Ti and Ni device layers were formed by using a CHA electron beam (e-beam) evaporation tool to deposit 89 Å of Ti and 85 Å of Ni at ~5 $x10^{-6}$ Torr in the defined pattern onto the $SiO_2$ surface. The standard procedures for using the CHA e-beam evaporator at MRC were used. However, as most users were depositing 500 Å, 1000 Å, 2000 Å, or more of metal, there are some issues to be aware of when using the e-beam evaporator to do relatively quite thin metal layers. The metal thickness for the Ti, Ni and Al layers were determined by the evaporation control module on the CHA, which utilizes a resonating quartz crystal to measure film thickness. The first suggestion is to ensure the crystal used to measure thickness is relatively new (at least 50% crystal remaining), one may need to buy new Inficon 6 MHz gold quartz crystals. The second suggestion is to not use too high of a power. Step up the power level slowly and open the shutter when the metal first becomes white hot. There is no need to go over 3 – 5 Å/sec when only going to 80 Å, or else the operator may miss the desired mark. Use fresh wafer-mirrors, the mirrors can be fabricated during the aluminum device layer growth. Seeing the crucible clearly greatly assists electron beam alignment. When performing aluminum deposition, go very slowly and put only 5 or 6 slugs worth of Al into the crucible. Aluminum's melting-solidification process will crack crucibles. Slightly cracked crucibles can be used, but a crucible full of Al will result in significant breakage and spilling of molten Al. Final advice is to obtain new crucibles (~$35 each) and metals as not to have to borrow and rely on other research groups to keep materials in stock.

After the metal deposition, the photoresist pattern was removed to leave just the metal device layer on the device. This was accomplished through a lift-off process in an acetone bath in a sonic cleaner. Often an acetone soak of 5 minutes was required before and after. In the end, one uses acetone until the photoresist and unwanted metal are removed. After this liftoff process the results are checked in the III-V bay's microscope. Figure 16 shows a Scanning Electron Microscope (SEM) image of a typical device layer. The line width is 2 microns, which as mentioned is usual when this process works. There are many times when one or more of the steps did not work, for any apparent reason. To form the external contacts, the second external lead pattern was aligned to the first using the lithography procedures. ~ 500 Å of Al (503 Å for the Ti and 520 Å for Ni devices) was subsequently electron beam evaporated onto the Ti or Ni layer to provide a contact lead for wire bonding. Figure 11, again, shows a cross section schematic of the devices fabricated prior to nanolithography.

### AFM Nanolithography of Tunnel Barrier Devices

After metal deposition, the samples were then placed on a probe station where current-voltage (I-V) measurements were made across the devices to ensure a good contact was present, and that the nanolithography process was indeed creating a tunnel barrier. Using a Hewlett Packard 4140B picoamp (pA) meter, I-V curves at room temperature were made and the sample resistances were usually around 1 kΩ. Leakage through the $SiO_2$ was tested by measuring the resistance from the top leads to the ground of the sample holder. This resistance at room temperature was on the order of 1 TΩ.

The samples were then placed on the Digital Instruments AFM. The top contacts were connected to the electrical ground of the AFM using the Al foil (with only 50 – 100 Ω resistance between the Al lead and ground). Conducting Scanning Capacitance Microscope (SCM) probes utilizing PtIr-coated Si were used.

For the tunnel barriers, the goal of fabrication was to make the barriers as thin as possible (thinnest line achieved through nanolithography was 25 nm) with as small as junction area as achievable through modification of the write-speed and voltage bias on the tip. One limit on this process is that although capacitance decreases as 1/L and linear with area, the tunnel current decreases exponentially with thickness and linearly with area, and the smallest detectable currents is on the femptoamp level. In addition, being able to detect the pattern with the AFM after writing was also a limiting factor on how thin and small the junctions could be. The ability to measure tunnel current was not tested until device characterization. The devices described below are those for which barriers and tunneling currents were measurable.

For the Ti device, using a - 12 V bias on the probe tip at a draw rate of 0.3 μm/sec, an oxide pattern was formed using the AFM's control software to restrict current flow to a narrow point in the center of the cross bar. Likewise, a - 9 V bias at a draw rate of 1.0 μm/sec was then used to form the two tunneling barriers, intentionally leaving an unoxidized metallic island in the center (see Fig. 17). As shown in Figure 18, the barrier thicknesses are approximately 65 nm and 95 nm and the metallic island area is approximately 45 nm wide measured using the AFM profiling software. The resultant tunneling barrier oxide is approximately 3 nm thicker in depth than the Ti (yielding ~12 nm total $TiO_2$ thickness). Many other Ti devices were made as well with varying write rates and bias of the oxidation. Three of these are shown in Figure 19, and are referenced as Ti device 2, 3 and 4. These devices also used - 12 V at 0.3 μm/sect to constrict the flow, but the tunnel barriers in Ti 2 used - 8 V at 0.7 μm/sec for the tunnel barriers, Ti 3 used - 8 V at 0.5 μm/sec, Ti 4 used - 8 V at 1.5 μm/sec. Figure 20 shows the AFM profile measurements of Ti devices 2 and 4, with 47 and 44 nm line widths, respectively.

For the Ni device, a - 4 V bias was used at 0.75 μm/sec to constrict the electron flow to the tunnel barrier and a - 3.5 V bias was used at 1.0 μm/sec to create the two tunnel junctions (see Fig. 21). The tunnel junctions ended up placed near or on each other, so that instead of a double barrier device there was one large central oxide 345 nm across with a length of 400 nm. But due to the voltages and write-speeds used, the presence of unoxidized particles within the oxide was predicted, thus the device was still tested. This was the only 'clean' Ni device made due to the difficulty in oxidizing Ni predictably (see Chapter Five on SPM Nanolithography). This was one of the reasons for going to the simple single tunnel barrier during the nanolithography development phase.

Fabricated devices were subsequently tested at room temperature on a probe station to ensure the resistance was greater than twice the resistance quantum (one for each junction in series) from Landauer's conductance theory, $R_Q = 12.9\ k\Omega\ (= h/2e^2)$ (as discussed in Chapter Two). This ensures excess electron charges would localize on the central island so that it could hold charge for Coulomb blockade. The device resistances at room temperature were on the order of 1 MΩ for the Ti devices. For the Ni devices, the resistance was on the order of 100 GΩ. Devices that met this criteria were packaged and tested while dipped into liquid $N_2$ at 77K to eliminate most of the thermally activated current and to increase the relative contribution from the less temperature dependent tunneling current. At this temperature, resistances generally increased into the GΩ regime. Devices exhibiting parabolic conductance and roughly cubic current behavior were determined to be tunneling devices and were subsequently placed on a sample mounting rod for liquid He cryostat testing.

### Packaging and Mounting

After being pre-tested on the probe station, samples were packaged into a Kyocera 0.5 cm x 0.5 cm square flat-pack with 10 tungsten-gold leads on a side with ceramic alumina as the insulator (see Fig. 22). Kyocera charged $3500 per order of up to 100 packages. Obviously 100 packages were ordered. Samples were hand scribed and cleaved to fit. Transistor silicone grease heat sink compound was then applied sparingly with the back end of a laboratory cotton swab to the top of the package surface where the sample would be placed. The sample was then inserted using the grease as an adhesive. The samples were then placed on a Westbond 7400A wire-bonder at MRC. As the author obtained training and repair for this wire bonder, which had not been used in years, the procedures are included in Appendix C.

After packaging, the devices were mounted onto the end of a sample rod for the LakeShore Cryotronics 9500 Hall Measurement system [67]. The sample mount has six pins which connect to the triax connectors at the top (see Fig. 23) and contains a thermocouple and is thermally connected to a large copper block which has its own thermocouple (see Fig. 24). The sample mount and the large copper block each have their own heater. The sample mount's heater is lower power but provides finer control of temperature than the larger heater. The packages were mounted using the silicone thermal grease to thermally connect to the sample mount. The leads of the devices to be tested in the package were then soldered to the pins.

### Section 6.3: Characterization Equipment and Methods

The packaged samples mounted on the sample rod were then placed in the LakeShore Cryotronics 9500 Series Hall Effect Measurement system with liquid He cryostat located at the Air Force Research Laboratory. The system has a 9 Tesla superconducting magnet using a LakeShore 620 Magnet power supply. A LakeShore 340 Temperature controller was used to manually control the temperature within 0.1 K using P-I-D settings for the large heater of 80/40/10 and for the smaller heater set to 40/0/1. A Keithley Instruments 6430 Sub-Femtoamp Remote Source-Meter [68] was used with a guarded cable to connect to the pin-outs of the sample-mounting rod (see Fig. 23).

#### Noise Reduction/Averaging Technique

The alternating polarity measurement method, as described in a Keithley Instruments White Paper [69], with a frequency of 166 millihertz (mHz) (bias every 6 seconds) was used to simulate a DC response while eliminating spurious currents not stimulated by the voltage down to the fourth order (using ten readings for each bias, thus 20 current readings in total per current measurement). This method was developed by

Keithley researchers who saw a need when doing measurements on ultra-high resistance devices to eliminate currents from piezoelectric effects and discharging capacitive elements. The alternating polarity method works by changing bias from V to – V at a low enough frequency such that the sample can go beyond its RC delay constant. This is done several times at the same voltage, with each value of current being measured and averaged by weighting each term with the binomial coefficients of that order down to which accuracy is desired. For instance to correct for any non-DC stimulated current abnormalities down to second order one would use,

$$I_{calc} = \frac{I_1 + 3(-I_2) + 3(I_3) + (-I_4)}{8} \qquad (91)$$

thus $G_{calc}=I_{calc}/V$ would give a conductance corrected for any second order effects. For this experiment, as mentioned, corrections were done down to fourth order, so,

$$I_{calc} = \frac{I_1 + 5(-I_2) + 10(I_3) + 10(-I_4) + 5(I_5) + (-I_6)}{32} \qquad (92)$$

To even better improve the accuracy, the Keithley white paper suggested allowing the measurement system reach steady state after initiating the measuring process. Keithley determined that by not including the first couple of data points, the calculated current would be within 1% of steady-state values. For this experiment, four measurements were made prior to the six used to determine the calculated current, and the first calculated data point was not used for each bias resulting in a total of twenty measurements per current value.

### Software and Manual Controls

Using National Instruments LabVIEW software to control the Keithley 6430 and the LakeShore 620 Magnet supply, the bias was swept from -3 V to 3 V in 0.1 V steps and measurements were taken under swept magnetic fields at -9, -5, -1, -0.5, -0.4, -0.3, -0.2, -0.18, -0.16, -0.14, -0.12, -0.10, -0.08, -0.06, -0.04, -0.02, 0.00T and likewise back up to 9T, then reversed. Temperature was manually controlled using the system's temperature controller and data was taken at ~2 K, 10 K, 25 K, 50 K, 150 K and 300 K. The front end of the LabVIEW software programmed by the author allows one to input a file name to save the plus and minus data points from the alternate bias method, plus the ending calculated current for both the 1/3/3/1 coefficient process with four measurements to measure stimulated current to the second order and the 1/5/10/10/5/1 coefficient process to measure stimulated current to fourth order. The program also allows the operator to see I-V, R-V and G-V plots. The program automatically controlled the superconducting magnet and allowed the user to stop the data taking process and set delays for measurement. For these measurements the delay was set to 6 seconds after the applied voltage. The LabVIEW printout is included in Appendix D.

### Liquid Helium Cryostat Operation

There are certain steps necessary to proper running of the cryostat. Procedures are included in Appendix E. The magnet operation is controlled using the LabVIEW sub-vi software control, with 1 A of current providing 1-T of field. When going to the first -9 T, the operator needs to do the increase slowly (in 0.5 T steps at maximum) or else the magnet will quench and boil-off 50% of the He. When first cooled down, the superconducting magnet which sits in the He bath is at the same temperature as the He.

When a current is first applied the magnet is still cold, but will then start to heat from a very limited amount of Joule heating which can be countered with the liquid He. If the applied current is too high, while at first there will be very little voltage drop, the magnet will quickly heat up faster than the He can cool it.  This causes the magnet to start going non-superconducting, creating heat build-up leading to a quench.

# Chapter Seven

# Data and Analysis

## Section 7.1: Ti Devices

Figure 25 (a), (b), and (c) show the I-V curves for the Ti 1 device at 1.8 K, 10 K and 50 K with and without a 9 T applied magnetic field (applied so that a positive field points up through the sample). Note that step-like features, while difficult to visually discern in the I-V curve with no applied magnetic field, appear clearly in the I-V curve with the application of the magnetic field up through 50 K. To more clearly illustrate this, Figure 26 (a)-(c) show the differential (dI/dV) conductance mathematically derived from experimental current-voltage data in arbitrary units for the device at these temperatures with and without a magnetic field. The device shows a clear parabolic conductance behavior, demonstrating tunneling, which is notably flattened with magnetic field. Note as well, clear conductance oscillations are observed, and the period of these oscillations, ~ 250 – 300 mV, does not change with application of magnetic field. In addition, when the magnetic field is applied, the magnitude of the oscillation peaks greatly increases, the peaks become more refined, and additional peaks begin to appear. At 1.8 K a zero-bias conductance spike is also seen in Figure 26 (a). This feature was also seen in Ti device 2 as shown in Figure 27. Ti device 2 also exhibited an enhancement in both the Coulomb blockade staircase and conductance oscillations with the application of a 5T field. The zero-bias anomaly in both devices disappeared with application of magnetic field and increase of temperature. In Ti device 1, as the temperature was increased from 10 to 50 K, the conductance decreased. This is attributed to the increase in scattering in the metal leads and that at low temperature the electrons are not tunneling through the $SiO_2$. As shown in Figures 28 and 29, (a) and (b), for 150 K and 300 K, the clear conductance oscillations disappeared, even with a magnetic field and the I-V curves are almost strictly linear with a very slight cubic bend at higher voltages at room temperature as thermally excited carriers begin to dominate. For comparison, Matsumoto and associates $TiO_2$ I-V and dI/dV curves are shown in Figure 30.

## Analysis and Discussion

The general overall parabolic shape of the conductance and linear behavior (with cubic or exponential rise at higher voltages) in the I-V plots at low temperatures indicates tunneling through the entire metal-insulator-metal-insulator-metal junction as described by Simmons' tunneling theory. For the double-barrier devices in this study, this tunneling mechanism should dominate in the high voltage regime where Coulomb blockade effects of the device are washed out by large numbers of high-energy electrons tunneling through the barriers. In this regime, the electrons are only limited by the individual tunneling processes of each barrier, and thus the conduction will primarily be limited by the thicker barrier.

In addition to standard single-barrier tunneling processes, for a device with multiple tunnel barriers in the Coulomb blockade regime, inelastic cotunneling of two electrons through the barriers and elastic tunneling of one electron simultaneously through the multiple barriers becomes significant as Coulomb blockade only suppresses the sequential tunneling of electrons through the junctions. In the Coulomb blockade regime, inelastic tunneling dominates elastic tunneling when eV or kT is much greater than the Coulomb blockade energy, $E_{cb}$, and for large metallic islands with a large density of states (as in these devices). Thus, while inelastic cotunneling is of the second order in tunneling conductance, this process is dominant in the Coulomb blockade regime for these devices.

The conductance oscillations and steps in the I-V curves are attributed to Coulomb blockade effects from the double barrier tunnel junction with an unoxidized Ti center. The period of these oscillations is approximately 250 – 300 mV and corresponds to a capacitance from Coulomb blockade of $C=e/\Delta E_{cb} \sim 0.6$ aF. The oscillations are present without a magnetic field, and conductance oscillations due to the creation of Landau levels create an approximate energy spacing of $\Delta E_{Landau}= \hbar B/m^* = 0.42$ mV (using an effective mass for titanium ~2.5 times the electron mass and B = 9T). This is much less than the observed oscillations, thus the oscillations are not attributed to Landau levels in the unoxidized central island or in trapped particles within the oxide.

To estimate the capacitance of the junction, the tunnel barriers are treated as parallel plate capacitors, and the cubic island capacitance is estimated using the capacitance of an isolated sphere, $C = 4\pi\varepsilon\varepsilon_r r$, where r is the effective radius and the relative permittivity, $\varepsilon_r$, of $TiO_2$ have been determined for $Ti/TiO_2/Ti$ tunnel junctions by Matsumoto to be 5 [13]. This value is significantly different from the permittivity values of 40 – 86 determined by other studies on vertical $TiO_2$ tunnel junctions formed using chemical-vapor deposition [70]. Not only was the fabrication process different for these devices, but the devices also had much larger areas typical of standard photolithography processes (μm$^2$). The lower dielectric constant will result in lower capacitance values, thus Matsumoto's value is most likely a lower limit for $TiO_2$ (reflected in that he was able to achieve 1 eV charging energy steps in his Coulomb blockade devices). The barrier width values measured with the AFM, as shown in Figure 31, are utilized to generate first estimates of the capacitance. To calculate the effective radius, an approximation method is utilized that sets the surface area of a sphere, $4\pi r^2$, equal to the cubic shape whose capacitance is being estimated and solve for r. Using this method, one obtains the capacitance of a 1m$^3$ cube to be 77 pF, which is in good agreement with the numerically calculated value of 73 pF [71]. Applying this method, we determine the effective radius to be 48 nm, and the island capacitance to be 27 aF. The 75 nm tunnel barrier capacitance is determined to be 1.41 aF, the 95 nm barrier capacitance is 1.11 aF and the top and bottom barrier capacitances are approximately 0.20 aF. Taking into account the parallel and series capacitances, once can sum these values to obtain a total capacitance of 1.01 aF. Compared to the capacitance determined from the observed oscillations, 0.6 aF, the actual effective electrical thicknesses and areas result in capacitance values about 60% of what the AFM measurements would give. This is not unrealistic as the actual portions of the tunnel barriers that significantly participate in the electron transport processes can be quite different from fabricated values [72] and is in line with other nanoscale research efforts estimates on capacitance [17, 19].

Using the theories for Simmons' tunneling through a single barrier and inelastic cotunneling in the Coulomb blockade regime, a fit was performed using a Mathcad program (included in Appendices F and G) on the measurements at 1.8 K with and without a 9T magnetic field (see Fig. 32). To fit the inelastic cotunneling equation, capacitances equivalent to 60% of the AFM measurement derived capacitances, as described above, were used. In addition, the total tunneling resistance was determined to be ~1 MΩ from the zero voltage resistance at T = 300 K (at low temperatures Coulomb blockade will mask the pure tunneling component). The resistance (and subsequently the voltage drop across each barrier) was assumed to be proportional to each barrier's thickness (a good assumption to the first order as the devices are made of the same material). The number of electrons contributing to charging on the island, n, was used as a fitting parameter. Using the area of the AFM formed tunnel barriers (9 x 265 $nm^2$) and utilizing the published barrier height for a Ti/$TiO_2$ junction fabricated using AFM nanolithography of 0.308 eV [13] , the Simmons' fit yielded a thickness of 39 – 40 nm. This barrier height is less than the 3.0 eV band gap and 1.0 eV barrier height reported for standard thin-film $TiO_2$ and $TiO_2$-Si junctions [70], respectively, but agrees well with the ~1.0 eV band gap (and thus an ~0.5 eV barrier height) measured of $TiO_2$ nanoparticles on a Au substrate [73]. The thin-film devices in these other studies were made using standard fabrication processes, thus were not close to the size of this effort's device barriers. The $TiO_2$ nanoparticle paper of Datar, et al., is closer to the composition of the barriers of this paper, and the nanoparticles were determined to have sub-band gap defect sites which reduced the bulk $TiO_2$ band gap from 3.0 eV to 1.0 eV [73]. The oxide barriers in this device (and other SPM lithography formed barriers) most likely have similar defects (such as unoxidized metal particles). While fitting the theoretical equations at 1.8 K, it was found that the inelastic cotunneling current was dominant at lower voltages while the Simmons' current through the entire device had the dominant effect at higher voltages, as predicted by theory. The number of electrons charging the island was determined to be ~ 233. To account for parallel leakage paths in the experimental apparatus not accounted for in this comparison with theory, an ohmic resistance was used as a fitting parameter to align the curves using that at near T = 0 K and low voltages, conductance should be nearly zero in the Coulomb blockade regime. Using this method the parallel leakage resistance was determined to be 1 TΩ. At higher temperatures, the conductance will have a non-zero component according to inelastic cotunneling and MIM theories. However, the metal will also decrease in conductance due to increased scattering, and at higher temperature there will also be increased thermionic emission currents. These processes make it difficult to isolate the pure tunneling component of the current at higher temperatures for a comparison with theory, thus only a comparison with the 1.8 K data was done. That the determined Simmons' barrier thickness is ~ 41% of the larger AFM measured barrier thickness is not surprising as the entire tunnel barrier area was assumed to be electrically effective, while in actuality the effective tunnel area can be as low as 1% of the total junction area [24, 72]. In addition, any impurities present in the oxide, such as unoxidized Ti particles or other contaminants, can effectively reduce the electrical thickness of the barrier. Also, the $TiO_2$ barrier height used for this fit was empirically determined from a similar, but not identical, Ti/$TiO_2$ barrier. To verify the presence of cotunneling currents, this same theoretical curve was fit to the conductance and I-V curves with a -9T field at 1.8 K. In addition to the increased resistance due to increased scattering in the metal leads as the electrons are induced by the Lorentz force to complete cyclotron orbits, inelastic cotunneling currents should also be suppressed in the presence of a magnetic field. Spin-flip scattering according to Appelbaum-Anderson theory and the splitting of spin-up and spin-down states will restrict the cotunneling of two electrons through both barriers in the presence of an intense magnetic field. As the spins in each lead are in general aligned (thus each lead is polarized), only if the carriers maintain their spin alignment will there be a high probability of tunneling (as in the TMR effect). With scattering centers this is less likely to occur. In addition, applying a strong magnetic effect effectively halves the available density of states in the leads and island resulting in a halving in all tunneling transition calculations using the Fermi Golden rule which depends linearly on the energy density of states. In fitting the I-V and conductance curves for the case with magnetic field, the offset resistance was increased to 1.5 TΩs, thus taking into account the increased scattering in the leads. In addition, the cotunneling component was reduced by 50% as shown in Figure 32. Thus the lower voltage part of the conductance, attributed to the inelastic cotunneling currents, is suppressed while the higher voltage component (yielding tunneling through the entire device) is relatively unchanged. In addition, as earlier mentioned, the conductance oscillations have a much greater amplitude as inelastic cotunneling through the designed barriers are restricted, resulting in only sequential tunneling (limited by Coulomb blockade) being primarily observable.

The presence of spin-flip scattering centers was evidenced by a zero-bias anomaly peak at T = 1.8 K in Ti device 1 and T = 2.4 K in Ti device 2 with no magnetic field (see

Fig 27). This is indicative of impurities in the tunnel barrier which could lead to the thinner value for the barriers (40 vs 90 nm in Ti device 1) than is measured with the AFM. The conductance peak is indicative of “s-d” exchange processes according to the Appelbaum model for localized paramagnetic states within a transition metal-metal oxide tunnel junction, which typically originate from unpaired d electrons of an isolated transition metal or atom [24]. Data indicates the majority of transition metal-metal oxide junctions experience a conductance peak due to these trapped particles [24, 31, 36]. Although Ti particles have been indicated to create a resistance peak [37], impurity concentrations can affect the presence conductance or a resistance peak [74]. As Ti is used as a reactant to absorb particles in getter pumps, impurities from the metal evaporation process are expected to be present in the oxide [38]. Observed in the data for the Ti devices tested, the central conduction peak becomes a dip with magnetic field, attributed to the central peak being split and spread by spin-flip processes (Appelbaum’s second magnetic field dependent term). The peak reduces in height with voltage and disappears as temperature is raised according to s-d exchange scattering resulting in Kondo tunneling (Appelbaum’s third conductance term). The zero-bias conduction peak anomaly behavior of the devices tested in this paper also agrees with the results of authors who did not try to include impurities or defects in their tunnel junctions, but whose results, none the less, indicated the presence of such impurities [48, 49].

At 150 and 300 K, the conductance oscillations are washed out, even with a magnetic field, and the zero-bias anomaly is no longer present as carriers are thermally excited through the barriers or over it according to thermionic emission at microamp levels. Thermionic emission and current from thermally excited trapped states in the $SiO_2$ and tunnel barriers dominate the small tunneling currents and subsequent Coulomb blockade effects, which are relatively independent of temperature. Thus true electron tunneling and Coulomb blockade behavior of these devices are only observable at 50 K and below. By applying a strong magnetic field, much of the cotunneling current is eliminated yielding the clearer conductance oscillations.

## Section 7.2: Nickel Devices

Figures 33 and 34 show the I-V and dI/dV differential conductance plots with and without a 9T field at 10 K, 25 K and 150 K. Again the current steps and conductance oscillations are clarified by the application of an applied magnetic field and at low temperatures the minimum of the conductance is reduced to nearly zero. The oscillations are not attributed to Landau oscillations as they are present without a magnetic field. At 10 K, the conductance oscillations appear to shift by +100 mV with applied magnetic field, by 25 K the conductance oscillations for with and without a magnetic field are nearly out of phase. By 150 K the distinct oscillations have been over taken by thermally activated carriers (I~exp(-Ea/kT)) hopping through the barriers by traditional tunneling and the I-V curves exhibit classical linear & cubic dependence (approaching exponential). However, with the increased tunneling through the device a broad zero-bias conduction peak becomes observable (see Fig. 34 (d)).

## Analysis and Discussion

From the ~ 300 – 400 mV period of the oscillations at low temperature one can determine that $C_{CB} \sim e/\Delta V_{cb} \sim .45$ aF. As this device had no detectable island nor individual tunneling barriers, the oscillations were determined to come from charging of unoxidized Ni particles embedded within the oxide. As was done in Schelp, et al. [55], with their device made of Co particles embedded in $Al_2O_3$, one can similarly consider approximately spherical Ni particles embedded in the NiO barrier and the capacitance can be estimated from the capacitance of an isolated sphere, $C = 4\pi\varepsilon_o\varepsilon_r r$. For NiO, the relative permeability $\varepsilon_r$ is 11.9 [75]. Using this formula, the size of the Ni particles responsible for the Coulomb oscillations are approximately 6 – 8 Å. From the scaling laws discussed in the second chapter, one immediately recognizes that for this size of particles embedded in the oxide, quantum effects would dominate. Indeed, using $\Delta E_Q \sim 0.38/L^2$ eV (L in nm = 0.4), one obtains ~ 1 eV, much larger than the observed oscillations. One then comes to the conclusion that tunneling is occurring through the quantized energy levels of the device vice the Coulomb blockade energy levels. If this were true, the actual particle size would be determined from $L^2 \sim 0.38$ eV/(~ .3 - .4 eV), which gives a particle of diameter ~ 1 nm, which agrees well with the expected size of Ni grains deposited during metallization (1 – 5 nm in size) after partial oxidation (oxidation consumes roughly half of the Ni per growth, so 10 nm of growth consumes ~ 5 nm of Ni). A 1 nm Ni particle in NiO would have a Coulomb blockade energy of ~ 240 mV. The uniform shift in coulomb oscillation peaks with magnetic field is attributed to the magnetic field creating an effective gate charge on the device. It is concluded that this effect was not present (or not as strong) in the Ti devices as scattering prevented charging of the gate oxide, wile in the Ni devices the tunnel barrier itself became the effective gate.

In the 150 K curves, the I-V behavior indicates that Coulomb blockade from any individual particle has been washed out by thermally activated carriers. As described by theory [17] and observed in experiment [55] (see Fig. 35), a distribution of nanoparticles in a Coulomb blockade device acts collectively. Therefore, the staircase will not be visible and the I-V curve will be exponential in nature. Why the Ni particles in the barrier do not act collectively at lower temperatures in this device is not entirely clear. Perhaps at 10 K the carriers are localized and do not have enough thermal energy to activate a statistically significant number of particles. This is confirmed by the fact that at ~ 2 K there was no clearly measurable current through the barrier, indicating that measurable conduction through such a thick barrier (~ 350 nm) may require the activation of trapped impurities embedded within the oxide (such as unoxidized Ni particles). At 10 K there is enough energy to activate a few particles to create tunnel channels through them, resulting in the clear oscillations distinctive to those particles. At higher temperatures, more carriers within the oxide are activated, creating multiple tunneling paths through the oxide using multiple particles as intermediaries, thus resulting in a collective Coulomb blockade effect. Also observed at 150 K is a zero-bias anomaly indicative of scattering states in the tunnel barrier. Figure 34 (d) illustrates that the peak also lowers with application of magnetic field, this can be a result of spin-flip scattering from the embedded particles creating an effective TMR effect, with TMR % = $G_{0T} – G_{9T}/G_{0T} = 3.8\%$.

At low temperatures, the enhancement in clarity of the Coulomb blockade staircase, increase in conductance oscillation amplitudes, and reduction of conductance minimums to zero with the application of a magnetic field is again attributed partly to suppression of higher-order tunneling currents. However, due to the likely ferromagnetic/antiferromagnetic nature of this device, the spin-alignment of electrons tunneling through the antiferromagnetic NiO to the Ni particles is expected to also be sensitive to an applied magnetic field.

# Chapter Eight

# Conclusions

This research effort was undertaken to advance the understanding of nanolithography techniques and electron transport in nanoscale tunnel devices. Such research is crucial not only from a purely scientific standpoint, but also to provide a reservoir of knowledge for the electronics industry as current transport and fabrication at the nanoscale becomes critical for a multitude of current and future technologies.

There have been multiple studies available in the literature, both theoretical and experimental, on single electron transistors, ferromagnetic tunnel junctions, and ferromagnetic single electron transistors which have observed Coulomb blockade phenomena, TMR phenomena and the effects of Coulomb blockade on TMR, and zero-bias tunneling anomalies indicative of magnetic field dependent spin-flip tunneling and bias and temperature dependent Kondo tunneling. However, only a very few of these devices were fabricated using AFM nanolithography, and no AFM fabricated devices have been studied with a magnetic field. These studies are important to develop affordable lithography techniques for research institutions and to increase understanding of tunneling dynamics in various oxide barriers, especially magnetic properties, as TMR based devices will play a crucial role in future electronics technology.

To this end Ti/$TiO_2$/Ti/$TiO_2$/Ti double-barrier tunnel devices and Ni/NiO/Ni tunneling devices exhibiting Coulomb blockade were manufactured using AFM nanolithography. Coulomb conductance oscillations were enhanced by the addition of a magnetic field, which is attributed to the suppression of inelastic cotunneling (where two electrons simultaneously tunnel through both barriers of the tunnel device creating an electron-hole excitation) and higher order tunneling processes. This is the first reported observation of this effect. Conductance oscillations were observed up to 50 K in both types of devices, after which thermally activated currents dominated up to room temperature. Zero-bias anomalies were also observed in both the Ti and Ni devices.

In the analyzed Ti device, the conductance oscillations were observed to have an approximately 250 – 300 mV period, which agreed well with the capacitance determined from AFM measurements of device dimensions and from dimensions determined from a data fit to Simmons' and inelastic cotunneling theory. The Simmons fit yielded a barrier thickness approximately 41% of the AFM measured value and this is attributed to interface states in the titanium dioxide and to the entire junction area not contributing to the tunneling current, which is dominated by the thinnest portions of the tunnel barrier. Performing a fit to the theory of inelastic cotunneling with Coulomb blockade, the inelastic cotunneling component was found to decrease by 50% with the application of a magnetic field. In addition, the linear magnetoresistance through the leads was found to increase by 50% to 1.5 TΩ with the application of a magnetic field. The appearance of a zero-bias conductance peak at low temperatures with no magnetic field is indicative of impurities in the oxide, such as unoxidized titanium or other contaminants from the fabrication process, which can create localized magnetic moments from the unpaired *d* electrons of an isolated transition metal impurity in the insulating barrier. These scattering states are one of the reasons for the reduction in inelastic tunneling current with magnetic field.

For the Ni device, Coulomb oscillations were observed with a period of ~400 mV, attributed to charging of unoxidized quantum sized nanoparticles on the order of 1 nm in diameter. As in the case for the Ti device, the conductance oscillations became clearer and conductance was suppressed with application of a magnetic field. The oscillations were overcome by thermally activated tunneling above 50 K. However, at 150 K collective Coulomb blockade was indicated from embedded unoxidized Ni (or other) particles in the barrier. At this temperature, this device too exhibited a very thermally broadened zero-bias anomaly peak in the conductance, which was shown to lower slightly with application of a magnetic field. This slight lowering was attributed to the embedded particles creating a minor TMR effect through spin-scattering processes.

To date no authors have reported replicating the results of Matsumoto, et al. [13, 15] in achieving Coulomb blockade in double barrier Ti/$TiO_2$ junctions. Most likely, this is due to the difficulties in controlling the AFM nanooxidation process and creating smooth thin layers of metal for the procedure. This research effort has fabricated Ti/$TiO_2$ devices using this technique and has reported the results [60]. Also, this effort has shown for the first time that Ni can be oxidized via scanning probe lithography techniques. Although difficult to control, patterns were fabricated in the Ni and a device was made and Coulomb conductance oscillations achieved.

The process of adding a strong magnetic field has been shown to be an effective method to obtain clear Coulomb oscillations. This process should lead others to continue studying planar metal-oxide coulomb blockade devices and to study planar ferromagnetic oxide tunnel devices as well. Promising materials for these future studies include Co and Fe. Devices using these materials have been fabricated up to the point of requiring nanolithography as part of this research effort. In addition, a sample has been fabricated with Ti deposited on sapphire, which has been reported to improve surface morphology for nanooxidation of tunnel devices [14], this too is ready for nanolithography. The single barrier Ti and Ni devices fabricated to determine nanolithography parameters are also readily available to be packaged for characterization. Future efforts could readily expand on the presented research by using the above-cited samples or ones similar.

# Figures

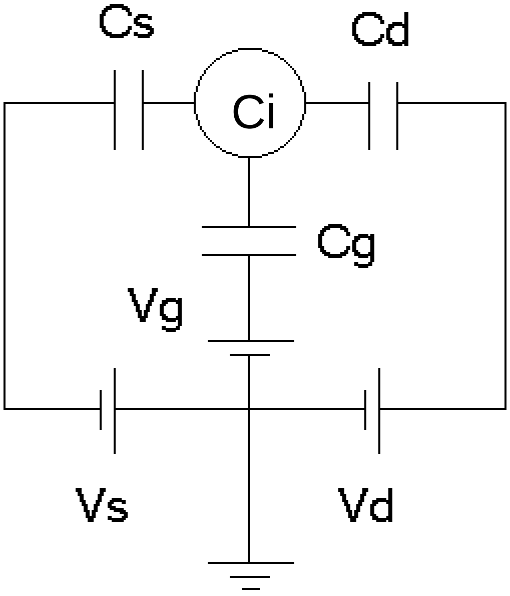

**Fig 1. Schematic of a Single Electron Transistor with source (s), drain (d), gate (g), and island (i).**

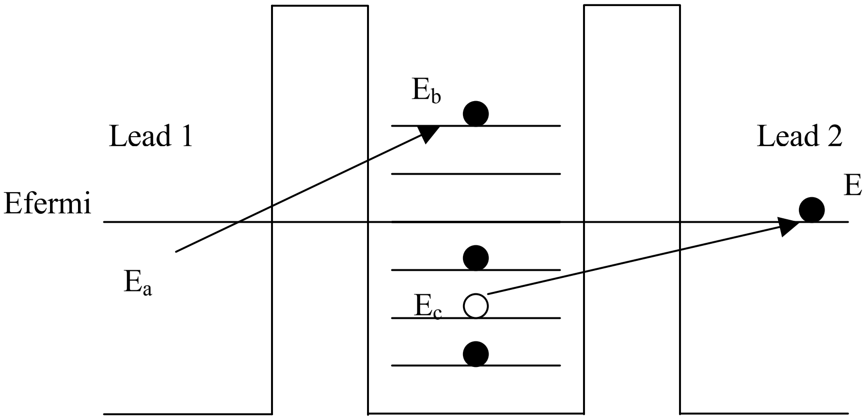

**Fig. 2. Diagram of inelastic cotunneling. One electron tunnels from the left electrode, an electron from below the fermi level in the island creates a hole and tunnels to the right electrode, thus creating an electron-hole excitation.**

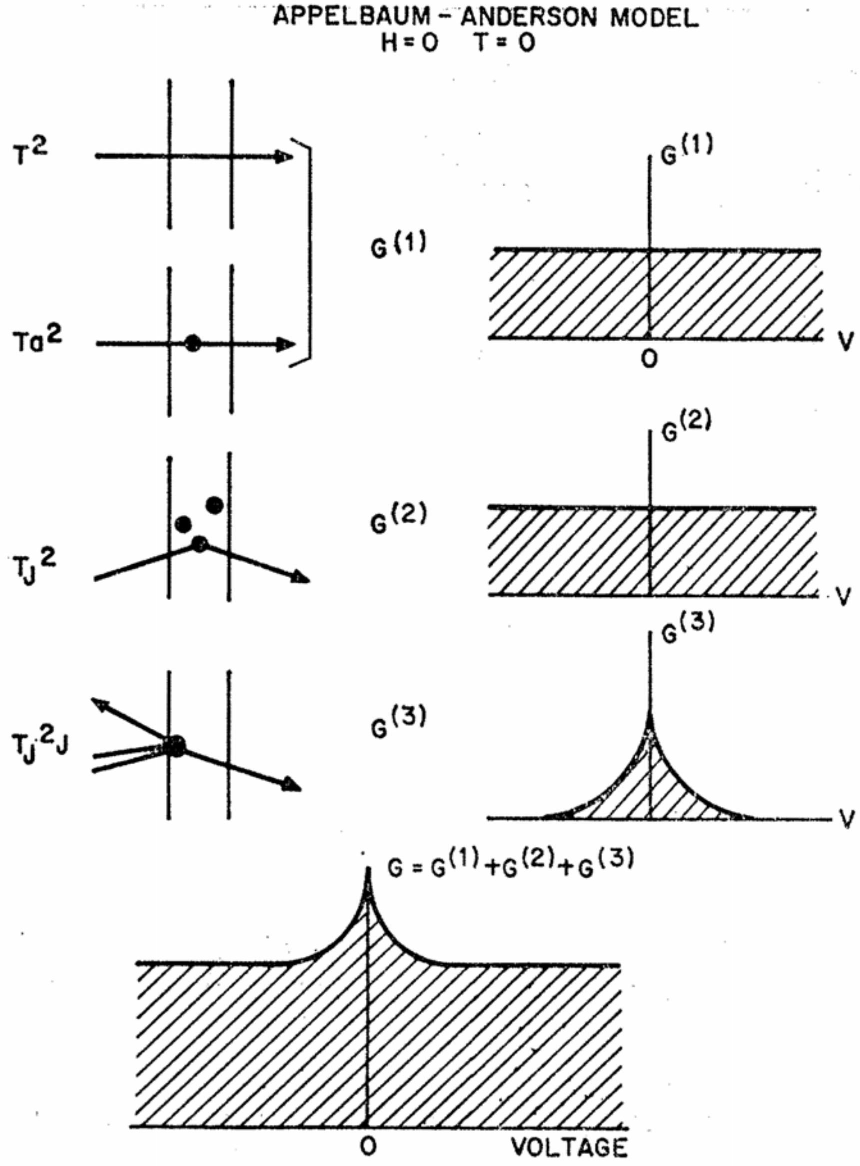

**Fig. 3. Diagram of Appelbaum-Anderson Theory after Shen and Rowell [31]. Three conductance contributions to tunneling with localized *d* state near barrier: (1) No interaction (2) Spin-flip process with magnetic field dependence that can reduce conductance (3) Kondo Tunneling with temperature and field dependence that gives rise to zero-bias peak.**

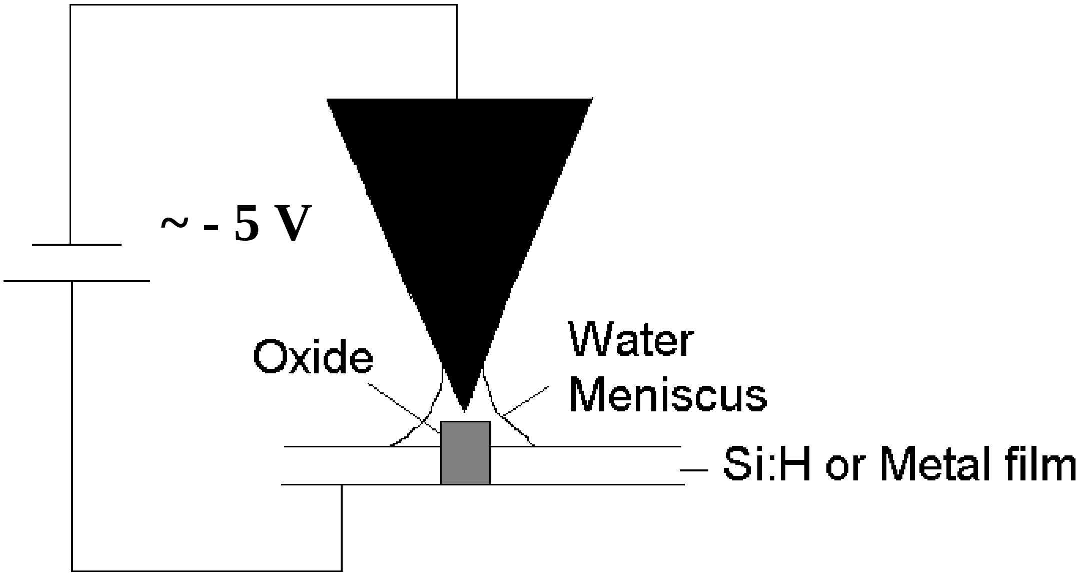

**Fig. 4. The applied negative bias to the AFM tip disassociates the water present from ambient humidity, creating narrow oxide lines underneath the tip.**

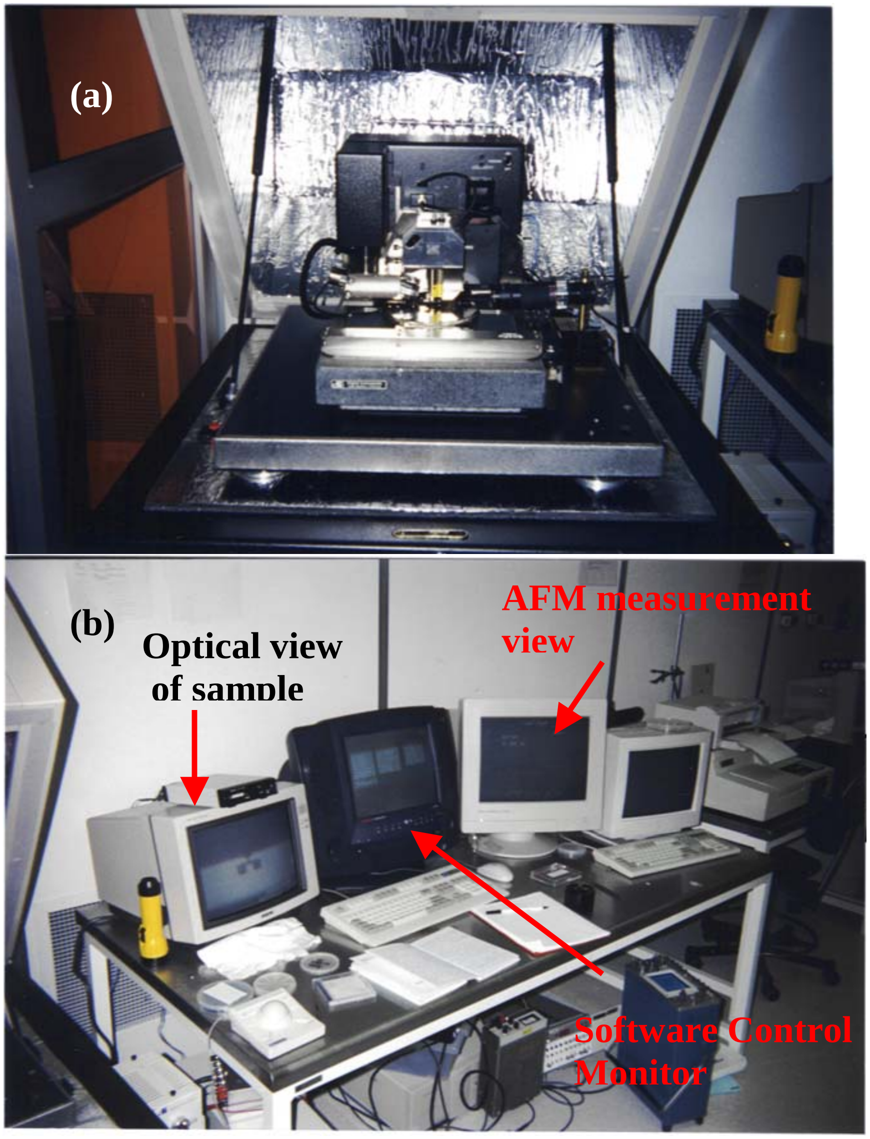

**Fig. 5. Digital Instruments atomic force microscope where (a) the probe head and sample holder are contained on a vibration isolated stage and (b) monitors provide an optical view of the sample, view of computer software control, and the AFM measurement view.**

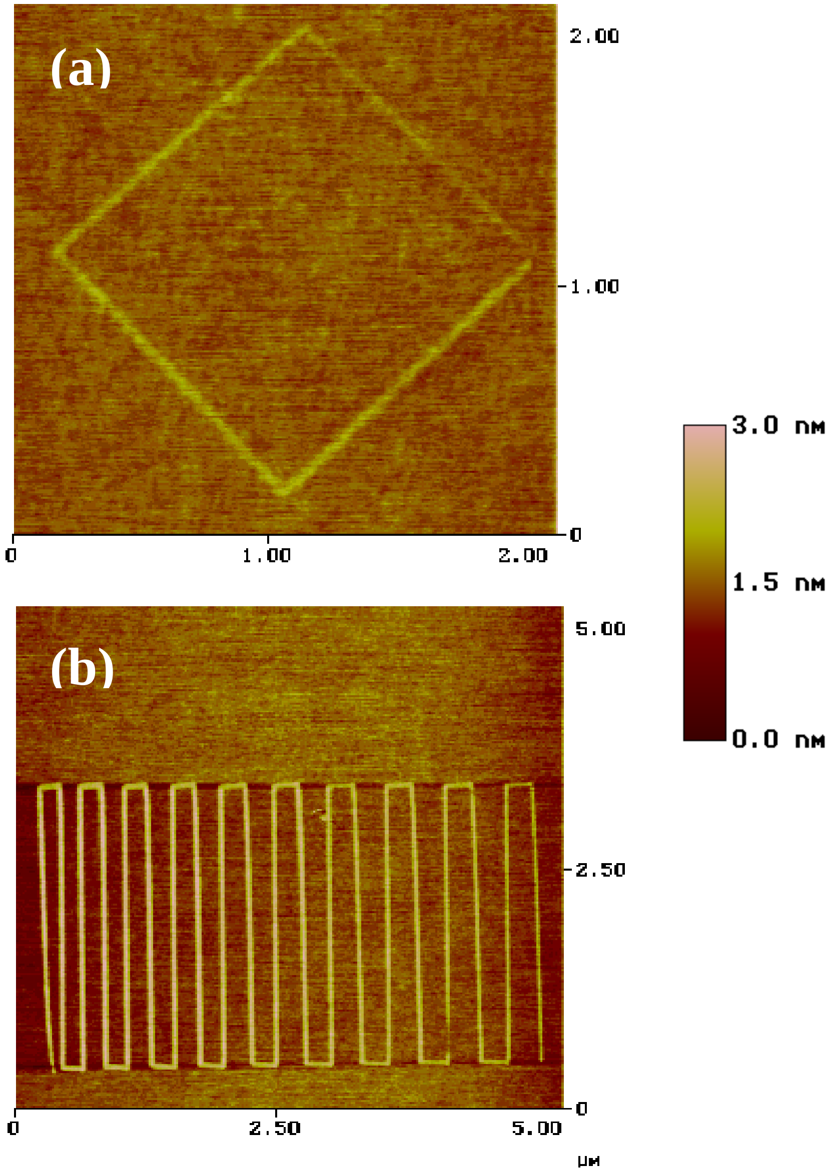

**Fig. 6. AFM nanolithography of Si at (a) - 8 V, 0.5 µm/s writing 80 nm lines and at (b) - 6 V, 0.5 – 10 µm/s writing 80 to 50 nm lines.**

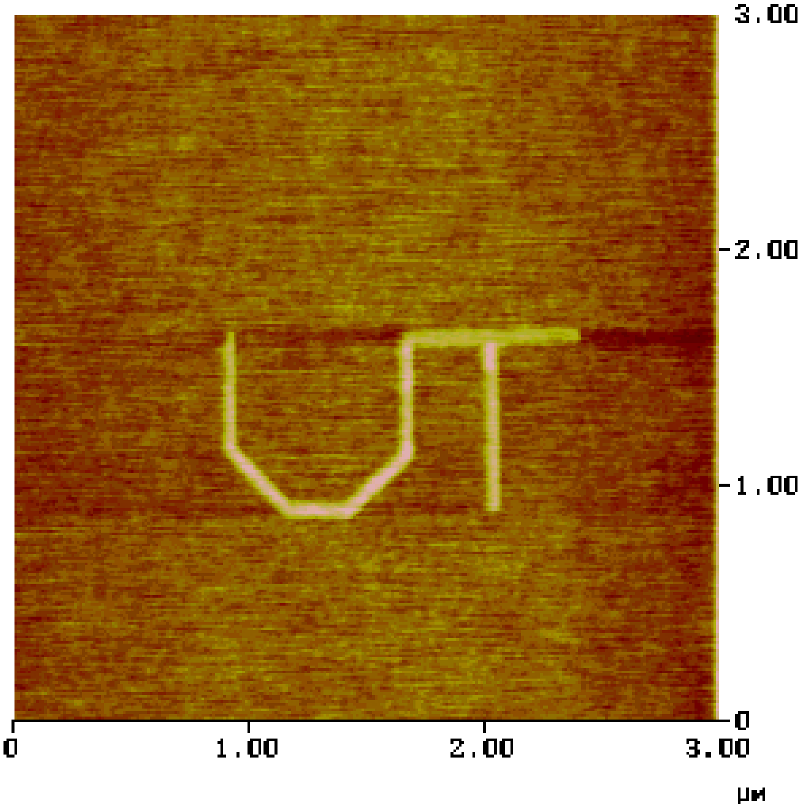

**Fig. 7. 80 nm line width UT drawn on Si with AFM nanooxidation process.**

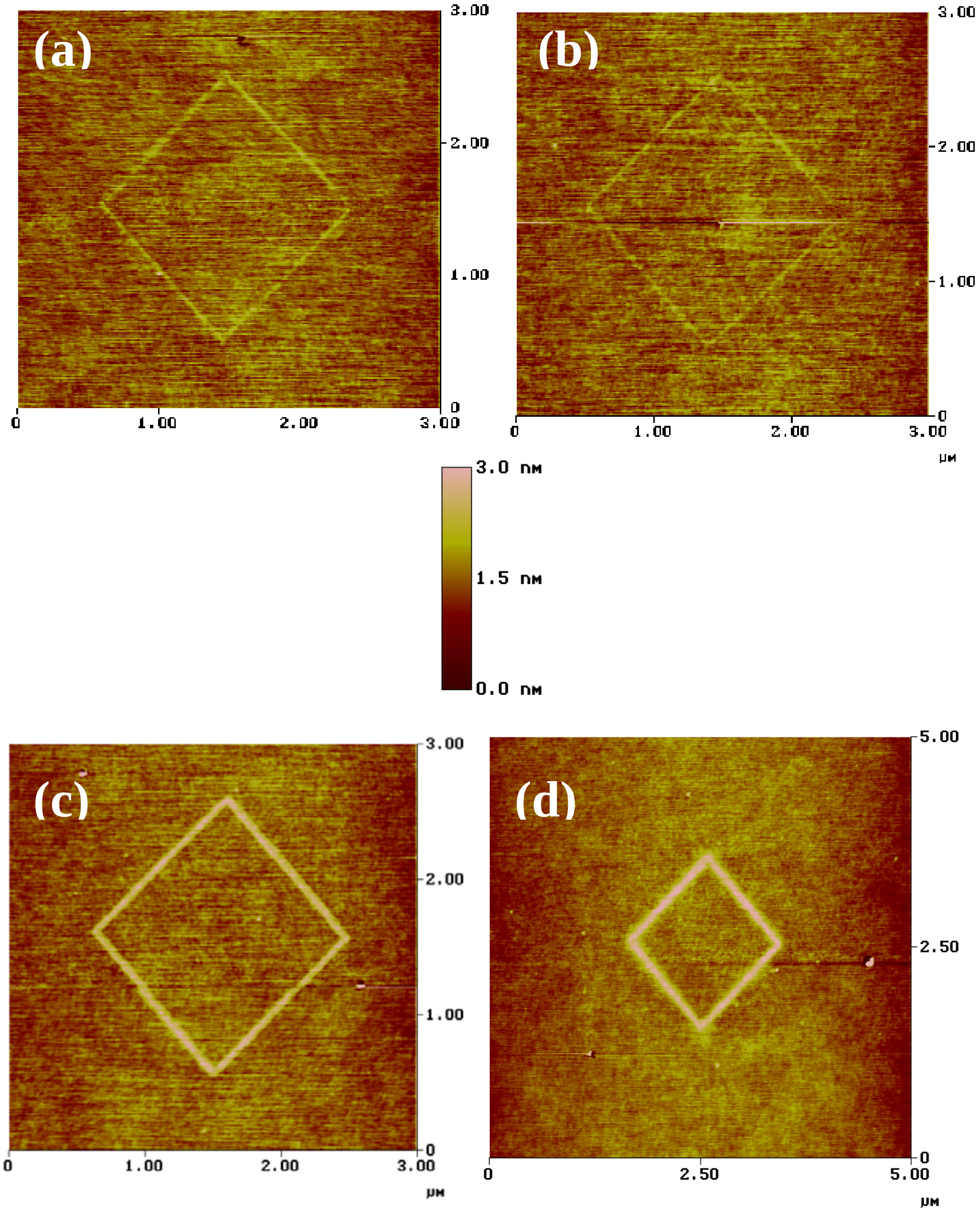

**Fig. 8. $TiO_2$ lines drawn with AFM nanolithography at (a) - 9 V at 0.05 µm/s 25 nm line width (b) - 10 V at 0.1 µm/s 25 nm line width (c) - 12 V at 0.2 µm/s 50 nm line width (d) - 12 V at 0.05 µm/s 190 nm line width.**

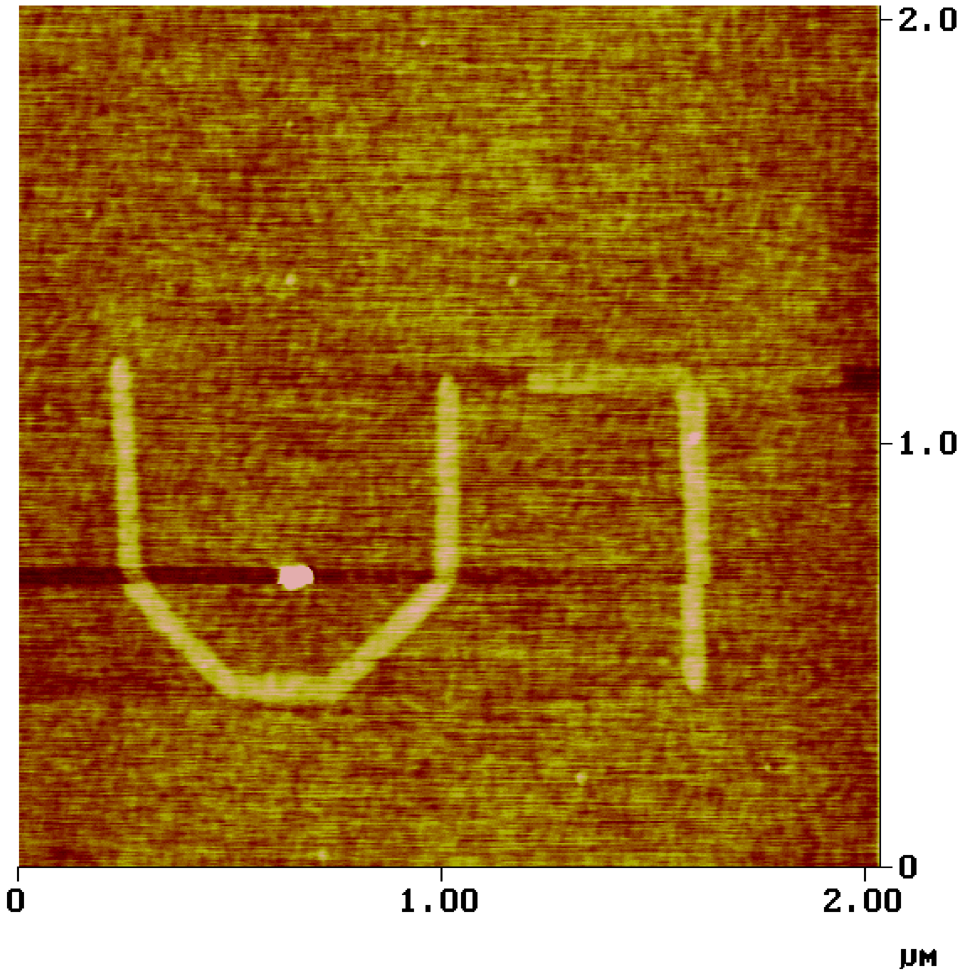

**Fig. 9. UT drawn in $TiO_2$ at - 12 V 0.5 μm/s 90 nm line width.**

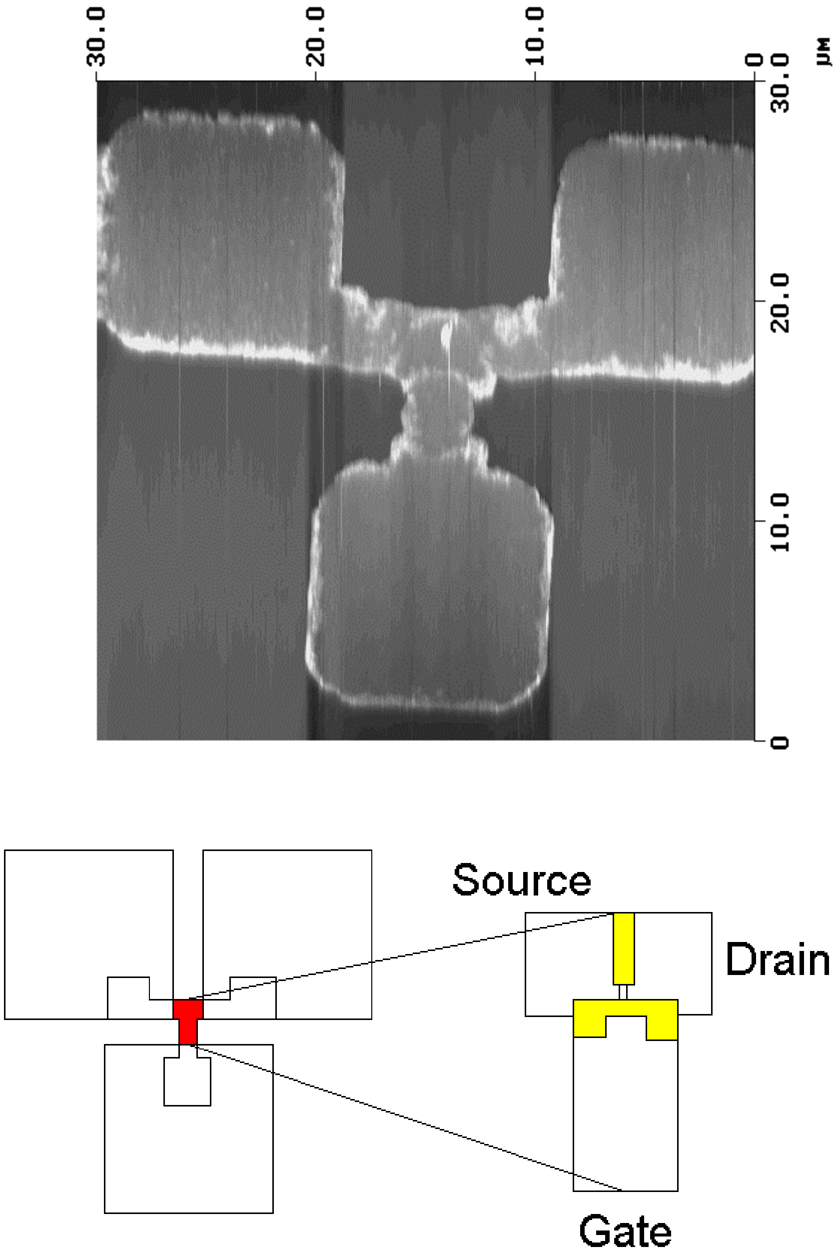

**Fig. 10. Schematic and AFM image of device layer of metallization that form "T" junction with 2 µm metal line width.**

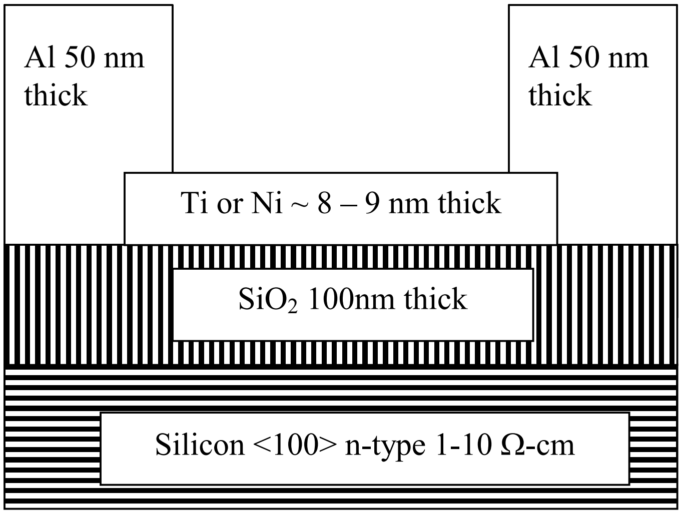

**Fig. 11. Schematic of device structure before AFM nanolithography.**

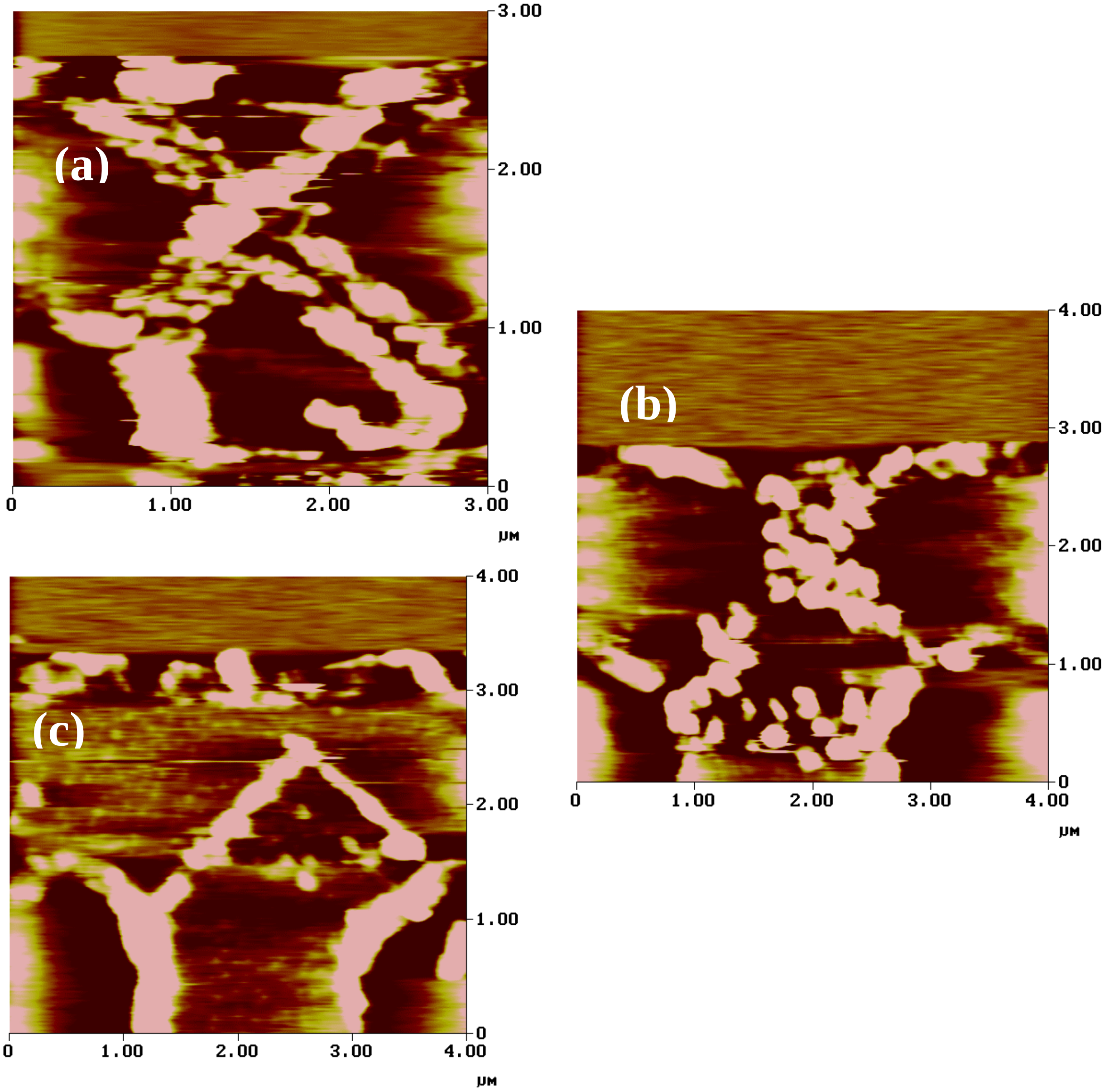

**Fig. 12. NiO patterns written with (a) - 7 V, 0.3 µm/s (b) - 6 V, 1.0 µm/s (c) - 4 V, 0.5 µm/s.**

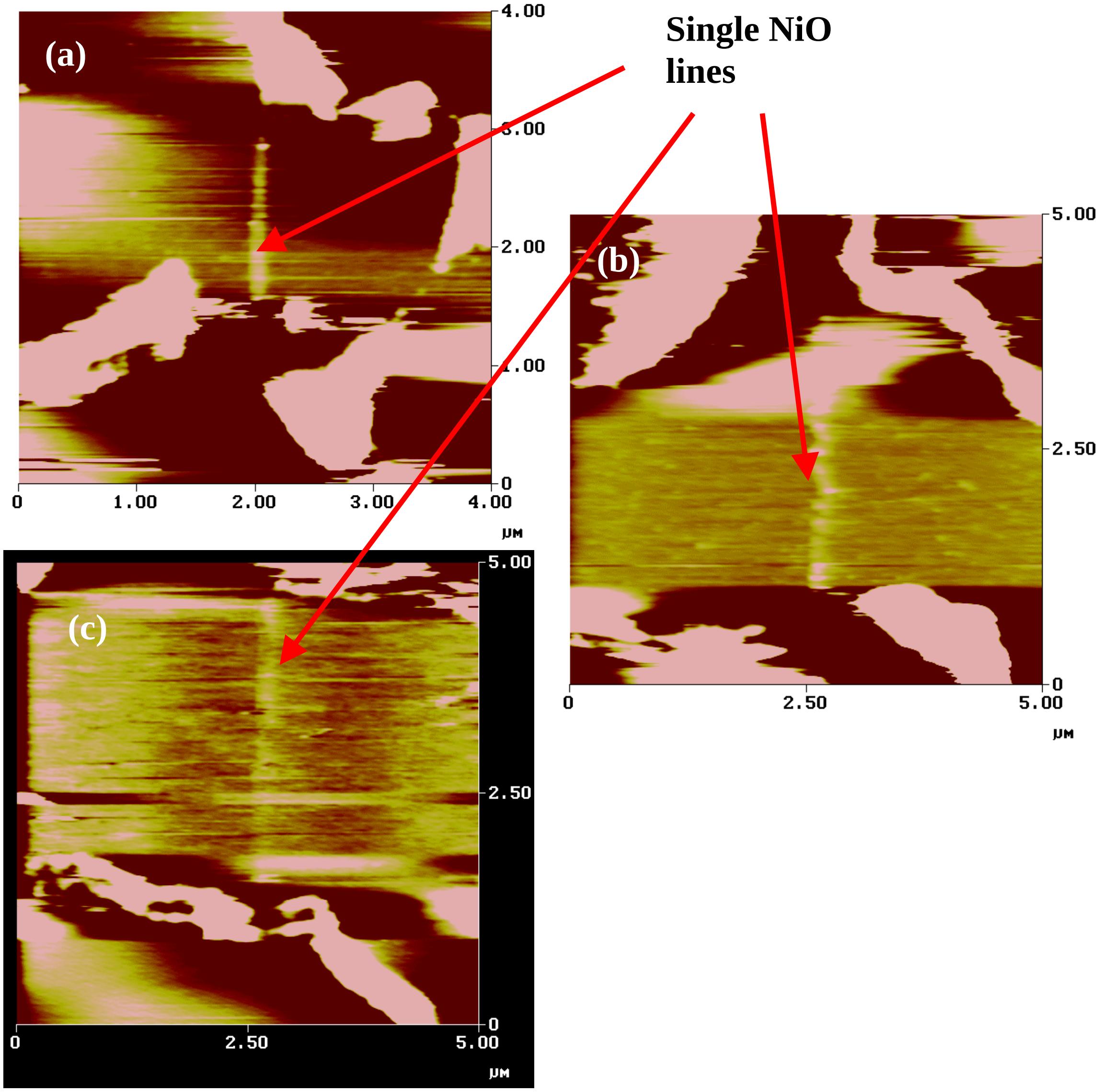

Single NiO lines

Fig. 13. NiO lines drawn on 154 Å of Ni at - 10 V, 10 Hz (a) 0.04 µm/s, 85 nm line width (b) 0.04 µm/s, 100 nm line width, (c) 0.02 µm/s 150 nm line width.

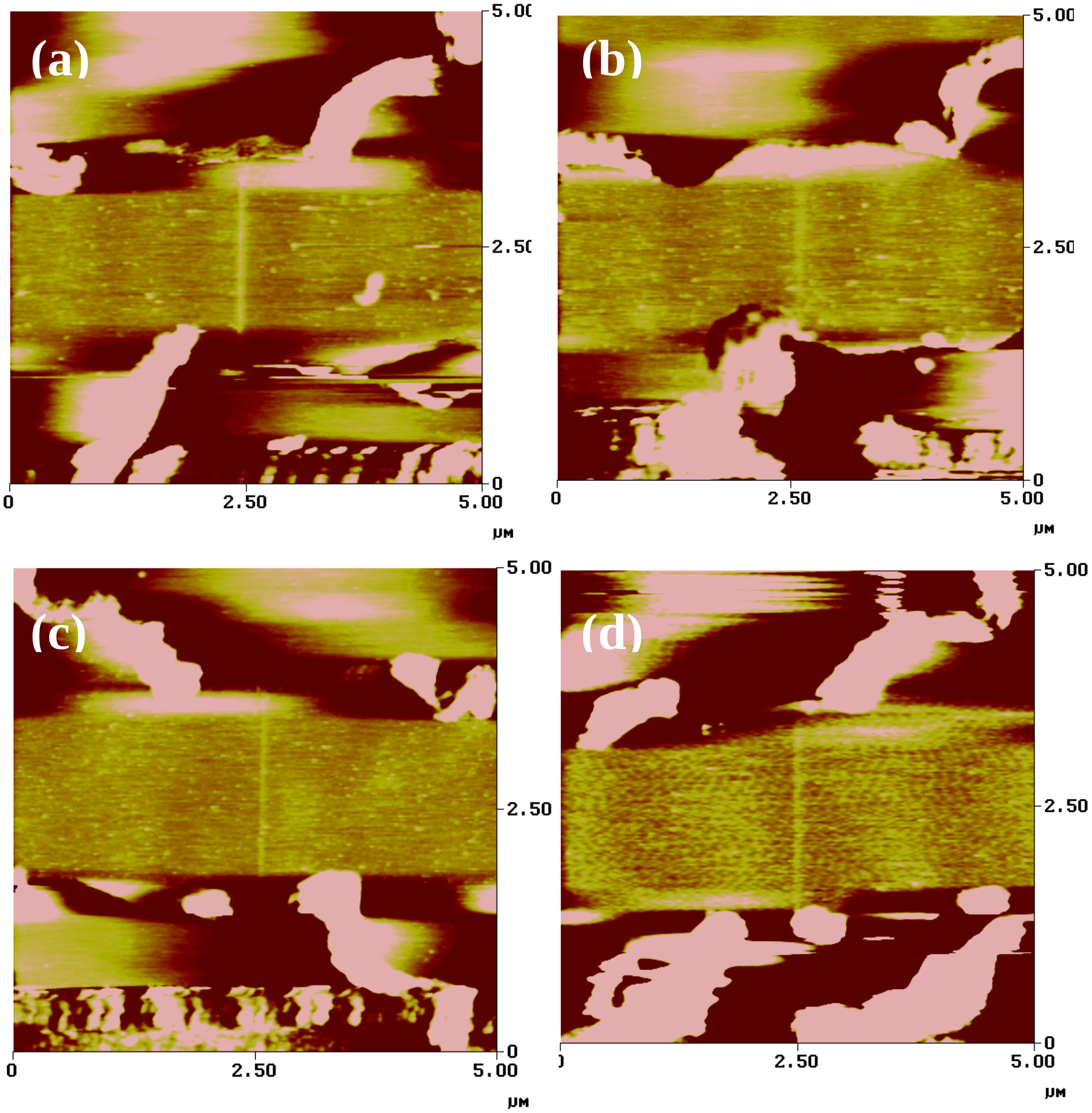

**Fig. 14.** TiO$_2$ single lines drawn on 220 Å of Ti at 10 Hz, 0.1 µm/s at (a) - 7 V, 150 nm (b) - 7 V, 150 nm (c) - 8 V, 80 nm (d) - 9 V, 90 nm.

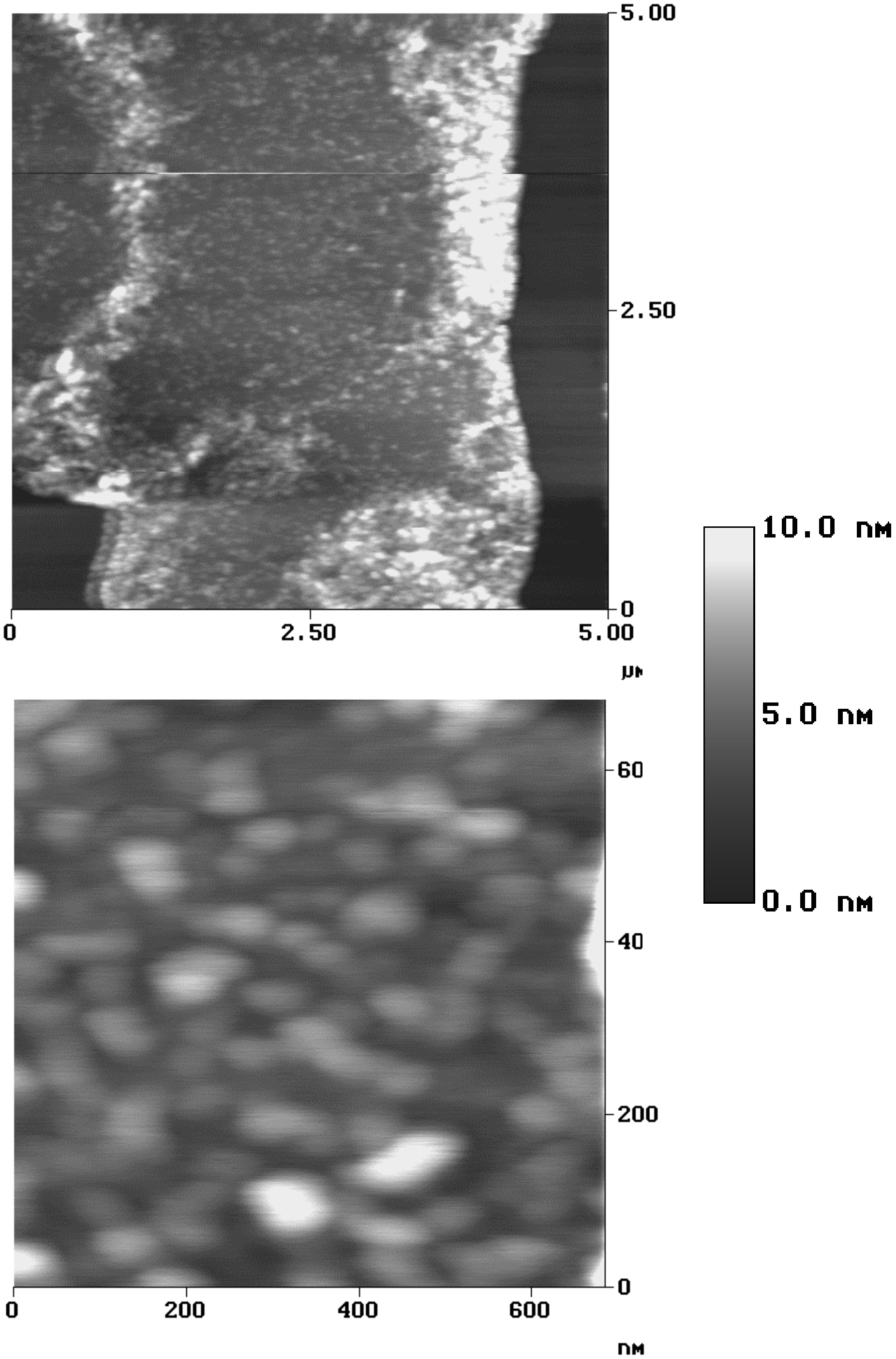

Fig. 15. Ti material deposited showing granularity of surface with grains from 2 – 50 nm in size.

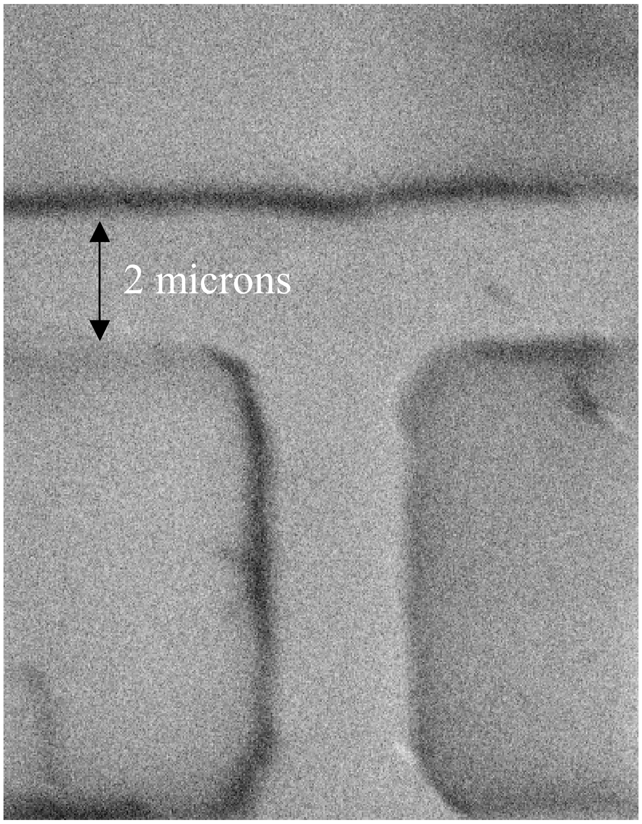

**Fig. 16. Scanning electron microscope image of device layer formed using standard lithography.**

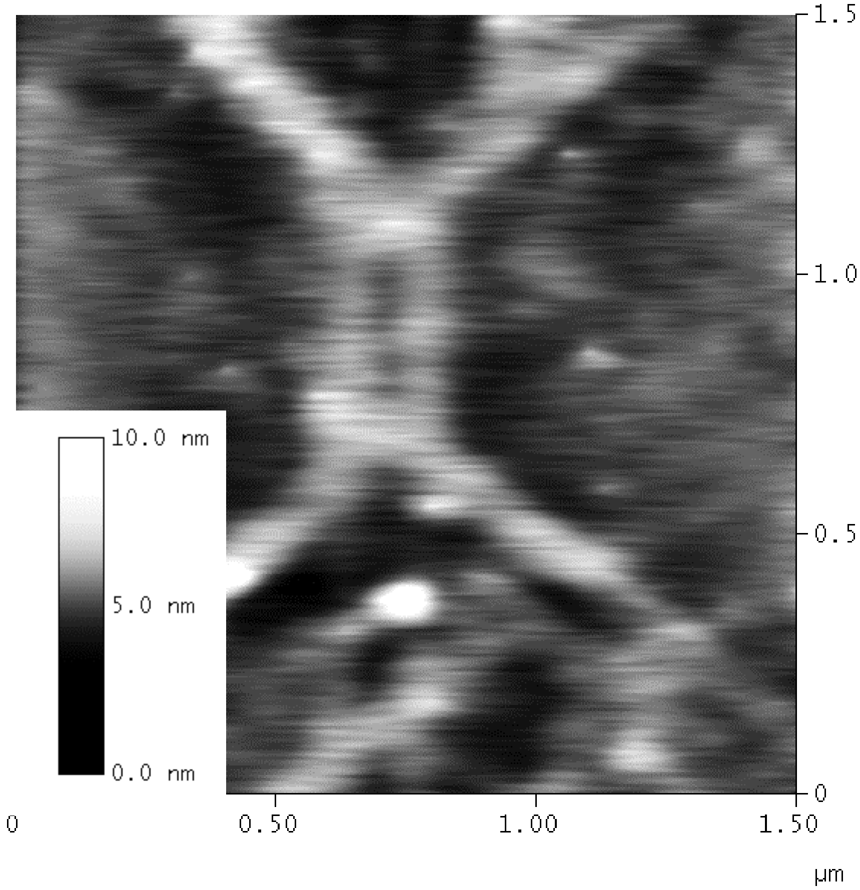

**Fig. 17. The $TiO_2$ double-barrier tunnel junction in Ti device 1 formed using AFM lithography with intentionally unoxidized internal region.**

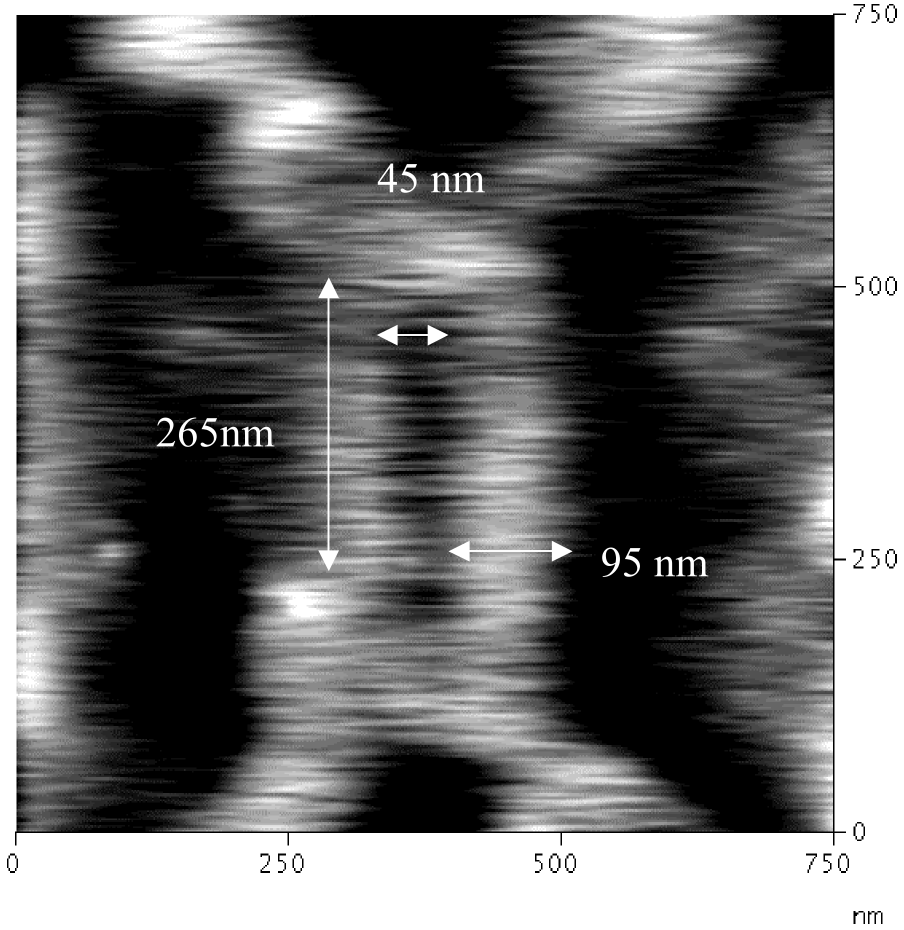

**Fig. 18. Closer AFM image of Ti device 1. The barrier length is 265 nm, the oxide barrier widths are 75 and 95 nm and the unoxidized metallic island width is 45 nm.**

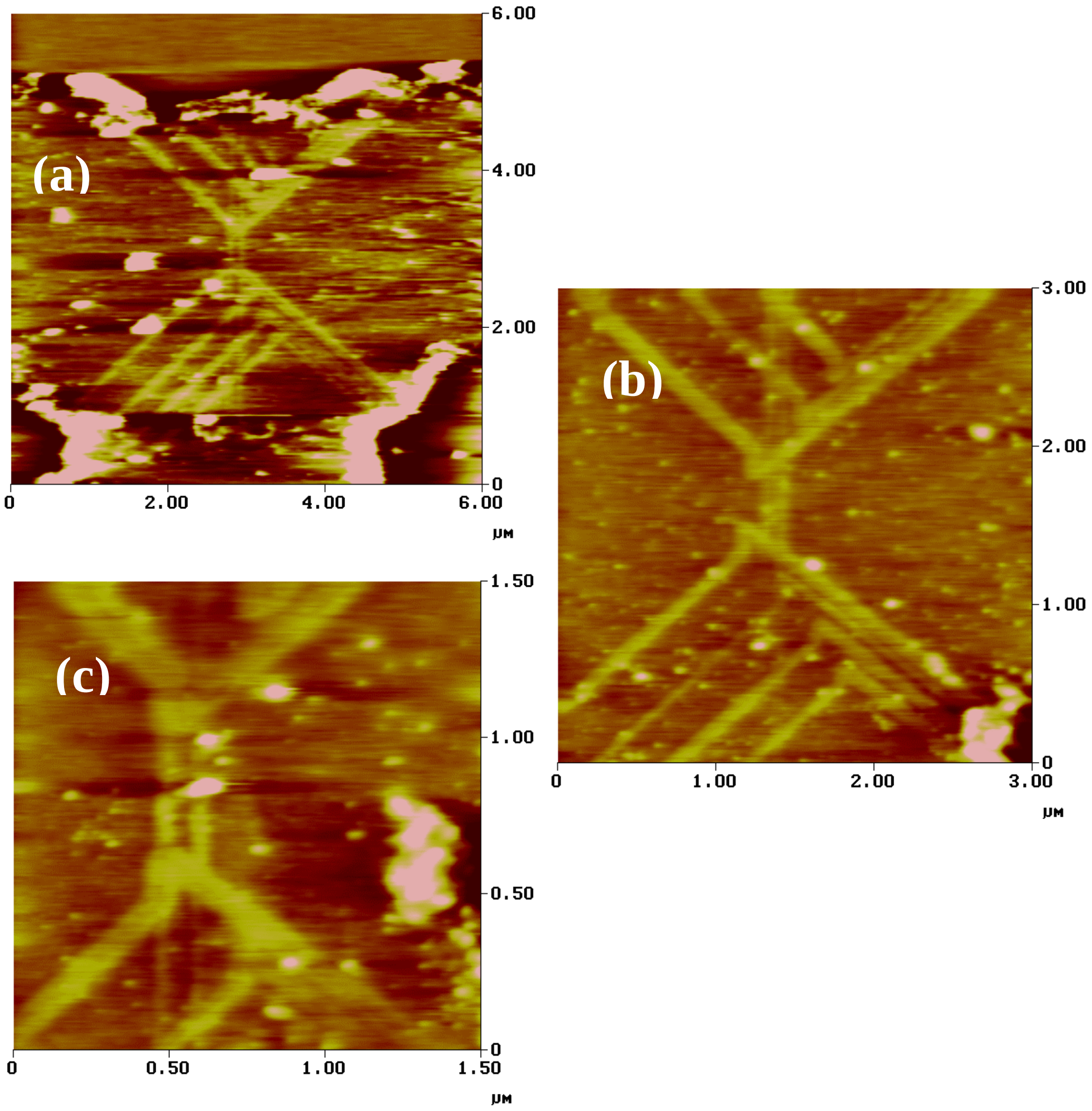

**Fig. 19. Three devices fabricated with $TiO_2$ barriers. Tunnel barriers made at (a) Ti device 2, - 8 V at 0.7 µm/s, (b) Ti device 3, - 8 V at 0.5 µm/s, (c) Ti device 4, - 8 V at 1.5 µm/s.**

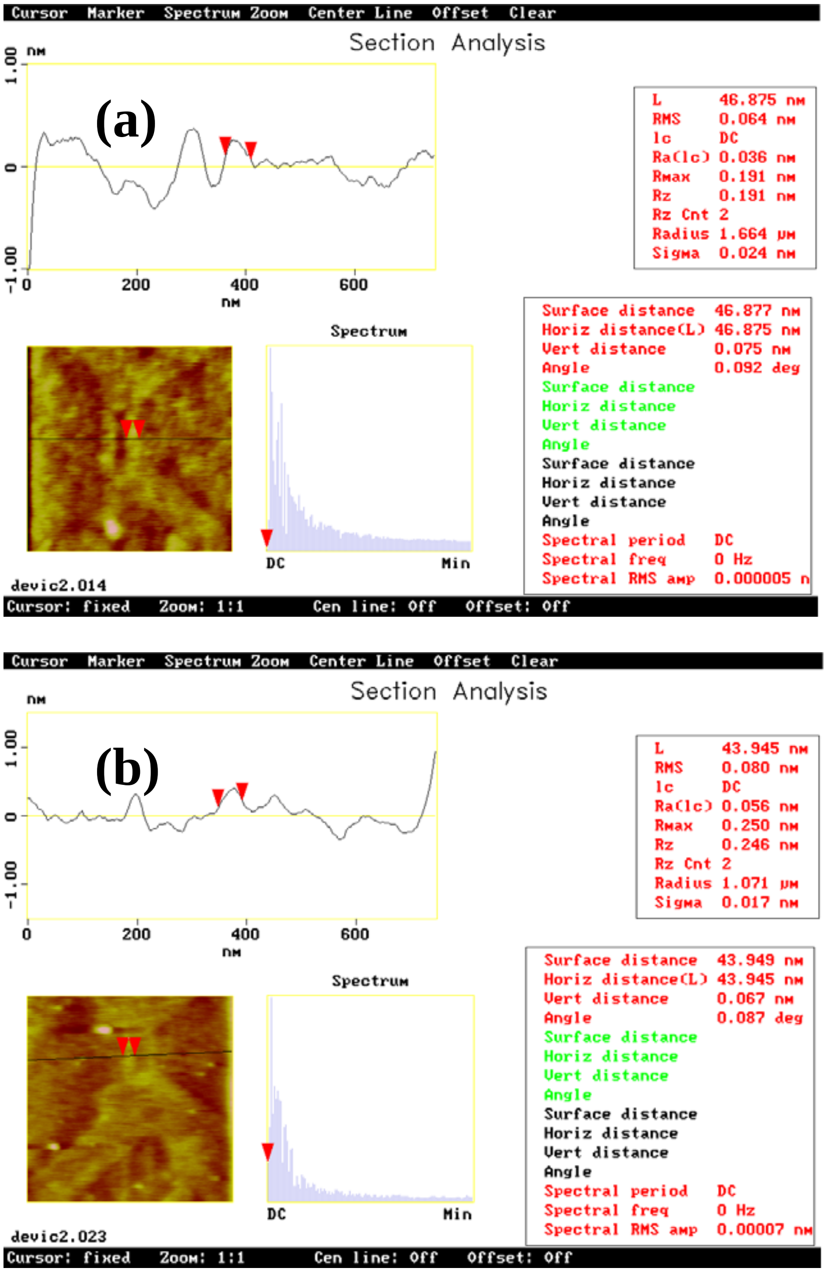

(a)

L 46.875 nm
RMS 0.064 nm
lc DC
Ra(lc) 0.036 nm
Rmax 0.191 nm
Rz 0.191 nm
Rz Cnt 2
Radius 1.664 µm
Sigma 0.024 nm

Surface distance 46.877 nm
Horiz distance(L) 46.875 nm
Vert distance 0.075 nm
Angle 0.092 deg
Surface distance
Horiz distance
Vert distance
Angle
Surface distance
Horiz distance
Vert distance
Angle
Spectral period DC
Spectral freq 0 Hz
Spectral RMS amp 0.000005 n

devic2.014

(b)

L 43.945 nm
RMS 0.080 nm
lc DC
Ra(lc) 0.056 nm
Rmax 0.250 nm
Rz 0.246 nm
Rz Cnt 2
Radius 1.071 µm
Sigma 0.017 nm

Surface distance 43.949 nm
Horiz distance(L) 43.945 nm
Vert distance 0.067 nm
Angle 0.087 deg
Surface distance
Horiz distance
Vert distance
Angle
Surface distance
Horiz distance
Vert distance
Angle
Spectral period DC
Spectral freq 0 Hz
Spectral RMS amp 0.00007 nm

devic2.023

**Fig. 20. AFM profile measurement of (a) Ti device 2 (47 nm line width) and (b) Ti device 4 (44 nm line width).**

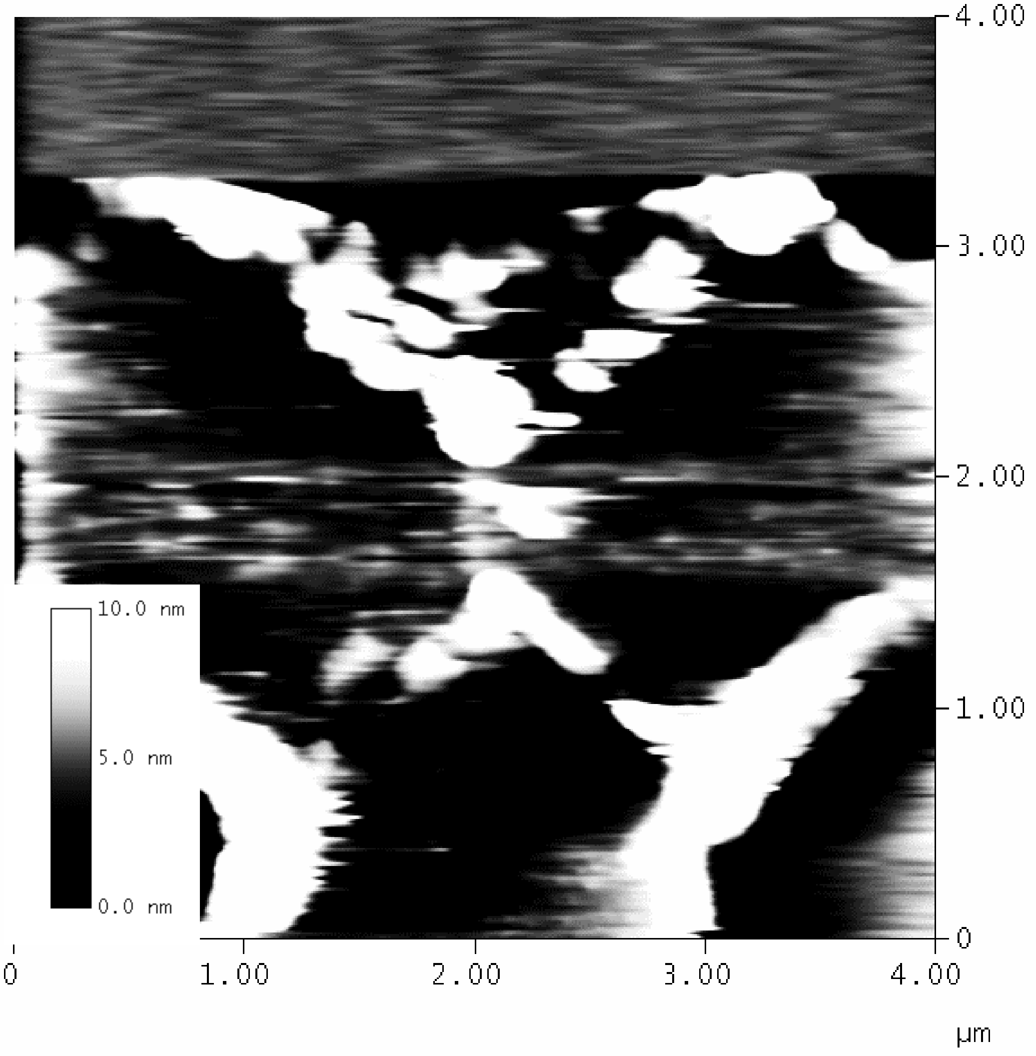

**Fig. 21. The NiO-barrier tunnel junction device formed using AFM lithography with under oxidized barrier. The central part of the barrier is 345 nm thick.**

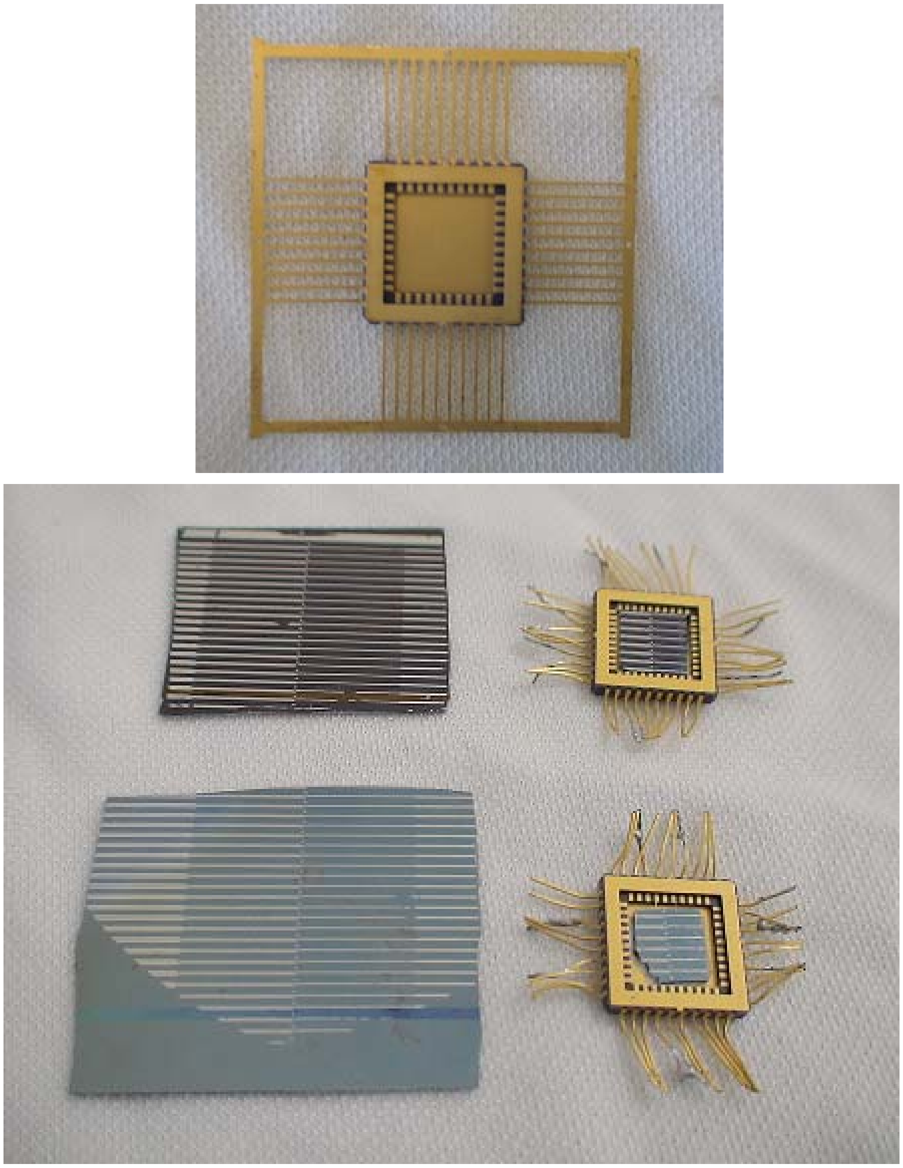

**Fig. 22. Fabricated samples before and after packaging in the square gold plated Kyocera flat-packs.**

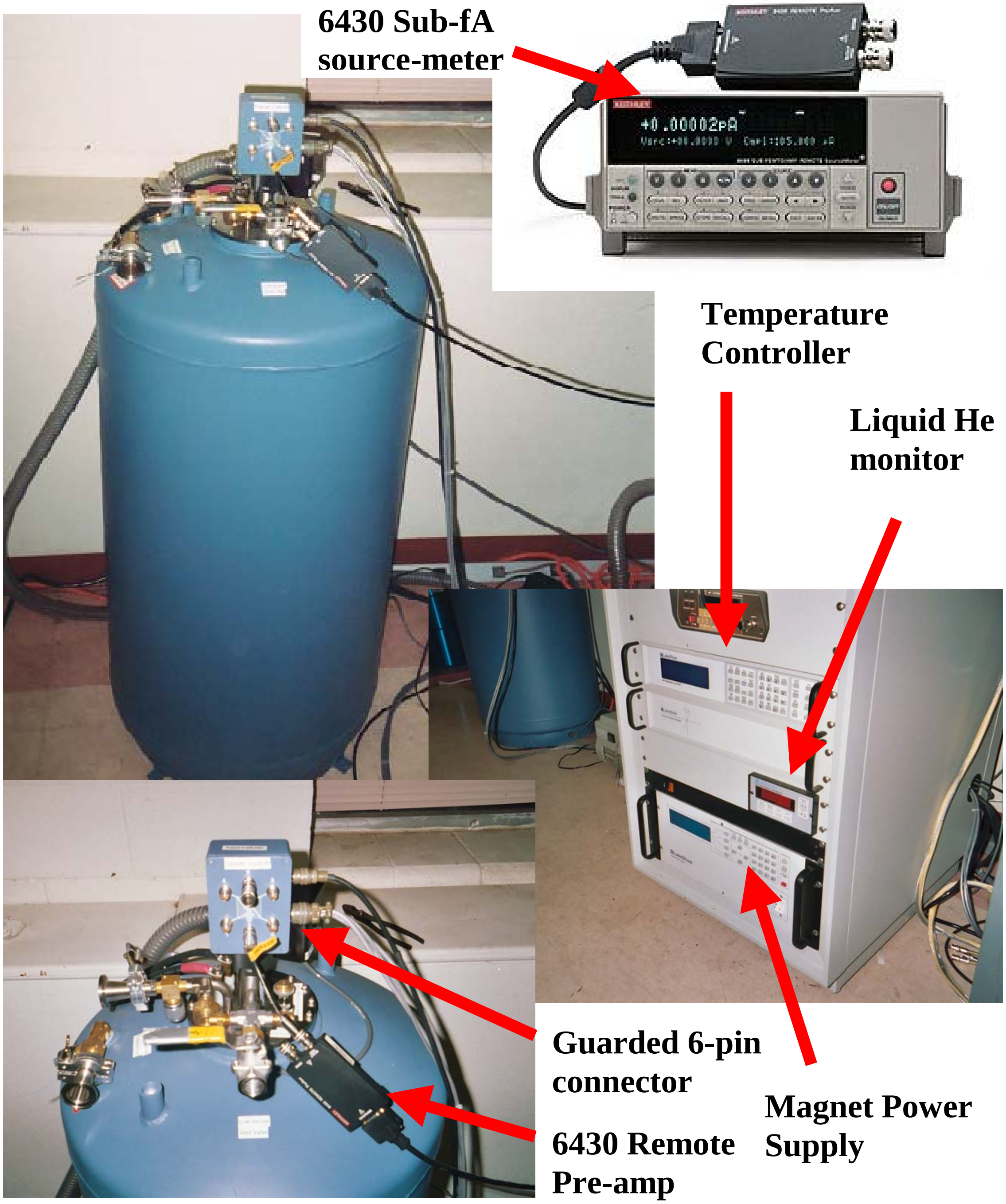

**Fig. 23. LakeShore 9500 Hall Effect Measurement System with 9T magnet, temperature control, Keithley 6430 with remote pre-amp, and guarded 6 pin-out connector to sample rod.**

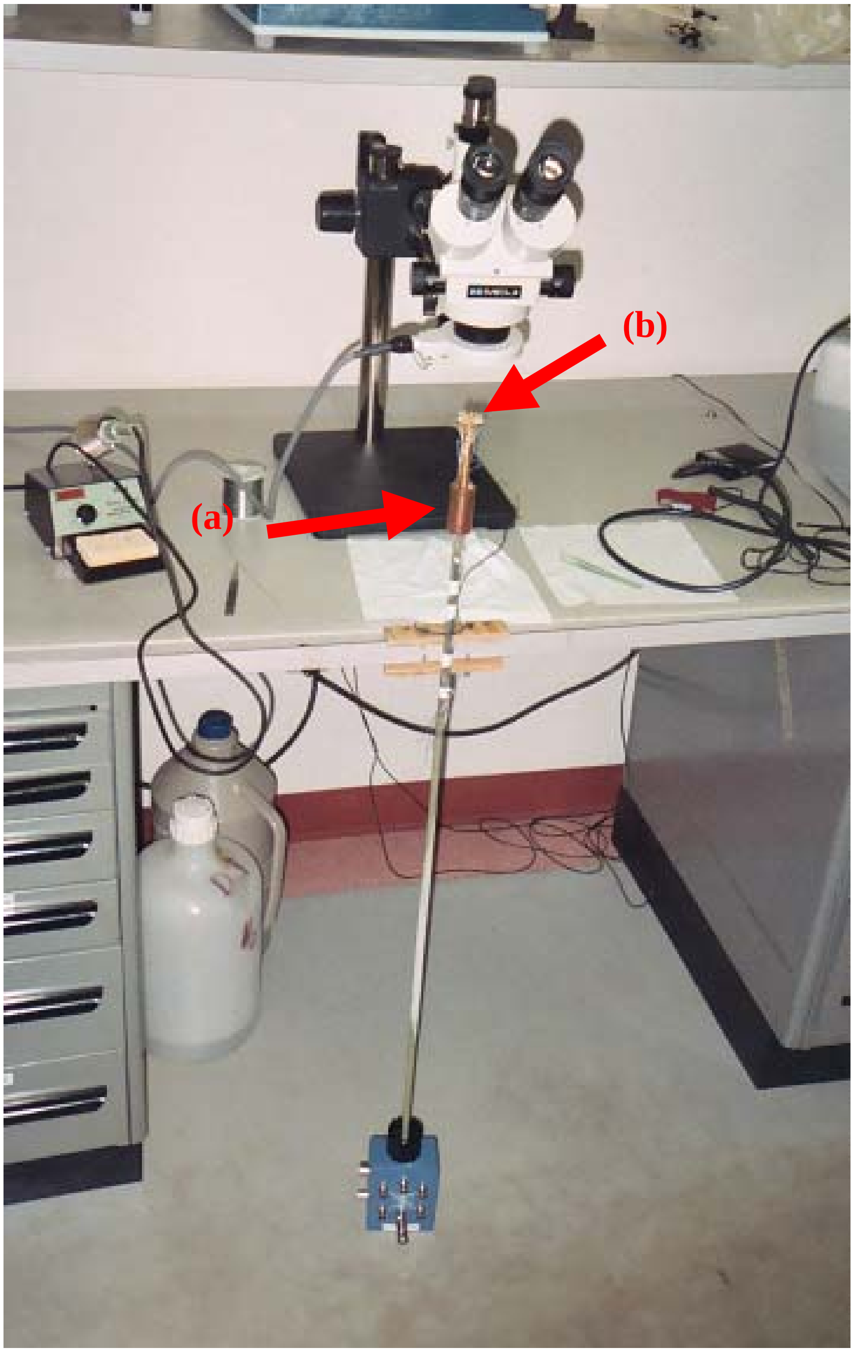

**Fig. 24. Sample holder for packaged samples to be mounted into cryostat. Two thermocouples located at (a) the large copper block heater and (b) the small sample heater inside gold plated base to which the sample is mounted.**

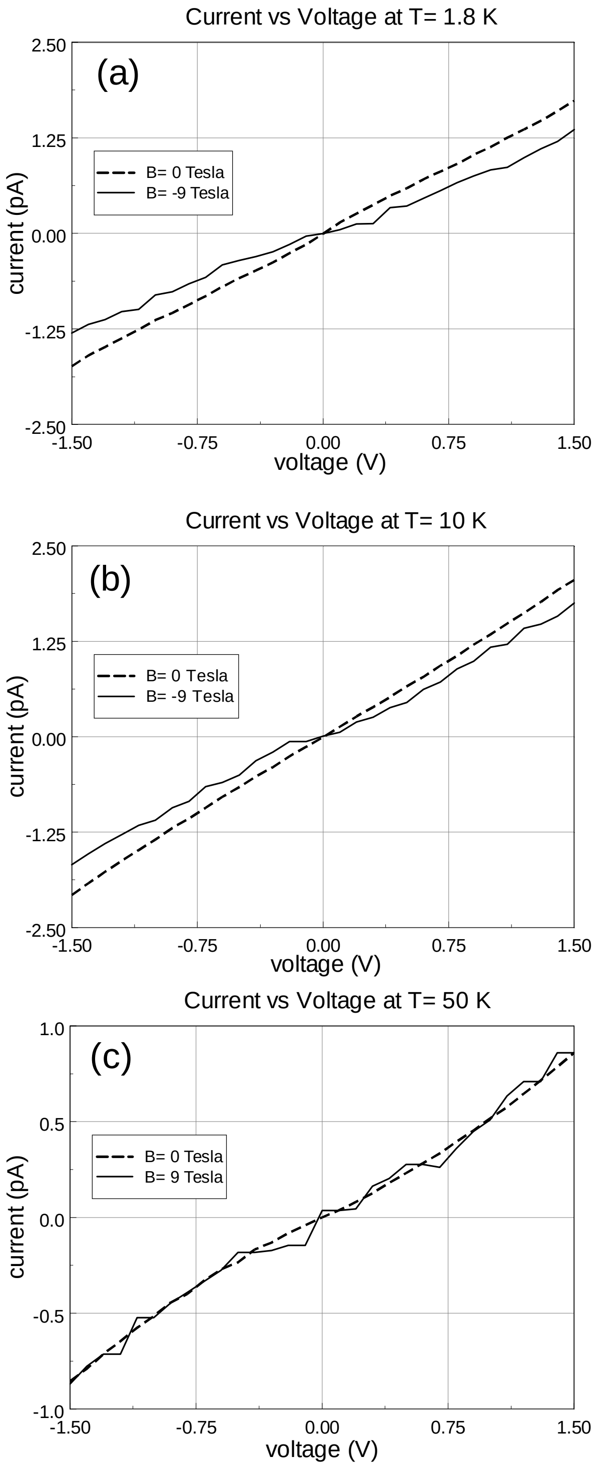

**Fig. 25. I-V plots of Ti device 1 at (a) 1.8 K, (b) 10 K, and (c) 50 K with and without 9T field. Dashed line is for no applied magnetic field.**

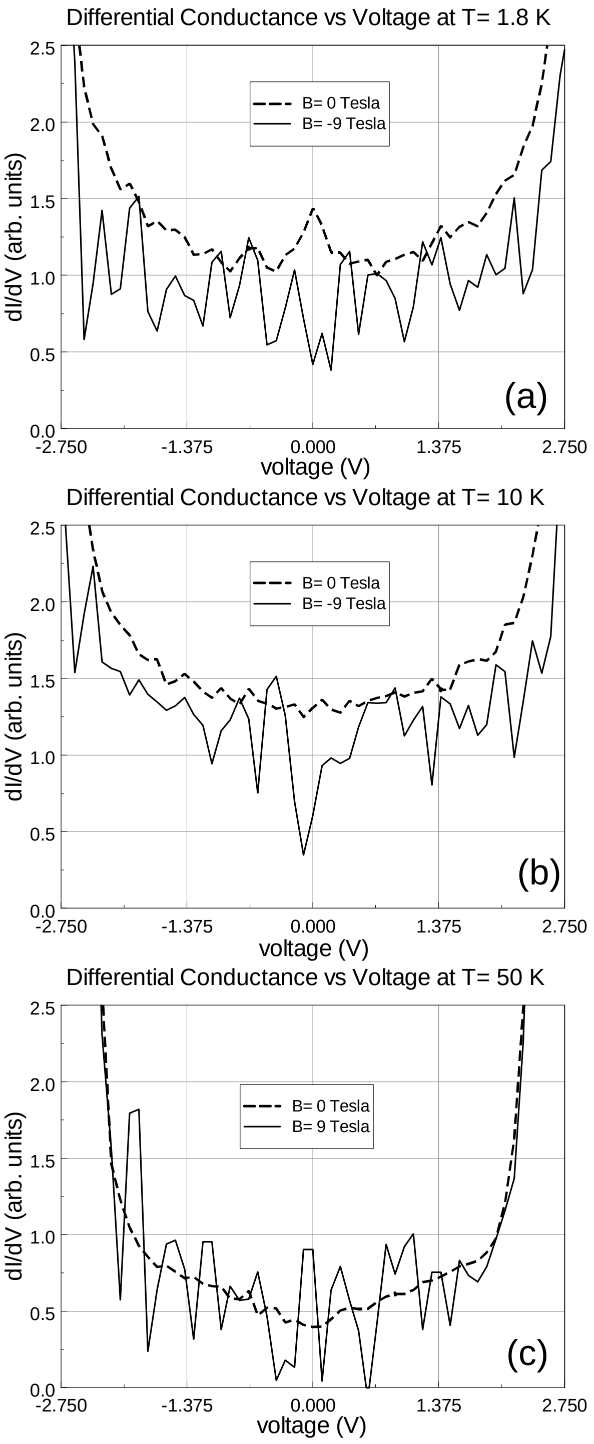

**Fig. 26. Differential conductance of Ti device 1 with and without applied 9T magnetic field at (a)1.8 K, (b) 10 K and (c) 50 K. The dashed line is for no applied field.**

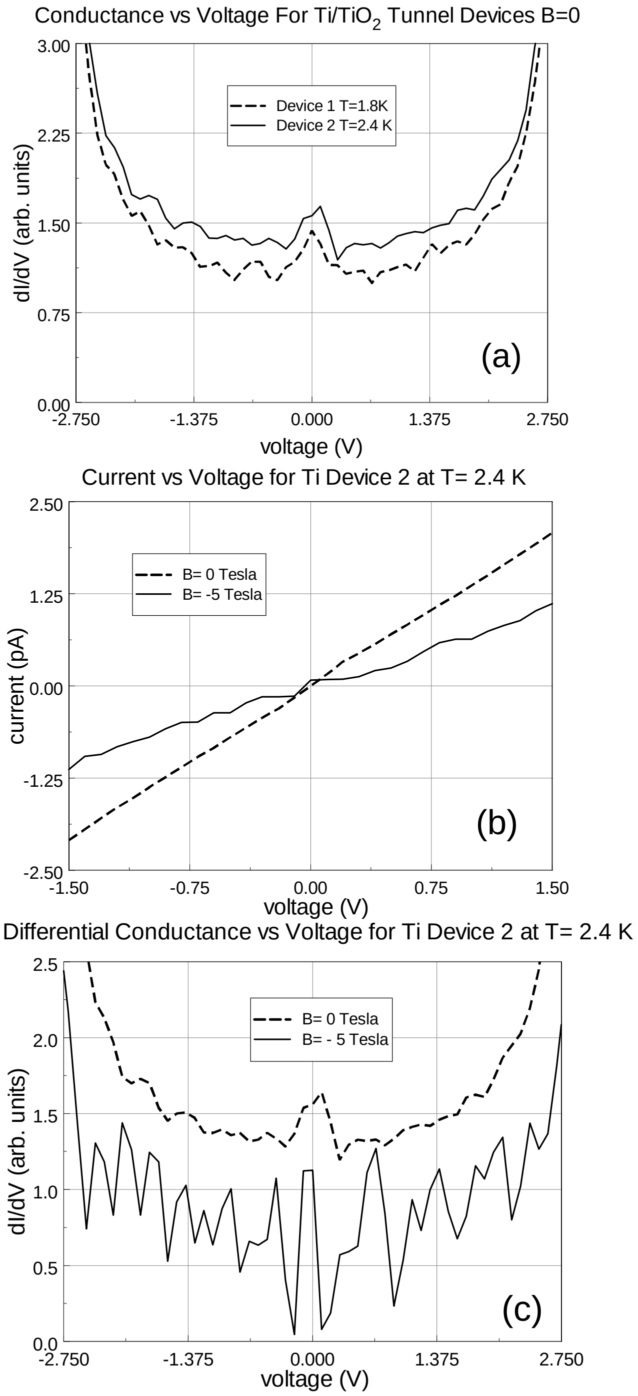

**Fig. 27. (a) Conductance versus voltage for Ti devices 1 & 2 showing oscillations and zero-bias conductance peak with no magnetic field (b) I-V plot of Ti device 2 with and without 5 T magnetic field (c) conductance plot of Ti device 2 with and without 5 T field.**

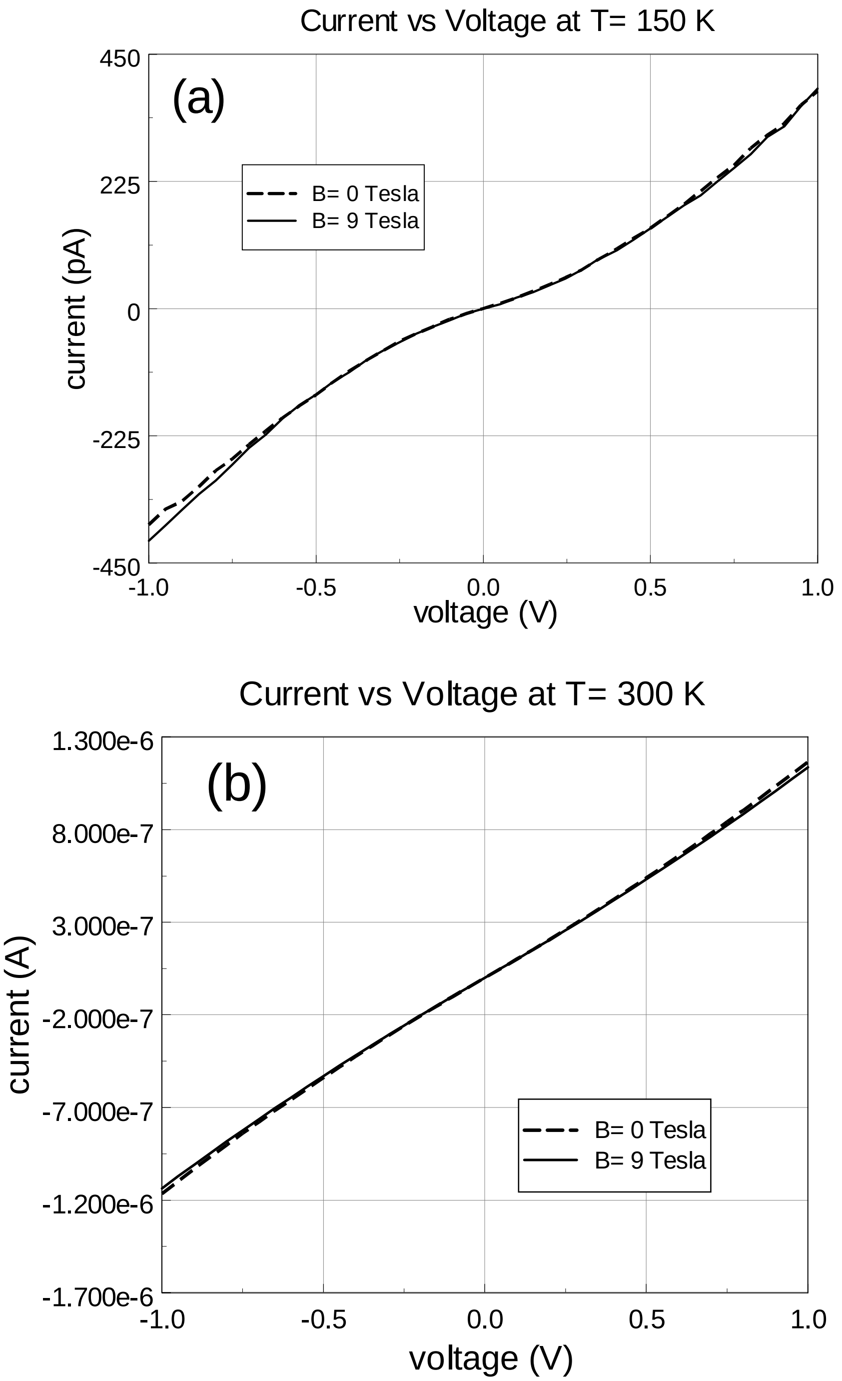

**Fig. 28. I-V curves for Ti device 1 at (a) 150 K and (b) 300 K showing that although tunneling behavior is still present, Coulomb blockade is no longer observable, even with a magnetic field.**

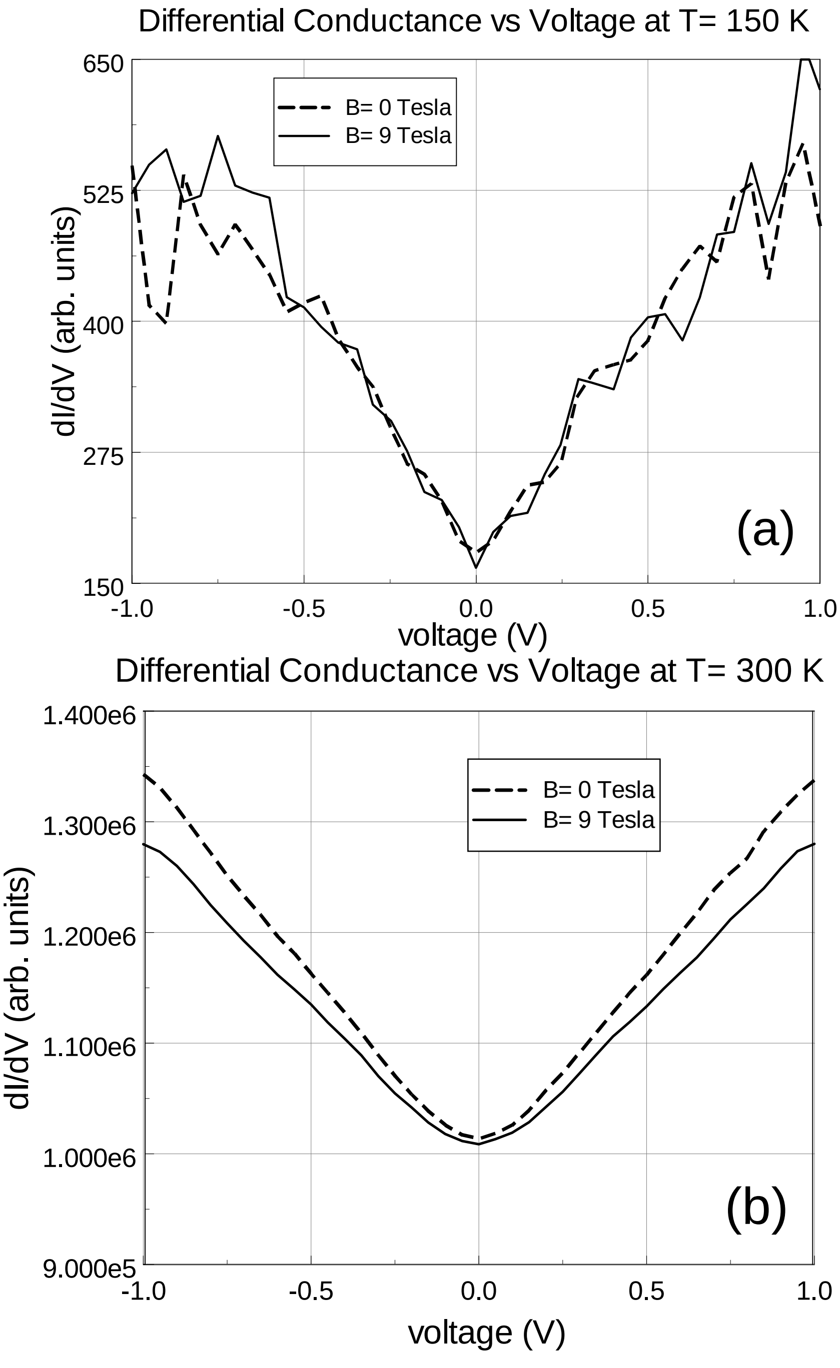
Differential Conductance vs Voltage at T= 150 K

Differential Conductance vs Voltage at T= 300 K

**Fig. 29. dI/dV for Ti device 1 at (a) 150 K and (b) 300 K illustrating the Coulomb blockade oscillations becoming less significant to current transport.**

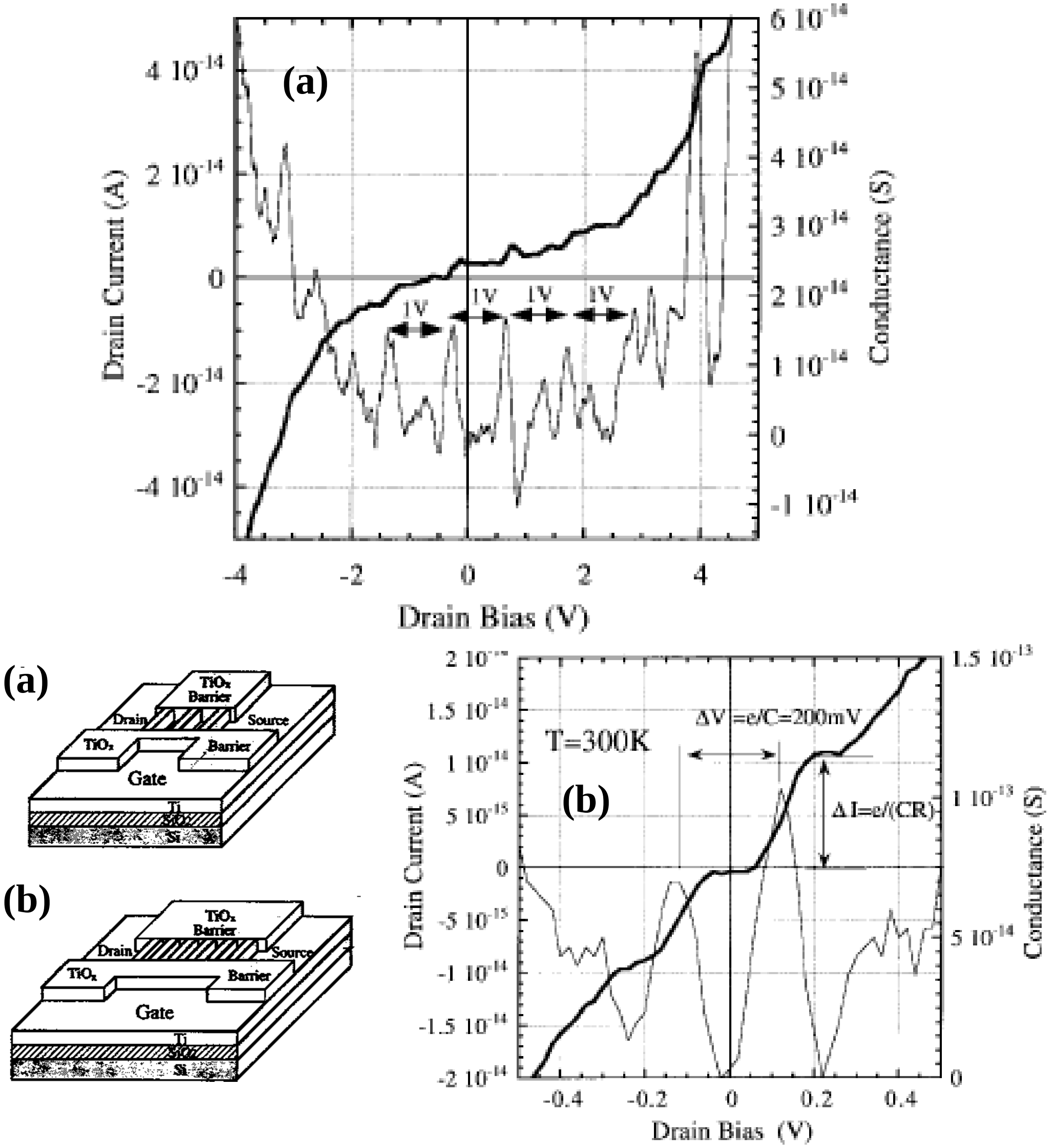

**Fig. 30. From Matsumoto, et al. [13]. I-V and dI/dV curves for a (a) 2 and (b) 5 island $TiO_2$ Coulomb blockade device. Note the similarities in these curves to those in Figures 25 and 26 for the case of an applied magnetic field.**

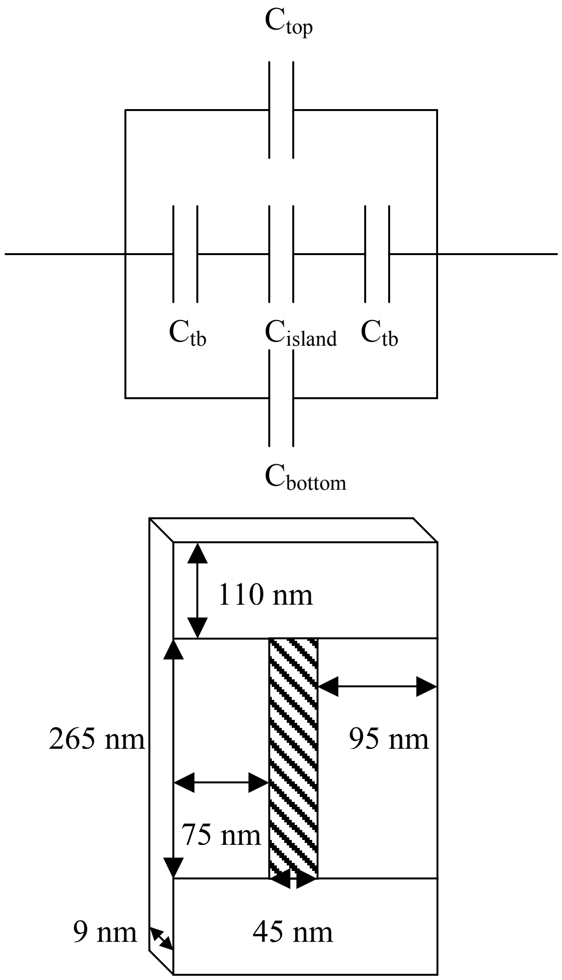

**Fig. 31. Ti device 1 capacitance is estimated assuming parallel plate capacitors for the tunnel barriers, $C_{tb}$, $C_{top}$ and $C_{bottom}$ and a cubic capacitor for $C_{island}$.**

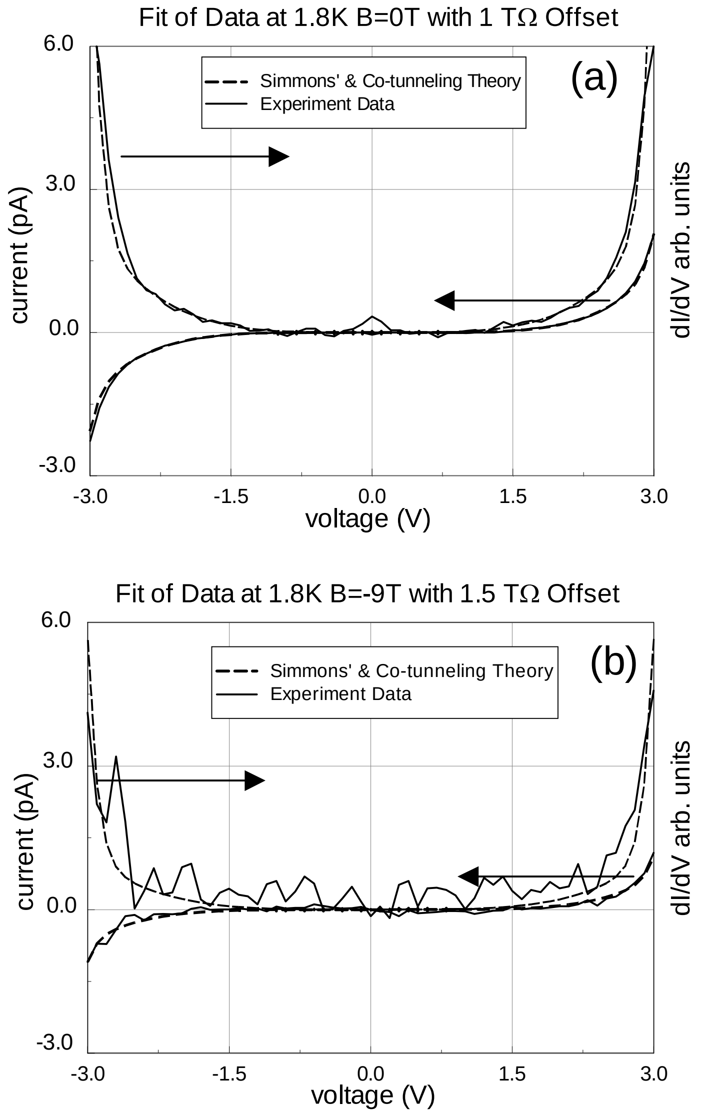

**Fig. 32. Plot of data fit to Simmons and inelastic cotunneling theories:**

$$I_{total} = \alpha I_{co-tunneling} + \beta I_{Simmons}$$

**(a) Data at 1.8 K with no magnetic field,** $\alpha, \beta = 1$

**(b) Data at 1.8K with -9T magnetic field,**

$\alpha = 0.5, \beta = 1$

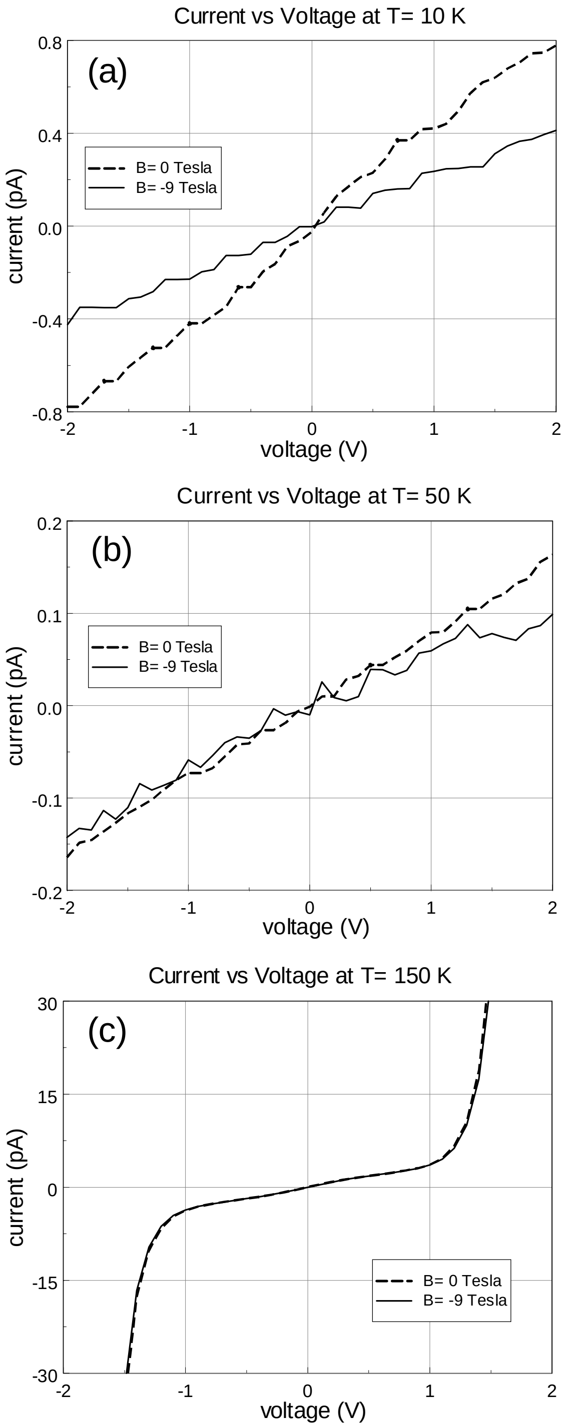
Current vs Voltage at T= 10 K

Current vs Voltage at T= 50 K

Current vs Voltage at T= 150 K

**Fig. 33. Nickel device I-V plots at (a) 10 K, (b) 50 K and (c) 150 K with and without 9T field. Dashed line is for no applied magnetic field.**

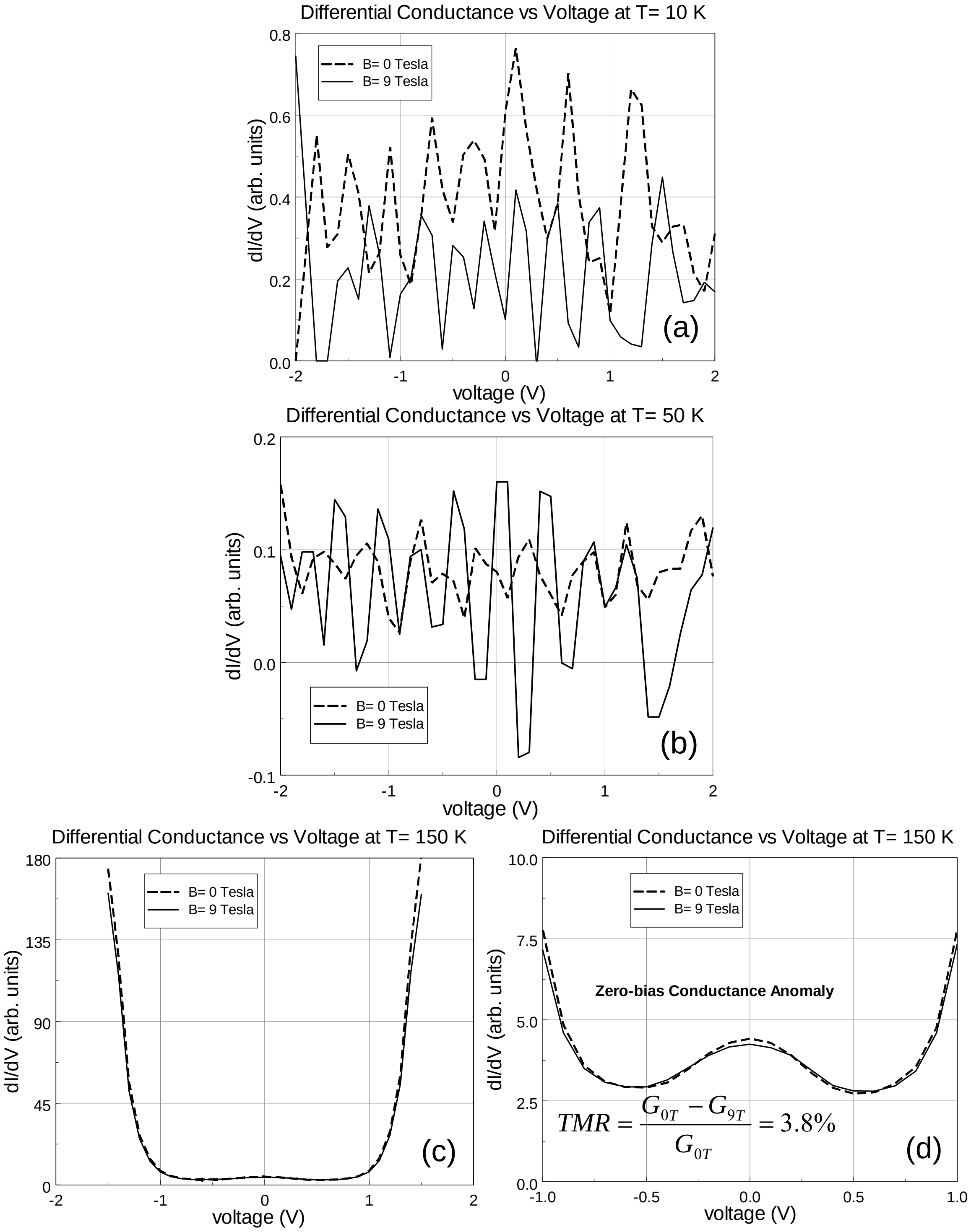

**Fig. 34. Nickel device I-V plots at (a) 10 K, (b) 50 K, and (c) 150 K with and without 9T field. Note zero-bias anomaly at 150 K (d). Dashed line is for no applied magnetic field.**

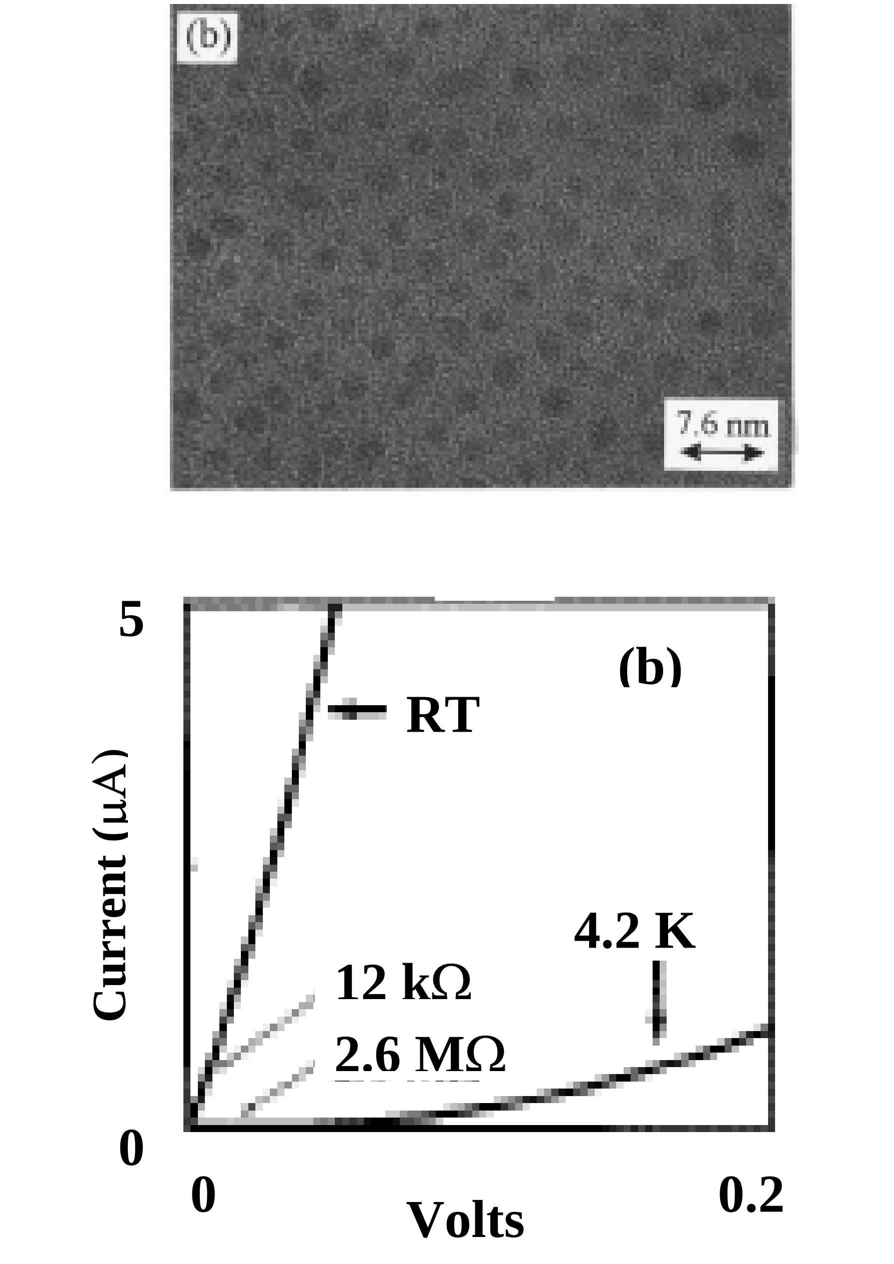

**Fig. 35. After Schelp, et al. [55]. Coulomb blockade at 4.2 K in Co nanoparticles embedded in $Al_2O_3$ where the ~0.05 V blockade is from the collective charging of the particles.**

# Appendices

## Appendix A: Nanolithography C programs for DI Nanoscope IIIa controller

### Box.c (draws a diamond/box in 4.43r1 standard)

```
#include <litho.h>

void main()

{

   LITHO_BEGIN

   LithoDisplayStatusBox();   //Display litho status box

   LithoScan(FALSE);   //turn off scanning

   LithoCenterXY();    //move tip to center

   double size=1.0;      //half-length of diagnolin microns

   double rate=.05;      //speed of tip in microns/sec

   //double bias=-10;    //initial bias setting

   //set bias to zero

   LithoSet(lsAna2,0);

   //move to bottom of first point

   LithoTranslate(size,0,rate);

   //turn on bias

   //LithoSet(lsAna2,bias);
```

```
   LithoPause(2);

   //move tip to draw box

   LithoTranslate(-size,size,rate);

   LithoTranslate(-size,-size,rate);

   LithoTranslate(size,-size,rate);

   LithoTranslate(size,size,rate);

   //turn off bias

   LithoPause(2);

   LithoSet(lsAna2,0);

    LITHO_END

}
```

**UT.c (draws a UT, in version 4.31)**

```
#include <litho.h>

void main()

{

   LITHO_BEGIN

   double size=.5;     //half-length of diagnolin microns

   double rate=.5;     //speed of tip in microns/sec
```

```
double bias=-6;    //initial bias setting

//set bias to zero

LithoSetOutput(aoAna2,0.0);

//move tip to initial point

LithoTranslate(0.0,0.1,rate);

//turn on bias

LithoSetOutput(aoAna2,bias);

//move tip to draw box

LithoTranslate(0,-size,rate);

LithoTranslate(.25,-.25,rate);

LithoTranslate(.25,0.0,rate);

LithoTranslate(.25,.25,rate);

LithoTranslate(0,size,rate);

LithoTranslate(.35,0,rate);

LithoTranslate(0,-.75,1);

LithoTranslate(0,.75,1);

LithoTranslate(.35,0,rate);
```

```
   //turn off bias
   LithoSetOutput(aoAna2,0);
   LITHO_END
}
```

**Point.c (draws two V’s on bottom and top, can easily edit just to make one V, in 4.43r1 standard)**

```
#include <litho.h>
void main()
{
   LITHO_BEGIN
   LithoDisplayStatusBox();   //Display litho status box
   LithoScan(FALSE);   //turn off scanning
   LithoCenterXY();    //move tip to center
   double size=2;      //length of diagnol in microns
   double rate=.1;      //speed of tip in microns/sec
   double bias=-12;   //initial bias setting
   //set bias to 0
   LithoSet(lsAna2,0);
```

```
LithoPause(1);

//move to bottom of left line

LithoTranslate(-size,-size,.5);

//turn on bias

LithoSet(lsAna2,bias);

LithoPause(1);

//move tip to draw bottom point

LithoTranslate(size,size,rate);

LithoTranslate(size,-size,rate);

//create oxide block

LithoTranslate(-1.7*size,0,rate);

LithoTranslate(0.7*size,0.7*size,rate);

LithoTranslate(0.7*size,-0.7*size,rate);

//LithoTranslate(-1.6*size,0,rate);

//LithoTranslate(0.8*size,0.8*size,rate);

//LithoTranslate(0.8*size,-0.8*size,rate);

//discharge bias

LithoSet(lsAna2,1);
```

```
LithoPause(1);

//move tip to center

LithoCenterXY();

//move tip to left of top line

LithoTranslate(-size,1.05*size,.5);

//turn on bias

LithoSet(lsAna2,bias);

LithoPause(1);

//move tip to draw left top point

LithoTranslate(size,-size,rate);

LithoTranslate(size,size,rate);

//create oxide block

LithoTranslate(-1.7*size,0,rate);

LithoTranslate(0.7*size,-0.7*size,rate);

LithoTranslate(0.7*size,0.7*size,rate);

//LithoTranslate(-1.6*size,0,rate);

//LithoTranslate(0.8*size,-0.8*size,rate);

//LithoTranslate(0.8*size,0.8*size,rate);
```

```
   //discharge bias
   LithoSet(lsAna2,1);
   LithoPause(2);
   LithoSet(lsAna2,0);
   LITHO_END
}
```

**Device.c (draws three V's on top and bottom to constrict current into a narrow point, then draws two barriers vertically through device to create central island, in 4.43r1 standard)**

```
#include <litho.h>
void main()
{
   LITHO_BEGIN
   LithoDisplayStatusBox();   //Display litho status box
   LithoScan(FALSE);   //turn off scanning
   LithoCenterXY();    //move tip to center
   double size=1.8;      //length of diagnol in microns
   double rate=0.1;   //speed of tip in microns/sec
```

```
double bias=-5;   //initial bias setting
//set bias to 0
LithoSet(lsAna2,0);
LithoPause(1);
//move to bottom of left line
LithoTranslate(-size,-size,.5);
//turn on bias
LithoSet(lsAna2,bias);
LithoPause(2);
//move tip to draw bottom point
LithoTranslate(size,size,rate);
LithoTranslate(size,-size,rate);
//create oxide block
LithoTranslate(-1.9*size,0,rate);
LithoTranslate(0.9*size,0.9*size,rate);
LithoTranslate(0.9*size,-0.9*size,rate);
LithoTranslate(-1.7*size,0,rate);
LithoTranslate(0.8*size,0.8*size,rate);
```

```
LithoTranslate(0.8*size,-0.8*size,rate);

LithoTranslate(-1.5*size,0,rate);

LithoTranslate(0.7*size,0.7*size,rate);

LithoTranslate(0.7*size,-0.7*size,rate);

//discharge bias

LithoSet(lsAna2,1);

LithoPause(2);

//move tip to center

LithoCenterXY();

//move tip to left of top line

LithoTranslate(-size,1.001*size,.5);

//turn on bias

//LithoSet(lsAna2,bias);

LithoPause(2);

//move tip to draw left top point

LithoTranslate(size,-size,rate);

LithoTranslate(size,size,rate);

//create oxide block
```

```
LithoTranslate(-1.9*size,0,rate);

LithoTranslate(0.9*size,-0.9*size,rate);

LithoTranslate(0.9*size,0.9*size,rate);

LithoTranslate(-1.7*size,0,rate);

LithoTranslate(0.8*size,-0.8*size,rate);

LithoTranslate(0.8*size,0.8*size,rate);

LithoTranslate(-1.5*size,0,rate);

LithoTranslate(0.7*size,-0.8*size,rate);

LithoTranslate(0.7*size,0.8*size,rate);

//discharge bias

LithoSet(lsAna2,1);

LithoPause(2);

LithoSet(lsAna2,0);

 //Draw island lines

LithoCenterXY();

LithoTranslate(-0.14*size,size,0.1);

LithoSet(lsAna2,-5);

LithoPause(1);
```

```
    LithoTranslate(0,-2*size,0.15);

    LithoTranslate(.055*size,0,0.15);

    LithoTranslate(0,2*size,0.15);

    //discharge

    LithoSet(lsAna2,1);

    LithoPause(2);

    LithoCenterXY();

    LithoSet(lsAna2,0);

    LITHO_END

}
```

## Appendix B: Operating Procedures for Karl Suss MJB-3 Mask Aligner

1) Turn on microscope light
2) Place the mask on the holder such that the Cr side of the mask in contact with the sample and area to be exposed is centered under hole, for a 5” mask, the mask holder will need to be rotated by 90 degrees, doing so will slightly pinch the vacuum hose, but will not cut off the vacuum.
3) Turn on vacuum to mask holder ensuring mask can not be easily moved
4) Place mask holder into aligner until flush, tighten knobs
5) Choose sample holder for wafer section so that wafer section will cover all holes on sample chuck, but use a chuck with as many holes as possible, place sample on holder and slide holder into aligner
6) Slowly push back contact lever located on left hand side so that it goes away from the controller, if sample will hit mask, lower sample and adjust the Z-control turn pot on the front (clockwise is down) so that sample will not hit the mask
7) Once contact leaver is moved all the way forward, look in microscope at sample, adjust Z-knob to left bringing sample into contact with mask. Once Z-knob is finger tight, lockdown with black lever.
8) Now pull separation lever towards the operator; separation light will come on. At this point the sample is free to be aligned with the mask using the position control knobs. Looking through the microscope the optimum alignment can be achieved adjusting the x, y and rotation.

9) Slowly push back separation lever and ensure sample did not move from aligned position. If so, one may need to turn down the Z knob a little (will need to unlock the turn pot) and readjust x, y & rotation, then slowly tighten (raise Z) again.
10) Turn time clock to 8 minutes, ensure power is at 275 Watts and that the 400 nm filter is on.
11) Press exposure button; sample will be exposed, do not look at sample (intense UV light is being emitted)
12) Once done being exposed, unlock Z, lower sample a little, then move contact lever towards the operator
13) Slide sample out, take off sample; turn off microscope light

Loosen mask holder knobs, slide out mask holder, flip over, turn off vacuum, take off mask.

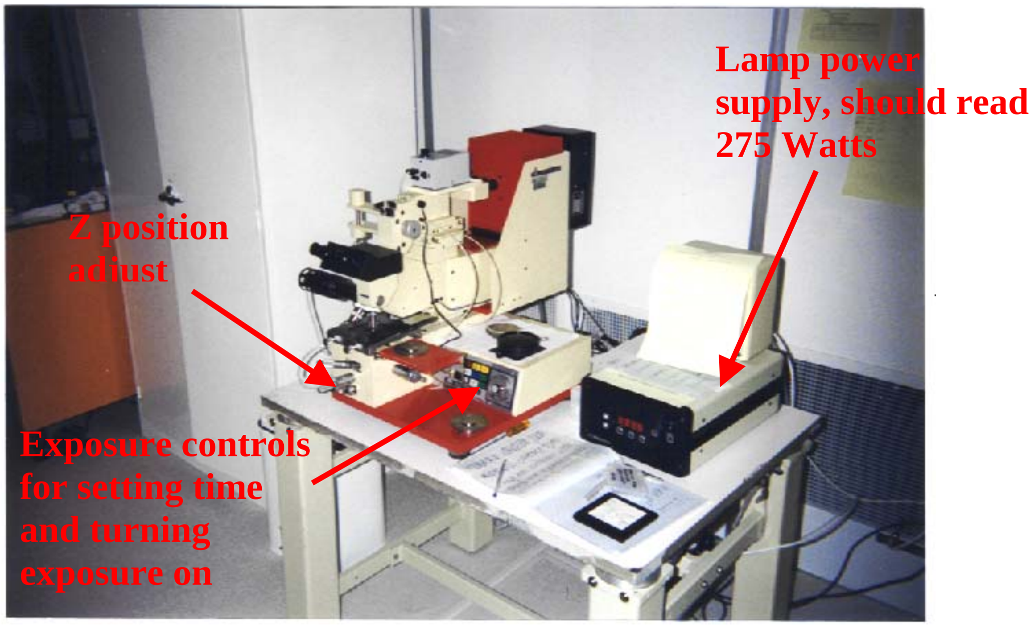

**Fig. A-1. Karl Suss MJB-3 mask aligner at The University of Texas at Austin.**

## Appendix C: Set-up and Operating Procedures for WestBond Wire Bonder

Preparation:

1) Turn the ultrasonic on and provide 30 minutes for source to warm up
2) Choose the proper wire bonder tool. For most of the applications at MRC, this means use a flat, 437mil length, $45^o$ angle tool, with 2025 sizing (2 mil diameter, 2.5 mil bond foot); the part number for the tool is Geiser 2145-2025-437-F.
3) Clean the surfaces to be bonded so that there are no oils. Use a cleaning fluid such as isopropyl.
4) Choose proper wire; usually want to match materials, however gold requires heater, while aluminum does not. Note that aluminum becomes brittle over time due to oxidation.
5) A pull strength on wire of 6-8 grams and 1.5-2 mils diameter wire for most applications is desired.
6) Place wire spool onto bonder, spools are marked with red and black, open at red end of spool and roll off the top and ensure the wire rolls off straight.
7) Insert tool so the top is flush with the transducer and entry hole for wire is in the back.
8) Switch open the clamp so the wire can feed; using tweezers, pull wire and feed through wire guide.
9) When there is enough to thread into tool, close clamp and thread wire into opening of tool (at $45^o$ angle). This is HARD to do for those without a light touch.

10) Set the force to ~20-25 grams (force is set using spring knob clockwise decreases force); Channel 1 to Power ~ 1.5/Timer ~ 1.4 and Channel 2 to Power ~ 1.8/ Timer ~ 1.9
11) Turn on sample heater if needed; can also turn on tool heat (softens wire)

Operating Procedures:

1) With the clamp closed, try a bond. Only on way to go for proper bonding: front to back. Need to change direction, rotate sample.
2) The sample stage rotates; rotating the stage also raises the sample up and down. The stage should be set so the tool just makes contact with the sample (don't want to go too hard), but adjust for best bonding.
3) Once ready to proceed, press down on the control lever. The wire will bond and the clamp will stay open to allow feed of wire to the next point, where after bonding the clamp will close breaking the wire.
4) In non-expert hands the tool is not a perfect bonder, but a little practice will result in bonds suitable for research devices.

In this manner, after about 1 hour for initial set-up, a half dozen devices could be wire bonded in each package at a rate of 10 minutes per device to allow for bonding errors (wires coming off, wire breaking, miswiring).

# Appendix D: LabVIEW Program Print-out

### 6430programaltVmethodnew.vi

### Connector Pane

### Front Panel

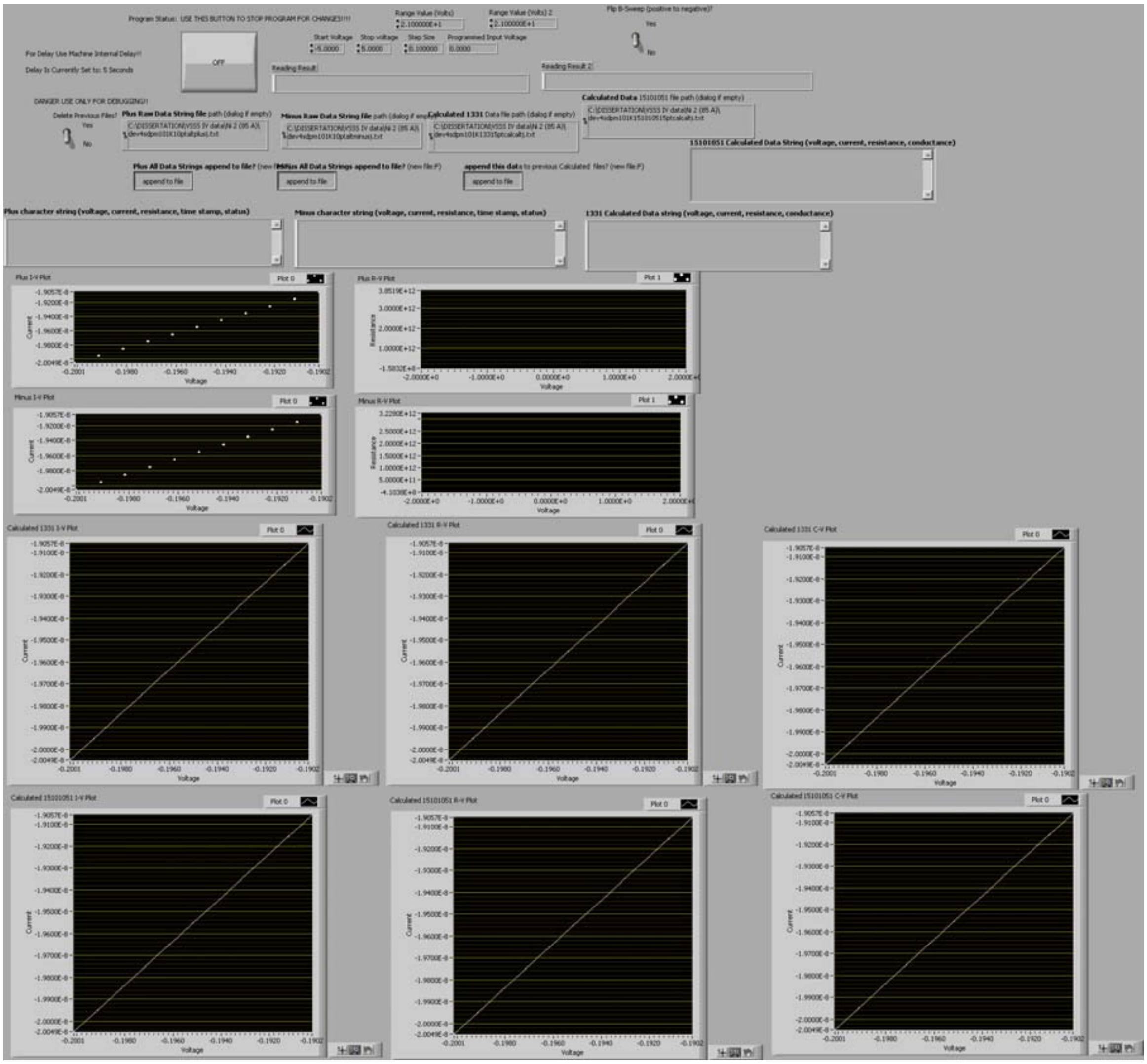

Program Status: USE THIS BUTTON TO STOP PROGRAM FOR CHANGES!!!!
Range Value (Volts): 2.100000E+1
Range Value (Volts) 2: 2.100000E+1
Flip B-Sweep (positive to negative)?
Start Voltage: -5.0000
Stop voltage: 5.0000
Step Size: 0.100000
Programmed Input Voltage: 0.0000
For Delay Use Machine Internal Delay!!
Delay Is Currently Set to: 5 Seconds
DANGER USE ONLY FOR DEBUGGING!!
Delete Previous Files?
Plus Raw Data String file path (dialog if empty): C:\DISSERTATION\VSSS IV data\Ni 2 (85 A)\dev4sdpm101K10ptaltplus1.txt
Minus Raw Data String file path (dialog if empty): C:\DISSERTATION\VSSS IV data\Ni 2 (85 A)\dev4sdpm101K10ptaltminus1.txt
Calculated 1331 Data file path (dialog if empty): C:\DISSERTATION\VSSS IV data\Ni 2 (85 A)\dev4sdpm101K1331ptcalcalt1.txt
Calculated Data 15101051 file path (dialog if empty): C:\DISSERTATION\VSSS IV data\Ni 2 (85 A)\dev4sdpm101K1510105 15ptcalcalt1.txt

## Controls and Indicators

DBL **Start Voltage**

DBL **Step Size** Size of voltage steps

DBL **Stop voltage**

**Delete Previous Files?** If readjusting parameters deletes already saved files with same name instead of appending to them

**Plus Raw Data String file path (dialog if empty) file path** is the path name of the file. If file path is empty (default) or is Not A Path, the VI displays a dialog box from which you can select a file. Error 43 occurs if you cancel the dialog box.

**Plus All Data Strings append to file? (new file:F) append to file?** indicates whether to append the data to an existing file.

**Program Status: USE THIS BUTTON TO STOP PROGRAM FOR CHANGES!!!!** Hit this button and wait for program to stop, or else there will be a hang-up (6430 will freeze)

**Range Value (Volts)** This specifies the specific Source range value to use.

**Range Value (Volts) 2** This specifies the specific Source range value to use.

**Minus All Data Strings append to file? (new file:F) append to file?** indicates whether to append the data to an existing file.

**Minus Raw Data String file path (dialog if empty) file path** is the path name of the file. If file path is empty (default) or is Not A Path, the VI displays a dialog box from which you can select a file. Error 43 occurs if you cancel the dialog box.

**Calculated 1331 Data file path (dialog if empty) file path** is the path name of the file. If file path is empty (default) or is Not A Path, the VI displays a dialog box from which you can select a file. Error 43 occurs if you cancel the dialog box.

**append this data to previous Calculated files? (new file:F) append to file?** indicates whether to append the data to an existing file.

**Calculated Data 15101051 file path (dialog if empty) file path** is the path name of the file. If file path is empty (default) or is Not A Path, the VI displays a dialog box from which you can select a file. Error 43 occurs if you cancel the dialog box.

**Flip B-Sweep (positive to negative)?** Turning this on has the magnetic field start at 9 T versus – 9 T

**Reading Result** System displays last two readings, this is one of them

**Programmed Input Voltage**

**Plus character string (voltage, current, resistance, time stamp, status) character string** is the data read from the file.

**Plus I-V Plot** The I-V plot based on the portion of the alternating bias method matching input voltage

**Plus R-V Plot** The R-V plot based on the portion of the alternating bias method matching input voltage

**Reading Result 2** System displays last two readings, this is one of them

**Minus character string (voltage, current, resistance, time stamp, status) character string** is the data read from the file.

**Minus R-V Plot** The R-V plot based on the portion of the alternating bias method matching -1 times input voltage

**Minus I-V Plot** The I-V plot based on the portion of the alternating bias method matching -1 times input voltage

**15101051 Calculated Data String (voltage, current, resistance, conductance)** is the calculated fourth order correctiondata

**1331 Calculated Data string (voltage, current, resistance, conductance)** is the calculated second order correction data

**Calculated 15101051 R-V Plot** Shows running plot of data after performing alternate bias method

**Calculated 15101051 I-V Plot** Shows running plot of data after performing alternate bias method

**Calculated 1331 R-V Plot** Shows running plot of data after performing alternate bias method

**Calculated 1331 I-V Plot** Shows running plot of data after performing alternate bias method

**Calculated 1331 C-V Plot** Shows running plot of data after performing alternate bias method

**Calculated 15101051 C-V Plot** Shows running plot of data after performing alternate bias method

## Block Diagram

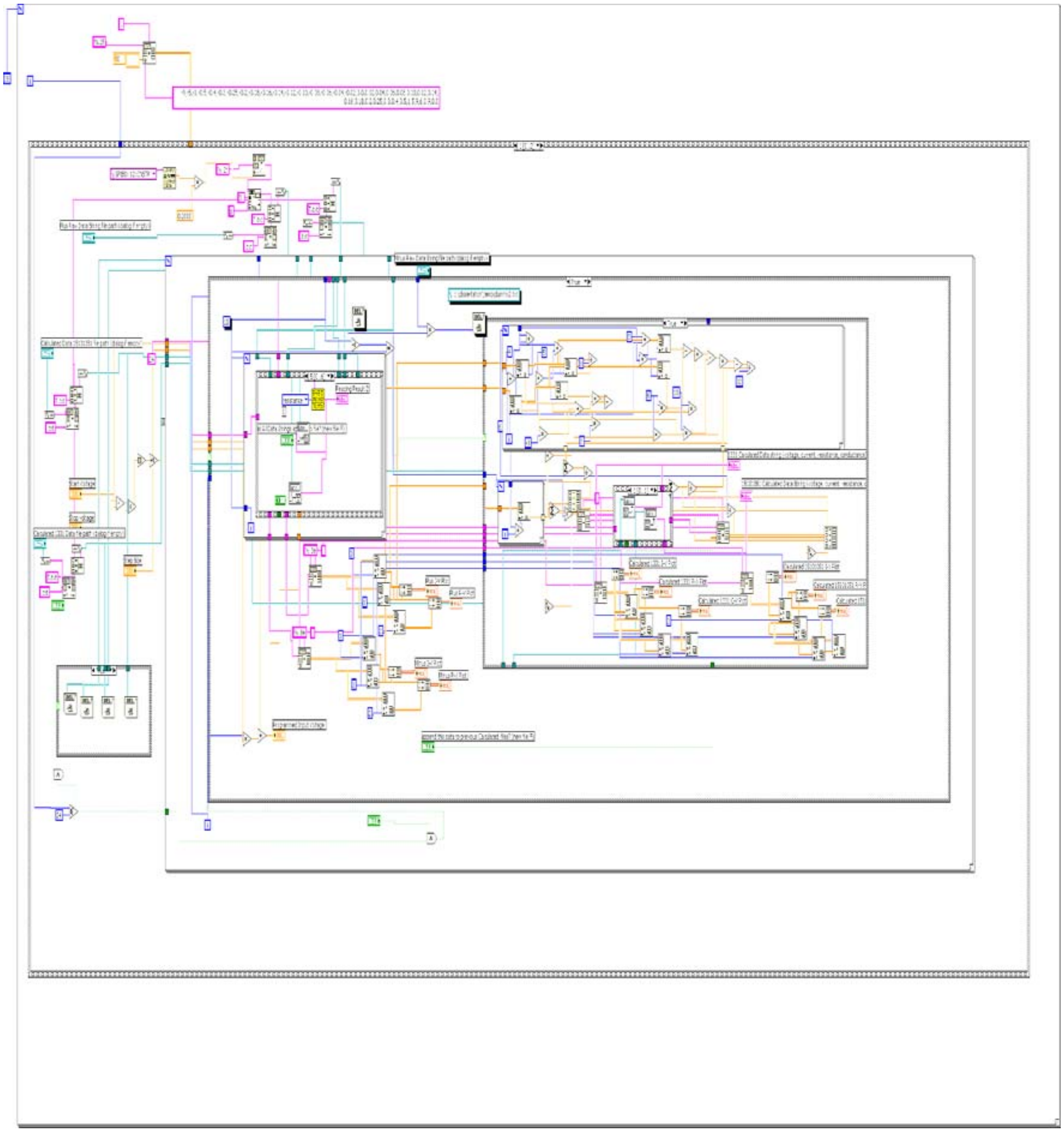

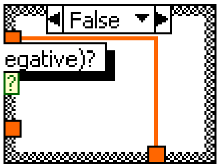

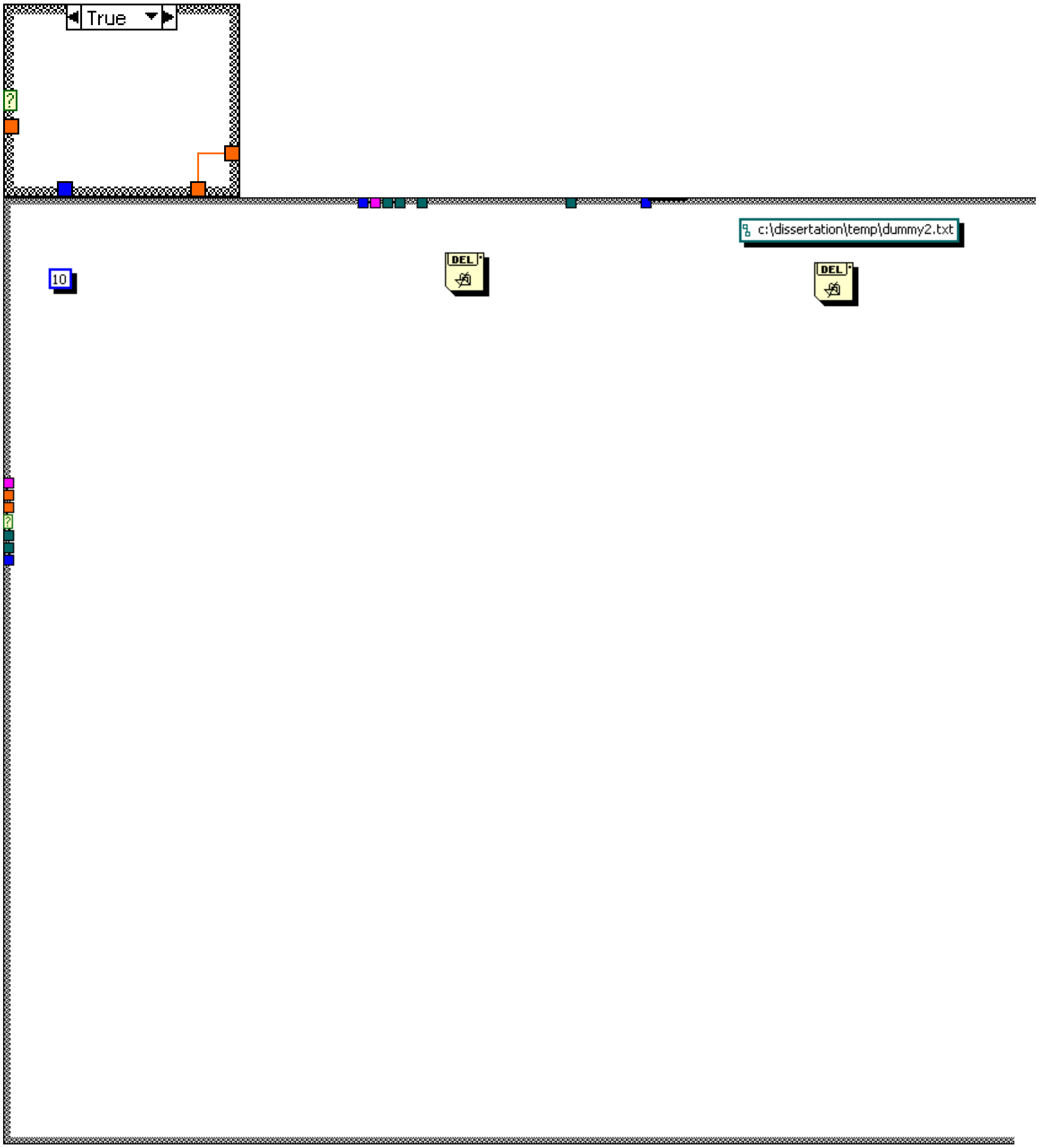
True
10
DEL
c:\dissertation\temp\dummy2.txt
DEL

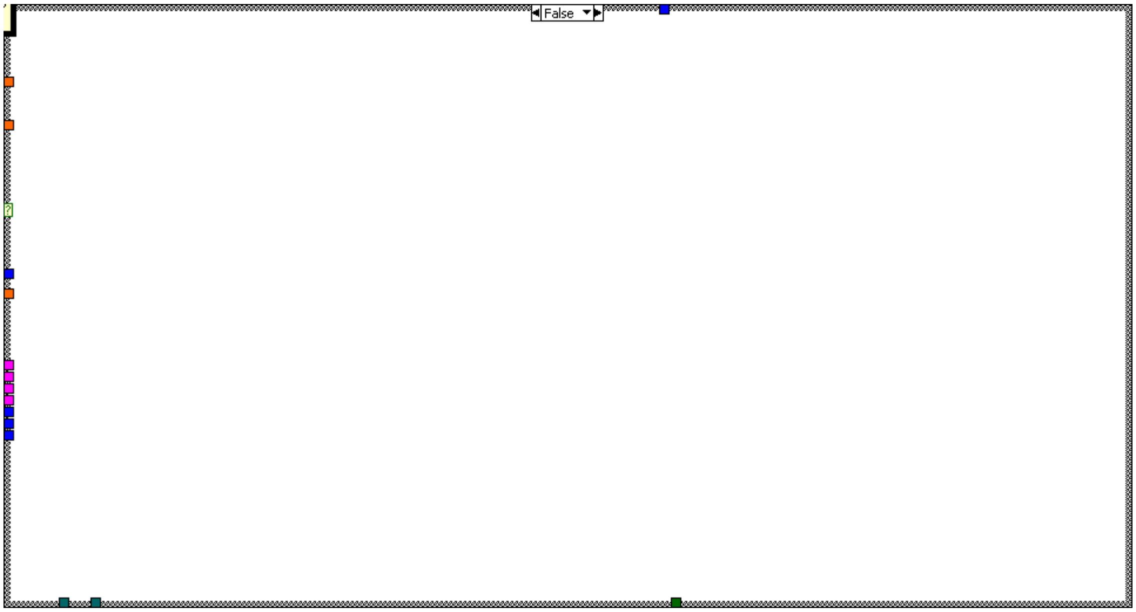

False

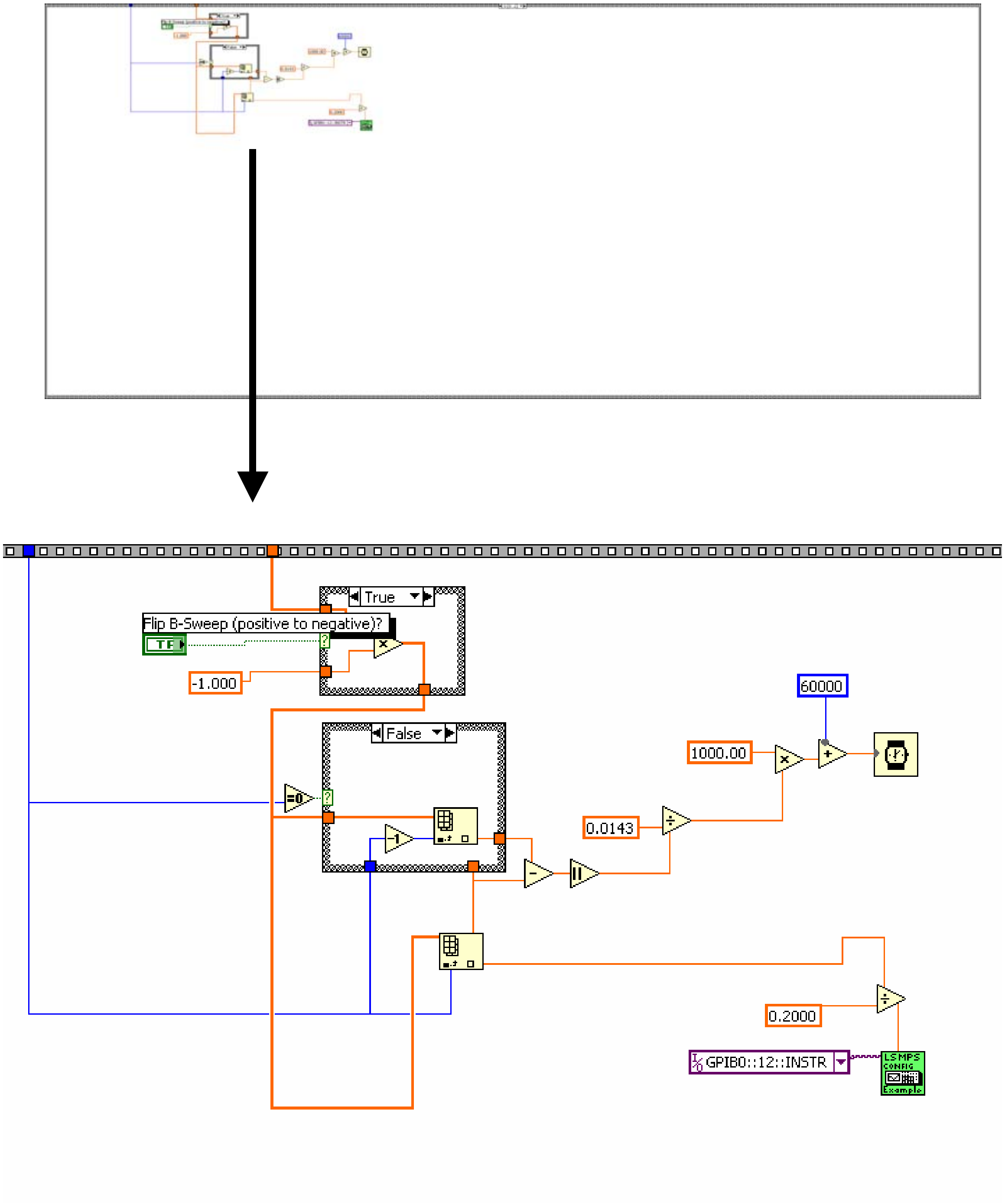
True
Flip B-Sweep (positive to negative)?
TF
-1.000
False
60000
1000.00
0.0143
0.2000
GPIB0::12::INSTR
LS MPS CONFIG Example

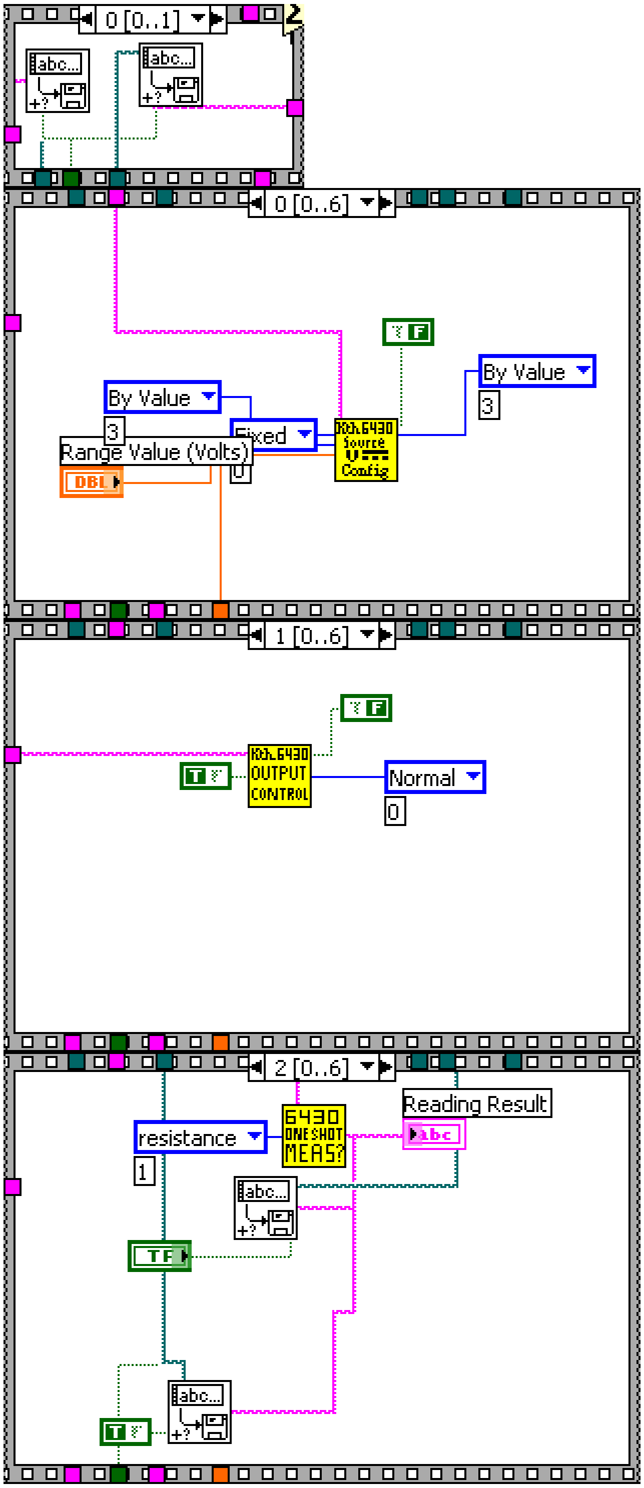
0 [0..1]
2
abc...
abc...
0 [0..6]
By Value
3
Range Value (Volts)
DBL
Fixed
0
Kth.6430 Source Config
F
By Value
3
1 [0..6]
F
Kth.6430 OUTPUT CONTROL
T
Normal
0
2 [0..6]
resistance
1
6430 ONE SHOT MEAS?
Reading Result
abc
abc...
TF
abc...
T

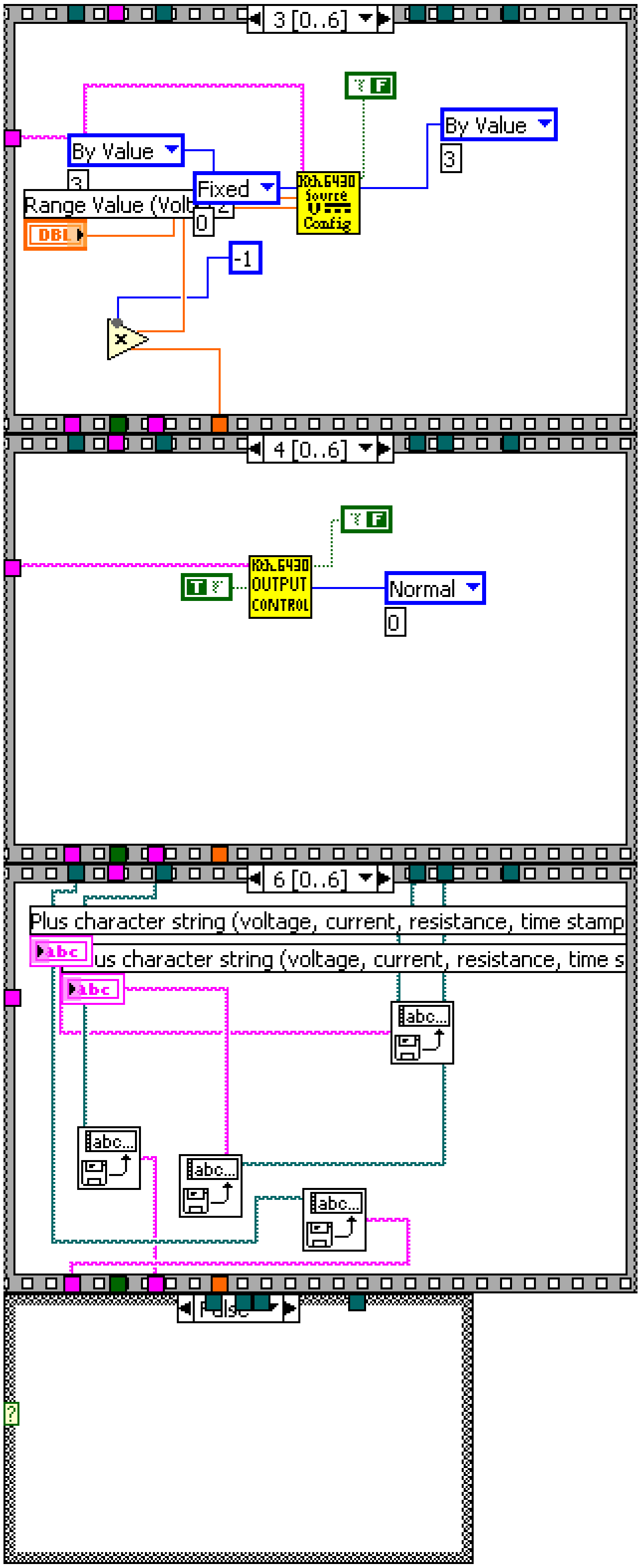3 [0..6]
By Value
3
Range Value (Volt
DBL
Fixed
0
2
T F
K6430 Source V Config
By Value
3
-1
4 [0..6]
T F
K6430 OUTPUT CONTROL
T F
Normal
0
6 [0..6]
Plus character string (voltage, current, resistance, time stamp
abc
us character string (voltage, current, resistance, time s
abc
abc...
abc...
abc...
abc...
False
?

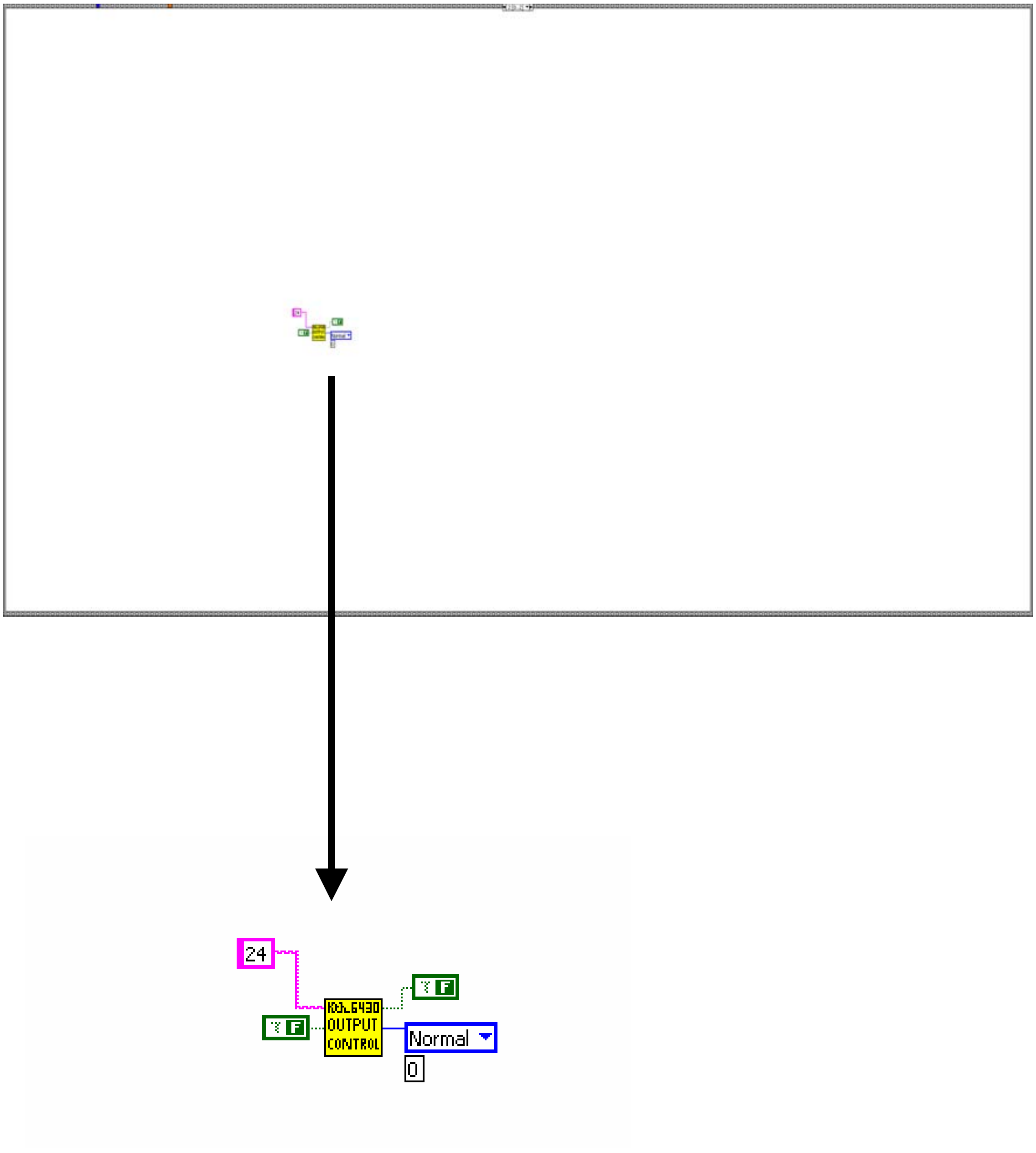
24
Kth 6430
OUTPUT
CONTROL
F
F
Normal
0

## List of SubVIs

**Keithley 6430 DCV Source Config.vi**

**Keithley 6430 One-Shot Measurewithtime-out.vi**
Edited sub-vi to allow a delay between voltage being turned on and current being read

**Keithley 6430 Output Control.VI**
Turns 6430 output on or off (blue light in front), key to use this and not manually do it while program is running

**Write Characters To File.vi**

**Read Characters From File.vi**

**LSCI MPS Application Settings/Limits Example.vi**
Controls Magnet

**LSCI MPS Data Output.vi**
Controls Magnet

## Position in Hierarchy

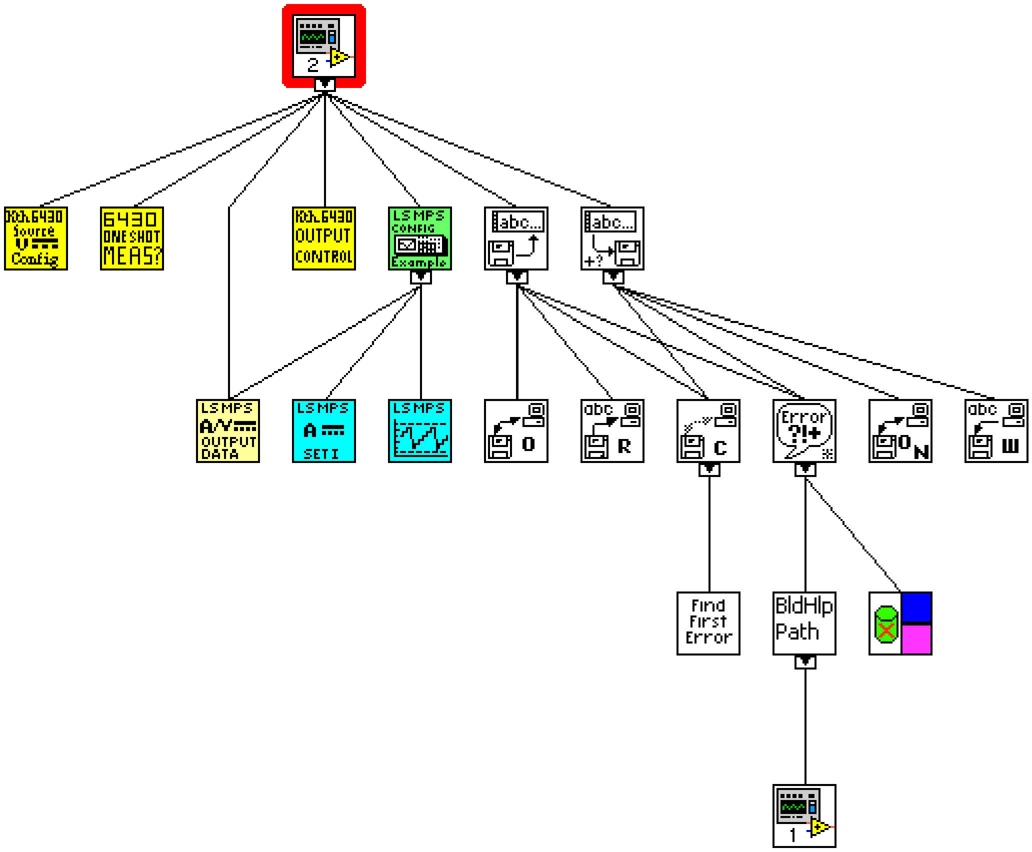

## Appendix E: Liquid He Cryostat Operation for LakeShore 9500 Hall Effect Measurement System

1) The first step is to order liquid He by Wednesday the week before you wish to test. The He will arrive the following Monday morning.
2) **(Warm start procedures)** Pump down the outer jackets with the turbo pump until they are at least $5x10^{-6}$ torr.
3) Insert sample rod into chamber, hook up the two heater and thermal couple connections (one big and one small).
4) When the liquid He arrives, turn on mechanical pump to vacuum out chamber & liquid He bath chamber (by opening up needle valve); perform several fill and purge cycles for these chambers with He gas attached to the He bath vent with the needle valve all the way open.
5) Close He bath chamber vent valve, turn off switch connecting pump to chamber
6) **(Start here if system already cold)** Hook He gas to liquid He dewar, turn off vent valve for liquid He dewar, open vent valve for He bath (let vent if some liquid He is present inside bath)
7) Slowly insert transfer tube into He dewar through top transfer tube opening and insert other end into He bath opening. Note, if liquid He is already present in bath wait until He liquid begins to come out of transfer tube.
8) Ensure you have ALL the proper fittings, there should minimal gas escaping, any lost pressure is lost He! There are two o-ring brass fittings needed to properly seal around the transfer tube end that is inserted into the liquid He dewar.

9) Connect the He gas to the He dewar, after He dewar completes blowing-off, slowly turn up gas to apply overpressure, but just enough so the sound of the He transferring from dewar to bath and boiling off is barely audible (whisper level). The transfer will take 4-6 hours (slow is good!)
10) When the temperature drops below 100 K, turn on liquid He level monitor.
11) Go approximately 5 minutes past 100% full on liquid He monitor; withdraw transfer tube simultaneously from both dewar and bath; close vent on bath; close vent to top hole in dewar
12) Plug in/turn-on mechanical vacuum pump to sample chamber; turn down needle valve so that it is one quarter turn counter-clockwise (open) from fully closed.
13) Let system sit at least for ~ 4 hours to settle before doing I-V measurements.

When testing samples at higher temperatures, close needle valve if desired sample temperature is above 5 K and set temperature on temperature controller accordingly.

# Appendix F: Mathcad Fitting Program No B Field

$$m := 2.5\cdot 9.109\cdot 10^{-31}$$

$$s := 1.6022\cdot 10^{-19}$$

$$Ctot := 0.6\cdot 10^{-18}$$

$$Cb := 1.11\cdot 10^{-18}$$

$$h := 6.626\cdot 10^{-34}$$

$$k := 1.3807\cdot 10^{-23}$$

$$T := 1.8$$

$$Ea := .5388\cdot k$$

$$K := 5$$

$$Cg := .47\cdot 10^{-18}$$

$$Ea = 7.4392116\times 10^{-24}$$

$$area := 9\cdot 265\cdot 10^{-14}$$

$$k\frac{T}{s} = 1.55115466233928\times 10^{-4}$$

$$k\frac{150}{s} = 1.29262888528274\times 10^{-2}$$

$$s2(\phi,t) := t\cdot 10^{10} - \frac{6}{K\cdot\phi}$$

$$s1(\phi) := \frac{6}{K\cdot\phi}$$

$$s21(\phi,t,V) := t\cdot 10^{10}\cdot\left(1 - \frac{46}{3\cdot\phi\cdot K\cdot t\cdot 10^{10} + 20 - 2\cdot V\cdot K\cdot t\cdot 10^{10}}\right) + s1(\phi)$$

$$s22(\phi,t,V) := \frac{\left(\phi\cdot K\cdot t\cdot 10^{10} - 28\right)}{K\cdot V}$$

$$\phi I1(\phi,t,V) := \phi - \left(\frac{V}{2\cdot t\cdot 10^{10}}\right)\cdot(s1(\phi) + s21(\phi,t,V)) - \left[\frac{5.75}{K\cdot(s21(\phi,t,V) - s1(\phi))}\right]\cdot\ln\left[s21(\phi,t,V)\cdot\frac{\left(t\cdot 10^{10} - s1(\phi)\right)}{s1(\phi)\cdot\left(t\cdot 10^{10} - s21(\phi,t,V)\right)}\right]$$

$$\phi I2(\phi,t,V) := \phi - \left(\frac{V}{2\cdot t\cdot 10^{10}}\right)\cdot(s1(\phi) + s22(\phi,t,V)) - \left[\frac{5.75}{K\cdot(s22(\phi,t,V) - s1(\phi))}\right]\cdot\ln\left[s21(\phi,t,V)\cdot\frac{\left(t\cdot 10^{10} - s1(\phi)\right)}{s1(\phi)\cdot\left(t\cdot 10^{10} - s22(\phi,t,V)\right)}\right]$$

$$I1L(\phi,t,V) := \left[area\cdot 6.2\cdot\frac{10^{10}}{(s21(\phi,t,V) - s1(\phi))^{2}}\right]\cdot\left[\left[(\phi I1(\phi,t,V))\cdot e^{\left[-1.025\cdot(s21(\phi,t,V)-s1(\phi))\cdot\phi I1(\phi,t,V)^{\frac{1}{2}}\right]}\right]\cdots + -(\phi I1(\phi,t,V) + V)\cdot e^{\left[-1.025\cdot(s21(\phi,t,V)-s1(\phi))\cdot(\phi I1(\phi,t,V)+V)^{\frac{1}{2}}\right]}\right]$$

$$I3L(\phi,t,V) := \left[area\cdot 6.2\cdot\frac{10^{10}}{(s22(\phi,t,V) - s1(\phi))^{2}}\right]\cdot\left[(\phi I2(\phi,t,V))\cdot e^{\left[-1.025\cdot\left(\phi I2(\phi,t,V)^{\frac{1}{2}}\right)\cdot(s22(\phi,t,V)-s1(\phi))\right]}\cdots + -(\phi I2(\phi,t,V) + V)\cdot e^{\left[-1.025\cdot(s22(\phi,t,V)-s1(\phi))\cdot\left[(\phi I2(\phi,t,V)+V)^{\frac{1}{2}}\right]\right]}\right]$$

$$I3(\phi,t,V) := \mathrm{if}(V > \phi, I3L(\phi,t,V), I1L(\phi,t,V))$$

$$I4(\phi,t,V) := \mathrm{if}(V < 0, -I3(\phi,t,|V|), I3(\phi,t,V))$$

$$\phi := .308$$

$$\phi 3 := .308$$

$$Ef := 3.8\cdot s$$

$\mathrm{Roff1} := .91\cdot 10^{12}$

$\mathrm{Cg} = 4.7\times 10^{-19}$

$N := 233$

$\mathrm{C1} := .67\cdot 10^{-18}$

$t := 38\cdot 10^{-9}$

$\mathrm{t3} := 39.0\cdot 10^{-9}$

$\mathrm{t1} := 95\cdot 10^{-9}$

$\mathrm{Roff2} := .91\cdot 10^{12}$

$\mathrm{Ec} := .167\cdot s$

$\mathrm{Rt} := 1.01\cdot 10^{6}$

$\mathrm{C2} := .85\cdot 10^{-18}$

$\mathrm{Csum} := \mathrm{C1} + \mathrm{C2} + \mathrm{Cg}$

$$\mathrm{R2} := \frac{15\cdot \mathrm{Rt}}{34}$$

$$\mathrm{R1} := \frac{19\cdot \mathrm{Rt}}{34}$$

$$\mathrm{E1}(V) := \frac{s\cdot\left[s\cdot\left(N+\frac{1}{2}\right) - V\cdot(\mathrm{C2}+\mathrm{Cg})\right]}{\mathrm{Csum}}$$

$$\mathrm{E2}(V) := \frac{s\cdot\left[-s\cdot\left(N-\frac{1}{2}\right) - V\cdot(\mathrm{C1}+\mathrm{Cg})\right]}{\mathrm{Csum}}$$

$$\mathrm{Imqt}(V) := \left(\frac{h}{2\cdot\pi\cdot 12\cdot\pi\cdot s^{2}\cdot \mathrm{R1}\cdot \mathrm{R2}}\right)\cdot\left(\frac{1}{\mathrm{E2}(V)}+\frac{1}{\mathrm{E1}(V)}\right)^{2}\cdot\left[(s\cdot V)^{2} + (2\cdot\pi\cdot k\cdot T)^{2}\right]\cdot V$$

$$I(V) := \mathrm{I4}\left(\phi 3, \mathrm{t3}, \frac{19}{34}V\right)\cdot\left[\frac{\left[\pi\cdot\left(4\cdot\pi\cdot\frac{t}{h}\right)\cdot\frac{\sqrt{2\cdot m}\cdot k\cdot(T)}{2\sqrt{\phi\cdot s}}\right]}{\sin\left[\pi\cdot\left(4\cdot\pi\cdot\frac{t}{h}\right)\cdot\frac{\sqrt{2\cdot m}\cdot k\cdot(T)}{2\sqrt{\phi\cdot s}}\right]}\right]$$

$$\mathrm{G4}(V) := \frac{d}{dV}\mathrm{I4}(\phi 3, \mathrm{t3}, V)$$

$\mathrm{Imq}(V) := \mathrm{Imqt}(V) + I(V)$

$$\mathrm{Gmq}(V) := \frac{d}{dV}\mathrm{Imq}(V)$$

$$\left[\frac{\left[\pi\cdot\left(4\cdot\pi\cdot\frac{t}{h}\right)\cdot\frac{\sqrt{2\cdot m}\cdot k\cdot(T)}{2\sqrt{\phi\cdot s}}\right]}{\left|\sin\left[\pi\cdot\left(4\cdot\pi\cdot\frac{t}{h}\right)\cdot\frac{\sqrt{2\cdot m}\cdot k\cdot(T)}{2\sqrt{\phi\cdot s}}\right]\right|}\right] = 1.01228015172061\times 10^{0}$$

$i := 0, 1 .. 60$

X := READPRN("d:\dissertation research\Ti218.prn")

$V_{i} := X_{i,0}$

$\mathrm{Imq}_{i} := \mathrm{Imq}\left(V_{i}\right)$

$\mathrm{Gmq}_{i} := \mathrm{Gmq}\left(V_{i}\right)$

$I_{i} := I\left(V_{i}\right)$

X =

| | 0 | 1 | 2 | 3 |
|---|---|---|---|---|
| 0 | $-3.000767\cdot10^{0}$ | $-5.612287\cdot10^{-12}$ | $-5.612287\cdot10^{0}$ | $8.000605\cdot10^{0}$ |
| 1 | $-2.900638\cdot10^{0}$ | $-4.811195\cdot10^{-12}$ | $-4.811195\cdot10^{0}$ | $6.727674\cdot10^{0}$ |
| 2 | $-2.800489\cdot10^{0}$ | $-4.264911\cdot10^{-12}$ | $-4.264911\cdot10^{0}$ | $4.721871\cdot10^{0}$ |
| 3 | $-2.700663\cdot10^{0}$ | $-3.866704\cdot10^{-12}$ | $-3.866704\cdot10^{0}$ | $3.508463\cdot10^{0}$ |
| 4 | $-2.600522\cdot10^{0}$ | $-3.563485\cdot10^{-12}$ | $-3.563485\cdot10^{0}$ | $2.757286\cdot10^{0}$ |
| 5 | $-2.500379\cdot10^{0}$ | $-3.314465\cdot10^{-12}$ | $-3.314465\cdot10^{0}$ | $2.231915\cdot10^{0}$ |
| 6 | $-2.400627\cdot10^{0}$ | $-3.117236\cdot10^{-12}$ | $-3.117236\cdot10^{0}$ | $1.98591\cdot10^{0}$ |
| 7 | $-2.300496\cdot10^{0}$ | $-2.917512\cdot10^{-12}$ | $-2.917512\cdot10^{0}$ | $1.906943\cdot10^{0}$ |
| 8 | $-2.200741\cdot10^{0}$ | $-2.736033\cdot10^{-12}$ | $-2.736033\cdot10^{0}$ | $1.694153\cdot10^{0}$ |
| 9 | $-2.100651\cdot10^{0}$ | $-2.578986\cdot10^{-12}$ | $-2.578986\cdot10^{0}$ | $1.560093\cdot10^{0}$ |
| 10 | $-2.000502\cdot10^{0}$ | $-2.423642\cdot10^{-12}$ | $-2.423642\cdot10^{0}$ | $1.596715\cdot10^{0}$ |
| 11 | $-1.900768\cdot10^{0}$ | $-2.259849\cdot10^{-12}$ | $-2.259849\cdot10^{0}$ | $1.479558\cdot10^{0}$ |
| 12 | $-1.800645\cdot10^{0}$ | $-2.128005\cdot10^{-12}$ | $-2.128005\cdot10^{0}$ | $1.319456\cdot10^{0}$ |
| 13 | $-1.700868\cdot10^{0}$ | $-1.99609\cdot10^{-12}$ | $-1.99609\cdot10^{0}$ | $1.354494\cdot10^{0}$ |
| 14 | $-1.600779\cdot10^{0}$ | $-1.857277\cdot10^{-12}$ | $-1.857277\cdot10^{0}$ | $1.292878\cdot10^{0}$ |
| 15 | $-1.500665\cdot10^{0}$ | $-1.737255\cdot10^{-12}$ | $-1.737255\cdot10^{0}$ | $1.296513\cdot10^{0}$ |

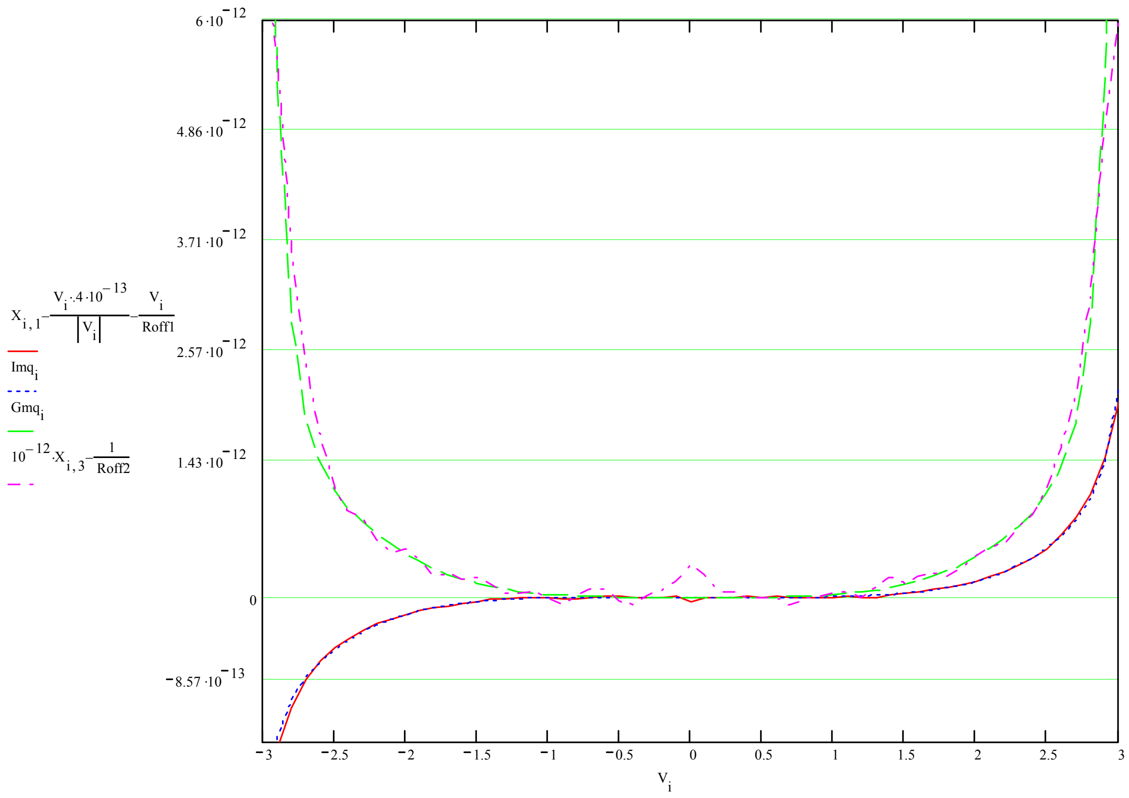

$Z_{i,0} := V_i$

$Z_{i,1} := Imq_i$

$$Z_{i,2} := X_{i,1} - \frac{V_i \cdot .4 \cdot 10^{-13}}{\left|V_i\right|} - \frac{V_i}{Roff1}$$

$Z_{i,3} := Gmq_i$

$$Z_{i,4} := 10^{-12} \cdot X_{i,3} - \frac{1}{Roff2}$$

Z =

| | 0 | 1 | 2 |
|---|---|---|---|
| 0 | $-3.000767 \cdot 10^{0}$ | $-2.27194916607639 \cdot 10^{-12}$ | $-2.27474084615385 \cdot 10^{-12}$ |
| 1 | $-2.900638 \cdot 10^{0}$ | $-1.4562436576627 \cdot 10^{-12}$ | $-1.58368071428571 \cdot 10^{-12}$ |
| 2 | $-2.800489 \cdot 10^{0}$ | $-1.05781054056818 \cdot 10^{-12}$ | $-1.14745056043956 \cdot 10^{-12}$ |
| 3 | $-2.700663 \cdot 10^{0}$ | $-8.28548821795262 \cdot 10^{-13}$ | $-8.58942461538462 \cdot 10^{-13}$ |
| 4 | $-2.600522 \cdot 10^{0}$ | $-6.70005298524861 \cdot 10^{-13}$ | $-6.65768516483517 \cdot 10^{-13}$ |
| 5 | $-2.500379 \cdot 10^{0}$ | $-5.46746106683401 \cdot 10^{-13}$ | $-5.26795769230769 \cdot 10^{-13}$ |
| 6 | $-2.400627 \cdot 10^{0}$ | $-4.45706217789323 \cdot 10^{-13}$ | $-4.39184351648352 \cdot 10^{-13}$ |
| 7 | $-2.300496 \cdot 10^{0}$ | $-3.60707771232798 \cdot 10^{-13}$ | $-3.49494417582418 \cdot 10^{-13}$ |
| 8 | $-2.200741 \cdot 10^{0}$ | $-2.89650745355851 \cdot 10^{-13}$ | $-2.77636296703297 \cdot 10^{-13}$ |
| 9 | $-2.100651 \cdot 10^{0}$ | $-2.30129481756365 \cdot 10^{-13}$ | $-2.30578307692308 \cdot 10^{-13}$ |
| 10 | $-2.000502 \cdot 10^{0}$ | $-1.80810031958517 \cdot 10^{-13}$ | $-1.85288153846154 \cdot 10^{-13}$ |
| 11 | $-1.900768 \cdot 10^{0}$ | $-1.40491063501138 \cdot 10^{-13}$ | $-1.31092956043956 \cdot 10^{-13}$ |
| 12 | $-1.800645 \cdot 10^{0}$ | $-1.07597290425565 \cdot 10^{-13}$ | $-1.09274230769231 \cdot 10^{-13}$ |
| 13 | $-1.700868 \cdot 10^{0}$ | $-8.12584109160694 \cdot 10^{-14}$ | $-8.70042857142855 \cdot 10^{-14}$ |
| 14 | $-1.600779 \cdot 10^{0}$ | $-6.02933309796864 \cdot 10^{-14}$ | $-5.81791978021977 \cdot 10^{-14}$ |
| 15 | $-1.500665 \cdot 10^{0}$ | $-4.38943805835487 \cdot 10^{-14}$ | $-4.81725824175825 \cdot 10^{-14}$ |

d:\..\Ti218KnoBSimmonsfit.txt

Z

# Appendix G: Mathcad Fitting Program With B Field

$\mathrm{m} := 2.5\cdot 9.109\cdot 10^{-31}$

$\mathrm{s} := 1.6022\cdot 10^{-19}$

$\mathrm{Ctot} := 0.6\cdot 10^{-18}$

$\mathrm{Cb} := 0.67\cdot 10^{-18}$

$\mathrm{Cg} := .47\cdot 10^{-18}$

$\mathrm{h} := 6.626\cdot 10^{-34}$

$\mathrm{k} := 1.3807\cdot 10^{-23}$

$\mathrm{T} := 1.8$

$\mathrm{Ea} := .5388\cdot \mathrm{k}$

$\mathrm{K} := 5$

$\mathrm{Ea} = 7.4392116 \times 10^{-24}$

$\mathrm{k}\cdot\frac{\mathrm{T}}{\mathrm{s}} = 1.55115466233928 \times 10^{-4}$

$\mathrm{k}\cdot\frac{150}{\mathrm{s}} = 1.29262888528274 \times 10^{-2}$

$\mathrm{area} := 9\cdot 265\cdot 10^{-14}$

$$\mathrm{s1}(\phi) := \frac{6}{\mathrm{K}\cdot\phi}$$

$$\mathrm{s2}(\phi, t) := t\cdot 10^{10} - \frac{6}{\mathrm{K}\cdot\phi}$$

$$\mathrm{s21}(\phi, t, V) := t\cdot 10^{10}\cdot\left(1 - \frac{46}{3\cdot\phi\cdot \mathrm{K}\cdot t\cdot 10^{10} + 20 - 2\cdot V\cdot \mathrm{K}\cdot t\cdot 10^{10}}\right) + \mathrm{s1}(\phi)$$

$$\mathrm{s22}(\phi, t, V) := \frac{\left(\phi\cdot \mathrm{K}\cdot t\cdot 10^{10} - 28\right)}{\mathrm{K}\cdot V}$$

$$\phi\mathrm{I1}(\phi, t, V) := \phi - \left(\frac{V}{2\cdot t\cdot 10^{10}}\right)\cdot(\mathrm{s1}(\phi) + \mathrm{s21}(\phi, t, V)) - \left[\frac{5.75}{\mathrm{K}\cdot(\mathrm{s21}(\phi, t, V) - \mathrm{s1}(\phi))}\right]\cdot\ln\left[\mathrm{s21}(\phi, t, V)\cdot\frac{\left(t\cdot 10^{10} - \mathrm{s1}(\phi)\right)}{\mathrm{s1}(\phi)\cdot\left(t\cdot 10^{10} - \mathrm{s21}(\phi, t, V)\right)}\right]$$

$$\phi\mathrm{I2}(\phi, t, V) := \phi - \left(\frac{V}{2\cdot t\cdot 10^{10}}\right)\cdot(\mathrm{s1}(\phi) + \mathrm{s22}(\phi, t, V)) - \left[\frac{5.75}{\mathrm{K}\cdot(\mathrm{s22}(\phi, t, V) - \mathrm{s1}(\phi))}\right]\cdot\ln\left[\mathrm{s21}(\phi, t, V)\cdot\frac{\left(t\cdot 10^{10} - \mathrm{s1}(\phi)\right)}{\mathrm{s1}(\phi)\cdot\left(t\cdot 10^{10} - \mathrm{s22}(\phi, t, V)\right)}\right]$$

$$\mathrm{I1L}(\phi, t, V) := \left[\mathrm{area}\cdot 6.2\cdot\frac{10^{10}}{(\mathrm{s21}(\phi, t, V) - \mathrm{s1}(\phi))^{2}}\right]\cdot\left[\begin{array}{l}(\phi\mathrm{I1}(\phi, t, V))\cdot e^{\left[-1.025\cdot(\mathrm{s21}(\phi, t, V)-\mathrm{s1}(\phi))\cdot\phi\mathrm{I1}(\phi, t, V)^{\frac{1}{2}}\right]}\ \ldots\\ + -(\phi\mathrm{I1}(\phi, t, V) + V)\cdot e^{\left[-1.025\cdot(\mathrm{s21}(\phi, t, V)-\mathrm{s1}(\phi))\cdot(\phi\mathrm{I1}(\phi, t, V)+V)^{\frac{1}{2}}\right]}\end{array}\right]$$

$$\mathrm{I3L}(\phi, t, V) := \left[\mathrm{area}\cdot 6.2\cdot\frac{10^{10}}{(\mathrm{s22}(\phi, t, V) - \mathrm{s1}(\phi))^{2}}\right]\cdot\left[\begin{array}{l}\phi\mathrm{I2}(\phi, t, V)\cdot e^{\left[-1.025\cdot\left(\phi\mathrm{I2}(\phi, t, V)^{\frac{1}{2}}\right)\cdot(\mathrm{s22}(\phi, t, V)-\mathrm{s1}(\phi))\right]}\ \ldots\\ + -(\phi\mathrm{I2}(\phi, t, V) + V)\cdot e^{\left[-1.025\cdot(\mathrm{s22}(\phi, t, V)-\mathrm{s1}(\phi))\cdot\left[(\phi\mathrm{I2}(\phi, t, V)+V)^{\frac{1}{2}}\right]\right]}\end{array}\right]$$

$\mathrm{I3}(\phi, t, V) := \mathrm{if}(V > \phi, \mathrm{I3L}(\phi, t, V), \mathrm{I1L}(\phi, t, V))$

$\mathrm{I4}(\phi, t, V) := \mathrm{if}(V < 0, -\mathrm{I3}(\phi, t, |V|), \mathrm{I3}(\phi, t, V))$

$\mathrm{Ef} := 3.8\cdot\mathrm{s}$

$\mathrm{t1} := 95\cdot 10^{-9}$

$\mathrm{Cg} = 4.7 \times 10^{-19}$

$C2 := .85\cdot 10^{-18}$

$C1 := .67\cdot 10^{-18}$

$N := 233$

$Rt := 1.01\cdot 10^{6}$

$Ec := .167\cdot s$

$Csum := Cg + C1 + C2$

$$R2 := \frac{15\cdot Rt}{34}$$

$$R1 := \frac{19\cdot Rt}{34}$$

$$E1(V) := \frac{s\cdot\left[s\cdot\left(N+\frac{1}{2}\right) - V\cdot(C2 + Cg)\right]}{Csum}$$

$$E2(V) := \frac{s\cdot\left[-s\cdot\left(N-\frac{1}{2}\right) - V\cdot(C1 + Cg)\right]}{Csum}$$

$$Imqt(V) := \left(\frac{h}{2\cdot\pi\cdot 12\cdot\pi\cdot s^{2}\cdot R1\cdot R2}\right)\cdot\left(\frac{1}{E2(V)} + \frac{1}{E1(V)}\right)^{2}\cdot\left[(s\cdot V)^{2} + (2\cdot\pi\cdot k\cdot T)^{2}\right]\cdot V$$

$\phi := .308$

$\phi 3 := .308$

$t3 := 40\cdot 10^{-9}$

$t := 38\cdot 10^{-9}$

$Roff1 := 1.15\cdot 10^{12}$

$Roff2 := 1.9\cdot 10^{12}$

$$I(V) := I4\left(\phi 3, t3, \frac{19}{34}V\right)\cdot\left[\frac{\left[\pi\cdot\left(4\cdot\pi\cdot\frac{t}{h}\right)\cdot\frac{\sqrt{2\cdot m}\cdot k\cdot(T)}{2\sqrt{\phi\cdot s}}\right]}{\sin\left[\pi\cdot\left(4\cdot\pi\cdot\frac{t}{h}\right)\cdot\frac{\sqrt{2\cdot m}\cdot k\cdot(T)}{2\sqrt{\phi\cdot s}}\right]}\right]$$

$$\left[\frac{\left[\pi\cdot\left(4\cdot\pi\cdot\frac{t}{h}\right)\cdot\frac{\sqrt{2\cdot m}\cdot k\cdot(T)}{2\sqrt{\phi\cdot s}}\right]}{\left|\sin\left[\pi\cdot\left(4\cdot\pi\cdot\frac{t}{h}\right)\cdot\frac{\sqrt{2\cdot m}\cdot k\cdot(T)}{2\sqrt{\phi\cdot s}}\right]\right|}\right] = 1.01228015172061\times 10^{0}$$

$Imq(V) := .5\,Imqt(V) + I(V)$

$$Gmq(V) := \frac{d}{dV}Imq(V)$$

$i := 0, 1 .. 60$

X := READPRN("d:\dissertation research\Ti218B.prn")

$V_i := X_{i,0}$

$Imq_i := Imq\left(V_i\right)$

$Gmq_i := Gmq\left(V_i\right)$

X =

|  | 0 | 1 | 2 | 3 |
|---|---|---|---|---|
| 0 | $-3.00072\cdot10^{0}$ | $-3.70554\cdot10^{-12}$ | $-3.70554\cdot10^{0}$ | $4.667857\cdot10^{0}$ |
| 1 | $-2.900587\cdot10^{0}$ | $-3.238134\cdot10^{-12}$ | $-3.238134\cdot10^{0}$ | $2.757185\cdot10^{0}$ |
| 2 | $-2.800433\cdot10^{0}$ | $-3.153352\cdot10^{-12}$ | $-3.153352\cdot10^{0}$ | $2.373394\cdot10^{0}$ |
| 3 | $-2.700602\cdot10^{0}$ | $-2.763983\cdot10^{-12}$ | $-2.763983\cdot10^{0}$ | $3.754624\cdot10^{0}$ |
| 4 | $-2.600462\cdot10^{0}$ | $-2.402582\cdot10^{-12}$ | $-2.402582\cdot10^{0}$ | $2.386272\cdot10^{0}$ |
| 5 | $-2.500326\cdot10^{0}$ | $-2.286067\cdot10^{-12}$ | $-2.286067\cdot10^{0}$ | $5.817859\cdot10^{-1}$ |
| 6 | $-2.400578\cdot10^{0}$ | $-2.313686\cdot10^{-12}$ | $-2.286067\cdot10^{0}$ | $9.460351\cdot10^{-1}$ |
| 7 | $-2.300448\cdot10^{0}$ | $-2.096614\cdot10^{-12}$ | $-2.096614\cdot10^{0}$ | $1.422706\cdot10^{0}$ |
| 8 | $-2.200699\cdot10^{0}$ | $-2.001519\cdot10^{-12}$ | $-2.001519\cdot10^{0}$ | $8.749381\cdot10^{-1}$ |
| 9 | $-2.100616\cdot10^{0}$ | $-1.9218\cdot10^{-12}$ | $-1.9218\cdot10^{0}$ | $9.116881\cdot10^{-1}$ |
| 10 | $-2.000475\cdot10^{0}$ | $-1.818971\cdot10^{-12}$ | $-1.818971\cdot10^{0}$ | $1.436827\cdot10^{0}$ |
| 11 | $-1.900742\cdot10^{0}$ | $-1.634784\cdot10^{-12}$ | $-1.634784\cdot10^{0}$ | $1.515058\cdot10^{0}$ |
| 12 | $-1.800626\cdot10^{0}$ | $-1.516316\cdot10^{-12}$ | $-1.516316\cdot10^{0}$ | $7.64045\cdot10^{-1}$ |
| 13 | $-1.700855\cdot10^{0}$ | $-1.481916\cdot10^{-12}$ | $-1.481916\cdot10^{0}$ | $6.357089\cdot10^{-1}$ |
| 14 | $-1.600768\cdot10^{0}$ | $-1.389172\cdot10^{-12}$ | $-1.389172\cdot10^{0}$ | $9.063595\cdot10^{-1}$ |
| 15 | $-1.50066\cdot10^{0}$ | $-1.300468\cdot10^{-12}$ | $-1.300468\cdot10^{0}$ | $9.951067\cdot10^{-1}$ |

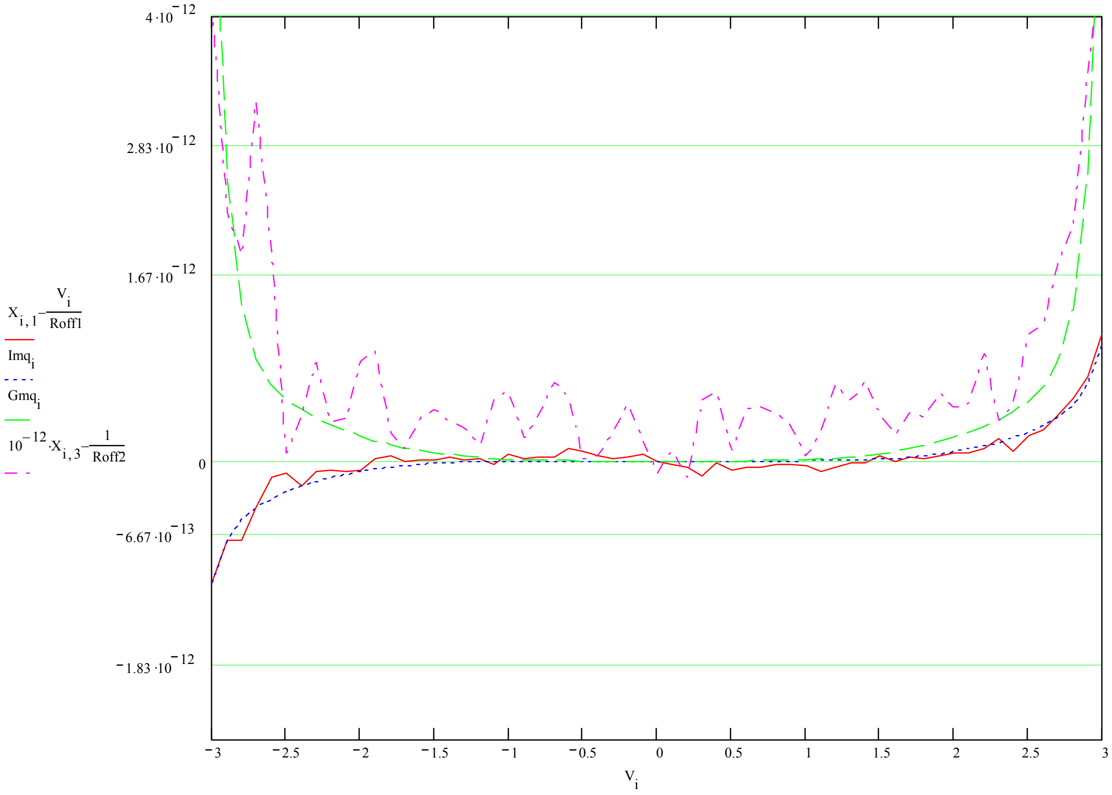

$Z_{i,0} := V_i$

$Z_{i,1} := Imq_i$

$Z_{i,2} := X_{i,1} - \frac{V_i}{Roff1}$

$Z_{i,3} := Gmq_i$

$Z_{i,4} := 10^{-12} \cdot X_{i,3} - \frac{1}{Roff2}$

$Z =$

|  | 0 | 1 | 2 |
|---|---|---|---|
| 0 | $-3.00072\cdot10^{0}$ | $-1.10103109553844\cdot10^{-12}$ | $-1.09621826086957\cdot10^{-12}$ |
| 1 | $-2.900587\cdot10^{0}$ | $-7.12514734799065\cdot10^{-13}$ | $-7.15884434782609\cdot10^{-13}$ |
| 2 | $-2.800433\cdot10^{0}$ | $-5.22662299858999\cdot10^{-13}$ | $-7.18192869565218\cdot10^{-13}$ |
| 3 | $-2.700602\cdot10^{0}$ | $-4.12005046348094\cdot10^{-13}$ | $-4.15633434782609\cdot10^{-13}$ |
| 4 | $-2.600462\cdot10^{0}$ | $-3.34250155832799\cdot10^{-13}$ | $-1.41310695652174\cdot10^{-13}$ |
| 5 | $-2.500326\cdot10^{0}$ | $-2.73139492593301\cdot10^{-13}$ | $-1.1187047826087\cdot10^{-13}$ |
| 6 | $-2.400578\cdot10^{0}$ | $-2.22778262052041\cdot10^{-13}$ | $-2.26226869565218\cdot10^{-13}$ |
| 7 | $-2.300448\cdot10^{0}$ | $-1.80323629275708\cdot10^{-13}$ | $-9.6224434782609\cdot10^{-14}$ |
| 8 | $-2.200699\cdot10^{0}$ | $-1.44809463878298\cdot10^{-13}$ | $-8.78676956521739\cdot10^{-14}$ |
| 9 | $-2.100616\cdot10^{0}$ | $-1.15054906524698\cdot10^{-13}$ | $-9.51773913043479\cdot10^{-14}$ |
| 10 | $-2.000475\cdot10^{0}$ | $-9.03989449464694\cdot10^{-14}$ | $-7.94275217391306\cdot10^{-14}$ |
| 11 | $-1.900742\cdot10^{0}$ | $-7.0240787949873\cdot10^{-14}$ | $1.80351304347826\cdot10^{-14}$ |
| 12 | $-1.800626\cdot10^{0}$ | $-5.37958477077169\cdot10^{-14}$ | $4.94457391304347\cdot10^{-14}$ |
| 13 | $-1.700855\cdot10^{0}$ | $-4.06276767398265\cdot10^{-14}$ | $-2.91165217391302\cdot10^{-15}$ |
| 14 | $-1.600768\cdot10^{0}$ | $-3.01456467206882\cdot10^{-14}$ | $2.80017391304353\cdot10^{-15}$ |
| 15 | $-1.50066\cdot10^{0}$ | $-2.19468310675692\cdot10^{-14}$ | $4.45373913043477\cdot10^{-15}$ |
| 16 | $-1.400865\cdot10^{0}$ | $-1.56547181051791\cdot10^{-14}$ | $2.78614782608697\cdot10^{-14}$ |
| 17 | $-1.300745\cdot10^{0}$ | $-1.08828471674355\cdot10^{-14}$ | $4.08760869565204\cdot10^{-15}$ |
| 18 | $-1.200915\cdot10^{0}$ | $-7.36122610879012\cdot10^{-15}$ | $2.12459130434783\cdot10^{-14}$ |
| 19 | $-1.100764\cdot10^{0}$ | $-4.80956837315253\cdot10^{-15}$ | $-3.60960130434782\cdot10^{-14}$ |

d:\..\Ti218KBSimmonsfit.txt

Z

# Bibliography

[1] G. Moore, Electronics **38** (8), (1965).

[2] E. Lerner, Indust. Phys. **6** (June), 18 (2000).

[3] PC Magazine website (http://www.pcmag.com).

[4] 2004 Int'l Tech. Roadmap for Semiconductors (http://www.itrs.net/common/2004update/2004.html).

[5] S. J. Vaughan-Nichols, Computer **36** (12), 21 (2003).

[6] Y. Miura, Digests of the Magnetic Recording Conference, IEEE Digests of the Meeting: August 27, 2002, p. AK1-01 (2002).

[7] S. Parkin, X. Jiang, C. Kaiser, A. Panchula, K. Roche, and M. Samant, Proc. IEEE **91**, 661 (2003).

[8] J. M. Daughton, A. V. Pohm, R. T. Fayfield, and C. H. Smith, J. Phys. D: Appl. Phys. **32**, R169 (1999).

[9] S. Natarajan, A. Alvandpour, IEEE MELECON, May 12-15, 2004 (2004).

[10] J. A. Dagata, J. Schneir, H. Harary, C. J. Evans, M. T. Postek, and J. Bennet, Appl. Phys. Lett. **56**, 2001 (1990).

[11] E. S. Snow, P. M. Campbell, and F. K. Perkins, Proc. of the IEEE **85**, 601 (1997).

[12] H. Sugimura, T. Uchida, N. Kitamura, and H. Masuhara, Appl. Phs. Lett. **63**, 1288 (1993).

[13] K. Matsumoto, Proc. of the IEEE **85** (4), 612 (1997).

[14] K. Matsumoto, M. Ishii, K. Segawa, Y. Oka, B. J. Vartanian, and J. S. Harris, Appl. Phys. Lett. **68**, 34 (1996).

[15] K. Matsumoto, Y. Gotoh, T. Maeda, J. A. Dagata, and J. S. Harris, Appl. Phys. Lett. **76**, 239 (2000).

[16] T. Ando, Y. Arakawa, K. Furuya, S. Komiyama, H. Nakashima, *Mesoscopic Physics and Electronics* (Springer, New York, 1998).

[17] For a review, see H. Grabert and M.H. Devoret, *Single Charge Tunneling* (Plenum Press, New York, 1992).

[18] D. V. Averin and Y. V. Nazarov in *Single Charge Tunneling* (S. M. Sze ed.), p. 217 (Plenum Press, New York, 1992).

[19] L. L. Sohn, L. P. Kouwenhoven, and G. Schon, *Mesoscopic Electron Transport,* p. 31 (Kluwer, Boston, 1997).

[20] L. I. Glazman in *Quantum Mesoscopic Phenomena and Mesoscopic Devices in Microelectronics* (I. O. Kulik and R. Ellialtioglu eds.), p. 105 (Kluwer, Netherlands, 2000).

[21] D. V. Averin and Y. V. Nazarov, Phys. Rev. Lett. **65**, 2446 (1990).

[22] J. G. Simmons, J. Appl. Phys. **34**, 1793 (1963).

[23] J. G. Simmons, J. Appl. Phys. **35**, 2655 (1964).

[24] For a review on tunneling phenomena, see E.L. Wolf, *Principles of Electron Tunneling Spectroscopy* (Oxford Univ. Press, New York, 1985).

[25] W. J. de Haas, J. de Boer, G . J. Van den Berg, Physica I, 1115 (1933).

[26] O. Ujsaghy, G. Zarand, A. Zawadowski, Sld. St. Comm **117**, 167 (2001).

[27] R. N. Hall, J. H. Racette, and H. Ehrenreich, Phys. Rev. Lett. **4**, 456 (1960).

[28] R. A. Logan and J. M. Rowell, Phys. Rev. Lett. **13**, 404 (1964).

[29] A. F. G. Wyatt, Phys. Rev. Lett. **13**, 401 (1964).

[30] J. Kondo, Progr. Theor. Phys. **32**, 37 (1964).

[31] L. Y. L. Shen and J. M. Rowell, Phys. Rev. **165**, 566 (1968).

[32] N. S. Wingreen, Mtls. Sc. Eng. B **84**, 22 (2001).

[33] J. Appelbaum, Phys. Rev. Lett. **17**, 91 (1966).

[34] J. Appelbaum, Phys. Rev. **154**, 633 (1967).

[35] J. R. Schrieffer and P. A. Wolff, Phys. Rev. **149**, 491 (1966).

[36] J. M. Rowell and L. Y. L. Shen, Phys. Rev. Lett. **17**, 15 (1966).

[37] A. F. G. Wyatt and D. J. Lythall, Phys. Lett. **25A**, 541 (1967).

[38] H. R. Zeller and I. Giaver, Phys. Rev. **181**, 789 (1969).

[39] F. Cerrina, C. Marrian, *Fabrication and Patterning at the Nanoscale: Matls. Rsch. Soc. Symp. Proc. Vol. 380* (Materials Research Society, Pittsburgh, 1995).

[40] J. A. Dagata, T. Inoue, J. Itoh, and H. Yokoyama, Appl. Phys. Lett. **73**, 271 (1998).

[41] P. Avouris, T. Hertel, and R. Martel, Appl. Phys. Lett. **71**, 285 (1997).

[42] C. R. K. Marrian and E. S. Snow, Microelectronic Eng. **32**, 173 (1996).

[43] J. I. Shirakashi, K. Matsumoto, N. Miura, and M. Konagi, Appl. Phys. Lett. **72**, 1893 (1998).

[44] Y. Okada, S. Amano, M. Kawabe, B. N. Shimbo, and J. S. Harris, Jr., J. Appl. Phys. **83**, 1844 (1998).

[45] U. F. Keyser, H. W. Schumacher, U. Zeitler, and R. J. Haug, Appl. Phys. Lett. **76**, 457 (2000).

[46] Veeco Instruments Inc., Woodbury, NY (http://www.veeco.com).

[47] M. Julliere, Phys. Lett. **54A**, 225 (1975).

[48] J.S. Moodera, Lisa R. Kinder, Terrilyn M. Wong, and R. Meservey, Phys. Rev. Lett. **74**, 3273 (1995).

[49] J. S. Moodera and L.R. Kinder, J. Appl. Phys. **79**, 4724 (1996).

[50] S-Y Bae and S. X. Wang, IEEE Trans. on Magnetics, **38**, 2721 (2002).

[51] Y. Ootuka, K. Ono, H.Shimada, R. Matsuda, A. Kinada, Mat. Sci. and Eng. B **84**, 114 (2001).

[52] M. B. A. Jalil, IEEE Trans on Magnetics, **38**, 2613 (2002).

[53] H. Wieldraaijer, P. LeClair, J.T. Kolhepp, H. J. M. Swagten, and W. J. M. de Jonge, IEEE Trans. on Magnetics **38**, 2727 (2002).

[54] P. M. Tedrow and R. Messervey, Phys. Rev. Lett. **26**, 192 (1971).

[55] L.F. Schelp, A. Fert, F. Fettar, P. Holoday, S.F. Lee, J.L. Maurice, F. Petroff, and A. Vaures, Phys. Rev. B **56**, R5747 (1997).

[56] K. Ono, H. Shimada and Y. Ootuka, Sld. St. Electr. **42**, 1407 (1998).

[57] Y. Ootuka, K. Ono, R. Matsuda, and H. Shimada, Microelectronic Eng. **47,** 409 (1999).

[58] H. Bruckl, G. Reiss, H. Vinzelberg, M. Bertram, I. Monch, and J. Schumann, Phys. Rev. B **58**, R8893 (1998).

[59] H. Kubota, Y. Fukumoto, S. Thamrongsing, Y. Ando, T. Miyazaki, and C. Yu, J. Appl. Phys. **87**, 5212 (2000).

[60] J. C. Wiemeri, T. A. Spencer, S. K. Banerjee, J. Appl. Phys. **97**, 084319 (2005).

[61] S. Iwabuchi, T. Tanamoto, R. Kitawaki, Physica B **249-251**, 276 (1998).

[62] R. Kitawaki, F. Wakaya, S. Iwabuchi, Microelectronic Eng. **47**, 413 (1999).

[63] J. Barnas and A. Fert, Phys. Rev. Lett. **80**, 1058 (1998).

[64] X. H. Wang and A. Brataas, Phys. Rev. Lett. **83**, 5138 (1999).

[65] H. Imamura, S. Takahashi, and S. Maekawa, Phys. Rev. B **59**, 6017 (1999).

[66] M. A. Khadar, V. Biju, and A. Inoue, Mtrls. Rsch. Bull. **38**, 1341 (2003).

[67] Lake Shore Cryotronics, Inc., Westerville, OH (http://www.lakeshore.com).

[68] Keithley Instruments, Inc., Cleveland, OH (http://www.keithley.com).

[69] A. Daire, "Improving the Repeatability of Ultra-High Resistance and Resistivity Measurements", Keithley White Paper 4645 (http://www.keithley.com).

[70] S. A. Campbell, H. S. Kim, D. C. Gilmer, B. HE, T. Ma, W. L. Gladfelter, IBMJ. Res. Develop. **43**, 383 (1999).

[71] K. Nabhors, S. Kim and J. White, IEEE Trans. Microwave Theory Tech. **42**, 1496 (1992).

[72] S.M. Sze, *Physics of Semiconductor Devices, 2nd ed.* (John Wiley & Sons, New York, 1981).

[73] S. Datar, P. M. Kumar, M. Sastry, C. V. Dharmadhikari, Colloids and Surfaces A: Physiochem. Eng Aspects **232**, 11 (2004).

[74] F. Mezei, Phys. Lett. **25A**, 534 (1967).

[75] G. V. Samsonov, *The Oxide Handbook* (IFI/Plenum, London, 1973).

# VITA

Jeffrey Charles Wiemeri was born in Elkhart, Indiana on April 5, 1972, the son of Beverly Jean Wiemeri and Charles August Wiemeri. After completing his work at Clay High School in South Bend, Indiana in 1990, he entered the University of Notre Dame, Notre Dame, Indiana. While at the University of Notre Dame he was enrolled in the United States Air Force Reserve Officers Training Corps. He received the degree of Bachelor of Science for Physics from the University of Notre Dame and a commission as a Second Lieutenant in the United States Air Force in May 1994. Immediately following graduation, he entered the Air Force Institute of Technology, Wright-Patterson Air Force Base where he received a Master of Science degree in Applied Physics in December 1995 with a thesis entitled "Electrical Characterization of 4H- and 6H-Silicon Carbide Schottky Diodes". His work was published and presented at two conferences. After his graduation, he was sent to the Avionics Directorate of Wright Laboratory, Wright-Patterson Air Force Base, where he conducted research on III-V semiconductor lasers which resulted in three publications, two conference presentations, and a patent. In August 1997, he entered the Graduate School at The University of Texas at Austin. For the next three and a half years he conducted research on AFM nanolithography of metals and silicon. In February 2001, the Air Force stationed him with the High Power Microwave Division, Directed Energy Directorate, Air Force Research Laboratory. While there, he continued his doctoral research and served as Deputy Branch Chief and Branch Chief of two branches developing and transitioning High Power Microwave technology to the Department of Defense. Under his leadership, his branches received over 30 awards, including four Air Force and two national level awards. In 2004, he was promoted to the rank of Major. In 2005, his work on magnetic field effects on Coulomb blockade conductance oscillations was published in the *Journal of Applied Physics*. He is the recipient of the Air Force Meritorious Service Medal, the Air Force Commendation Medal, and was named 2003 Air Force Outstanding Scientist of the Year for Mid-Career Military (6-16 years of service). He has been happily married to his wife, Kiley, since 1995.

Permanent Address: 26089 Lake Drive, Elkhart, Indiana 46514

This dissertation was typed by the author.